Politecnico di Torino

Master's degree in ENERGY AND NUCLEAR ENGINEERING
Degree Class LM-30 RENEWABLE ENERGY SYSTEMS

A.a. 2022/2023
July 2023

Numerical study of supercritical carbon dioxide accidental releases in partially confined spaces

Supervisor:
    Prof. Andrea Carpignano
Co-supervisors:
    Prof. Raffaella Gerboni
    Alberto Moscatello

Candidate:
    Giulio Fiorita   (s291306)

Abstract

The objective of this thesis is to support a preliminary project for the reconversion of decommissioned offshore platforms by conducting Computational Fluid Dynamic (CFD) simulations for risk analysis. The focus of the project is to repurpose an oil platform into a carbon dioxide injection station for storage purposes, using Carbon Capture and Storage (CCS) technologies. However, due to the changes in platform layout and the presence of another hazardous substance, the previously conducted risk analyses for hydrocarbon extraction are no longer applicable. The primary focus of this thesis is to perform numerical modeling simulations of potential incidental scenarios related to the CO_2 release that can occur on board the platform. These simulations are fundamental for risk analysis. Commercial models do not accurately reproduce these phenomena in the presence of obstacles (confined spaces), leading to inaccurate predictions of CO_2 releases that can occur in gaseous, liquid, or supercritical phases. The research object of this study has allowed on the one hand to investigate the numerical models, available in the literature, as well as the existing experiments; the scope is to implement CO_2 release simulations within confined spaces into SBAM, a Computational Fluid Dynamics (CFD) model specifically designed for analyzing incidental scenarios involving high-pressure fluid leakages in confined spaces, extending its range of applicability. This study has revealed that the application of the ideal gas equation of state (EOS) in the case of supercritical CO_2 release simulations leads to inaccurate predictions of the results. Consequently, a real gas model is required to provide a more accurate estimation of the behavior of this substance. However, the implementation of real gas models in the ANSYS Fluent software posed several challenges. Various attempts to incorporate this real gas equation of state are discussed in this thesis to highlight the encountered issues.

List of Figures

List of Tables

1.Introduction

1.1 Energy Context

In the latter half of the 20th century, the concept of sustainability began to spread. It was adopted in the Brundtland report, also known as "Our Common Future", published by (World Commission on Environment and Development, 1987), a sub-organization of the United Nations (UN). The report emphasizes the global significance of sustainable development and defines it as "*Sustainable development is the development that meets the needs of the present without compromising the ability of future generations to meet their own needs.*". Over the years, this concept has played a key role in the legislative framework, following a continuous research process for the worldwide adaptation of sustainability (Mondini G., 2019). More recently, the UN has defined 17 "Sustainable Development Goals" (SDGs) as part of the 2030 Agenda, building upon the earlier "Millennium Development Goals" (MDGs). These goals stimulate action over the next fifteen years in areas of critical importance for humanity and the planet (UN, 2015) (UNFCCC, 2019). In particular, the SDGs align with the primary goal of the Paris Agreement, which aims "*to keep the average global temperature rise well below 2 °C and as close as possible to 1.5 °C above pre-industrial levels*" (UNFCCC, 2015). These proposed actions seek to unify all nations in a shared effort to swiftly reduce greenhouse gas emissions. To understand the types and percentages of greenhouse gas emissions, Figure 1 presents the distribution of greenhouse gases emitted in the United States in 2021. Carbon dioxide is identified as one of the most significant anthropogenic greenhouse gases, contributing to approximately 80% of total emissions. The remaining 20% is attributed to other greenhouse gases. However, it is important to note that some of these gasses are even more harmful to the global climate than carbon dioxide itself. For instance, methane and nitrous oxide have much higher Global Warming Potentials (GWPs) compared to carbon dioxide. This implies that these gases have a greater ability to trap heat in the atmosphere, resulting in a stronger greenhouse effect.
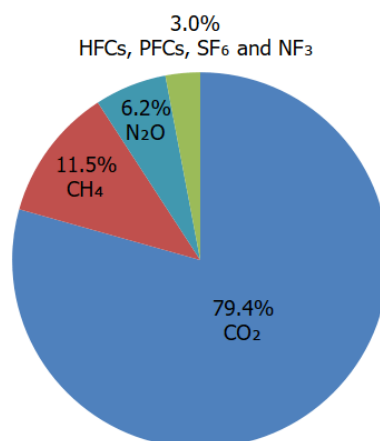
Figure 1: Overview of U.S. Greenhouse Gas Emissions in 2021. (United States Environmental Protection Agency, 2023)
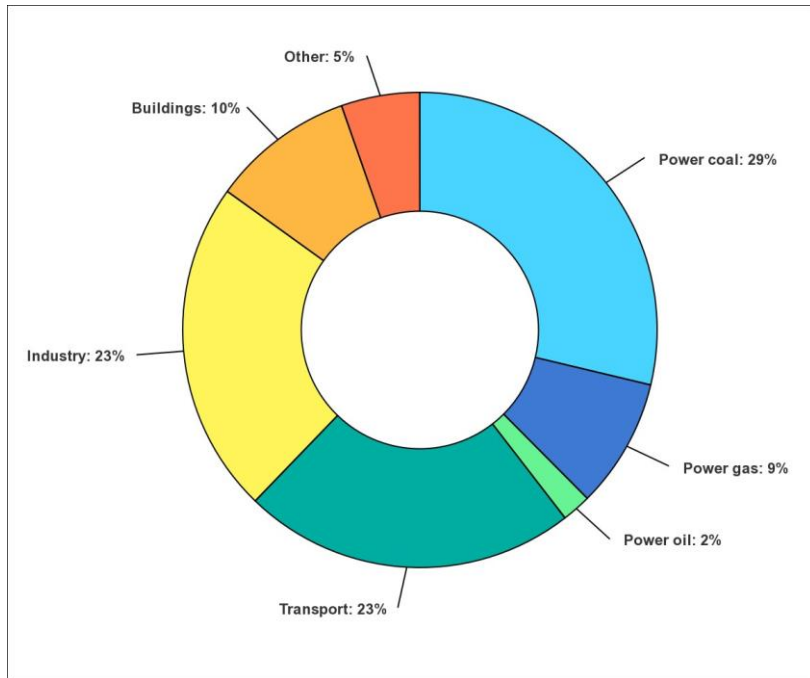
Figure 2: Sources of Global Greenhouse Gas Emissions in 2020. (IEA, 2020)

Different sectors, including electrical and thermal energy production, transportation, industries, and others, significantly contribute to these emissions. Figure 2's pie chart illustrates that the power generation sector is the most significant contributor, accounting for approximately 40% of emissions.

Figure 3: Global atmospheric CO_2 concentration. (Ritchie H. et al., 2017)

To highlight the importance of adopting strategies to mitigate greenhouse gas emissions, Figure 3 presents the evolution of global CO_2 emissions from human activities over the years. According to the IEA report "CO_2 Emissions in 2022", after two years of exceptional oscillations in energy use and emissions caused by the Covid-19 pandemic, global CO_2 emissions grew by 0.9% in 2022, reaching a new record of 36.8 Gt, which is below the global GDP growth rate of 3.2%. Emissions from energy consumption increased by 423 million tons, while emissions from industrial processes decreased by 102 million tons due to the production reduction in China and Europe. Specifically, for energy consumption emissions, natural gas emissions decreased by -1.6% due to reduced exports from Russia. However, these emissions were compensated by increased emissions from the re-ignition of coal-fired power stations, resulting in a 1.6% increase in emissions. Renewables met 90% of last year's global growth in electricity generation, specifically, solar PV and wind generation each increasing by 245 TWh, setting a new record (IEA, 2022). Given the fact that renewable sources cannot meet all the energy demand and the urgency to mitigate the effects of greenhouse gases, commonly referred to as "climate change", new opportunities have emerged. These include increasing the efficiency of fossil fuel plants, improving end-use energy efficiency, and exploring alternative methods like Carbon Capture and Storage (CCS). The International Energy Agency (IEA) has also emphasized the importance of CCUS in their special report "CCUS in Clean Energy Transitions", stating that it is the only group of technologies that can contribute to achieving the "net-zero" goals by 2050 (International Energy Agency, 2020). In this context, Chapter 2 provides a detailed description of the CCS techniques commonly employed in the industrial and energy production sectors. Numerous research programs are being conducted around the world to develop secure and economically viable CCUS projects. In this regard, Eni SpA is actively contributing to CCUS projects in Italy, specifically through the Ravenna CCS project, which aims to start its activity in 2024 with a storage capacity of 500 MT of CO_2. The research activity regarding these kinds of projects has increased over the years, driven by a growing awareness of the potential of CCUS technologies to further support emissions reduction efforts. Numerous research programs are being conducted worldwide with the aim of developing secure and economically viable CCUS projects. In this context, Eni SpA is actively contributing to CCUS projects in Italy, particularly through the Ravenna CCS project, scheduled to commence its operations in 2024 with a storage capacity of 500 MT of CO_2. The research activity surrounding these projects has increased over the years, driven by a growing awareness of the potential of CCUS technologies to further support emissions reduction efforts.

1.2 Work Objectives

Having emphasized the fact that Carbon Capture and Storage is one of the most promising technologies for the reduction of CO_2 emissions, this thesis aims to support a preliminary project that proposes a potential solution to implement CCS technology. The specific focus of the project is on utilizing a decommissioned oil platform as infrastructure for CO_2 storage in depleted hydrocarbon reservoirs. However, repurposing the platform for this new objective requires a redesign of the platform layout, including necessary modifications such as the introduction or removal of specific items. Due to the redesigned layout and the potential toxicity of high-concentration carbon dioxide, a new risk analysis

is necessary since the previously conducted risk analyses for hydrocarbon extraction are no longer applicable. The preliminary analysis of the project conducted by (F. Pertuso, 2022) has highlighted that a phase change of CO_2, from gas to supercritical phase, occurs during storage operations in the well due to the increasing pressure. However, commercially used empirical models for simulating incidental leakage scenarios tend to overestimate the risk since they do not consider various variables, such as obstacles in the proximity of the release point that can facilitate fluid dispersion.

In this context, the primary objective of this thesis is to simulate the release of supercritical CO_2 using Computational Fluid Dynamics (CFD) methods for Quantitative Risk Analysis (QRA) purposes. Several steps need to be completed before being able to simulate supercritical CO_2 releases.

Firstly, an analysis of the characteristics of under-expanded jets is necessary to understand the structure that the supercritical CO_2 jet can present during accidental leakage scenarios due to high pressure. Moreover, an analysis of the properties and equations of state (EOS) applicable to supercritical CO_2 is necessary to better simulate the release phenomenon.

Another fundamental objective of the thesis work is to determine if numerical model techniques (CFD) capable of simulating supercritical CO_2 releases are available in the literature. This research reveals that a literature gap exists, which is also in accordance with Det Norske Veritas (DNV), one of the most important institutes for risk management, and reported in their special reports on CCS.

Given the literature gap and the impossibility of using specific CFD models for the thesis objective, a parallel objective closely linked to the true scope of this thesis is proposed. Specifically, being able to simulate a CO_2 release using CFD methods, which would extend the validity range of the SBAM model. This model is developed to simulate incidental leakage scenarios in confined spaces (spaces with obstacles) using an approach based on CFD methods. This approach employs a particular strategy that aims to minimize the computational effort typically associated with classical CFD analysis while ensuring precise results as in CFD methods. Introducing supercritical CO_2 into the model's inventory would not only widen the range of validity of the model itself but also provide accurate results in the context of the risk analysis associated with the reconversion of decommissioned oil platforms for CCS purposes, which is the focus of this thesis.

For these reasons, the literature review sections also introduce experiments conducted by some authors to compare the experimental data with the results obtained from the simulations conducted in this thesis to validate the models used in the CFD analysis.

1.3 Thesis Structure

To the previously proposed objectives, this thesis is structured as follows:

Chapter 2 provides an analysis of the thesis context, including an overview of CCS technologies and their implementation in the chosen reference site for this project. Additionally, this chapter emphasizes the need for a risk analysis due to the new platform layout for carbon dioxide storage and its toxicity at high concentrations. An overview of risk analysis and the types of incidental events in the thesis context is presented.

Chapter 3 encompasses all the necessary information for developing CFD simulations. It includes an analysis of under-expanded jets, properties of CO_2, and suitable equations of state for describing CO_2 behavior. Furthermore, an essential overview of the methodology for calculating the incidental frequency of CO_2 pipelines is provided. The chapter concludes with an analysis of the SBAM model, designed to simulate high-pressure gas releases in congested environments. By simulating the release of supercritical CO_2, the applicability range of the SBAM model can be expanded to include this new substance.

Chapter 4 consists of a literature review of the numerical modeling methods for the simulation of supercritical CO_2 release. This chapter highlights the existing literature gap in this field. Additionally, it includes a review of experiments conducted by the scientific community regarding supercritical CO_2, which will be crucial for comparing the numerical simulation results with experimental data to validate the models.

Chapter 5 focuses on numerical simulations of supercritical CO_2 release using the ANSYS Fluent calculation software. Initially, a simulation using the ideal gas law as the equation of state is developed to predict CO_2 behavior. However, a comparison of the simulation results with experimental data reveals the inadequacy of the ideal gas law for supercritical CO_2, leading to the necessity to implement a real gas equation of state. Various attempts to incorporate real gas equations of state are discussed.

Chapter 6 serves as the concluding chapter, summarizing the work done and presenting potential perspectives and ideas for future development.

2. Thesis context

This thesis aims to support a specific research project financed by the Ministero dell'Ambiente e della Sicurezza Energetica (MASE) and involving the Politecnico di Torino, Environment Park, and Fondazione Istituto Italiano di Tecnologie. The project's objective is to analyze the disposal of offshore extractive platforms and propose innovative technologies for repurposing the infrastructure to minimize the environmental impact during decommissioning operations. In the master thesis by (F. Pertuso, 2022), an innovative approach was analyzed, which involves using the depleted oil deposit as a container for carbon dioxide. The following sections focus on carbon dioxide and the Carbon Capture and Storage (CCS) technologies currently available. Additionally, a summary of the work carried out by F. Pertuso in his master's thesis will be provided, specifically highlighting the implementation of CCS on a platform undergoing decommissioning. For a more detailed understanding of the system's design phase and rearrangement, it is recommended to refer to F. Pertuso's master thesis, which extensively discusses the relevant information (F. Pertuso, 2022). The information reported in this chapter aims to contextualize the project in which this thesis is developed. Moreover, understanding the redesigned layout of the platform and how the CCS technology is applicated to this case result fundamental to understanding the motivations of the work's research of this thesis.

2.1 Carbon dioxide

Carbon dioxide, also known as CO_2, is a naturally occurring molecule that has not had a good reputation in the last century due to its association with the greenhouse effect. For example, CO_2 accounts approximately for 79% of all greenhouse gas emissions from human activities in the United States in 2021 (Masson D. et al., 2021). Despite its negative connotations, carbon dioxide plays a crucial role in Earth's environment as it acts as a thermoregulator, facilitating the thermal balance between day and night and making life on Earth possible. While water vapor is the primary greenhouse gas that retains the highest amount of thermal energy from the sun, it is important to note that carbon dioxide is essential for enabling this effect. Without carbon dioxide, the average temperature on Earth would be approximately -18°C. Despite its relatively small quantity in the atmosphere (0.004%), carbon dioxide becomes part of the biogeochemical carbon cycle and fulfills important roles in the biosphere, geosphere, and hydrosphere, as shown in Figure 4. (Le Treut et al., 2007)

However, as mentioned before, human activities have significantly increased carbon dioxide emissions over the past century, intensifying the greenhouse effect and leading to a rise in Earth's temperature. The phenomenon, known as *climate change*, is causing increasingly disastrous effects on the entire planet.
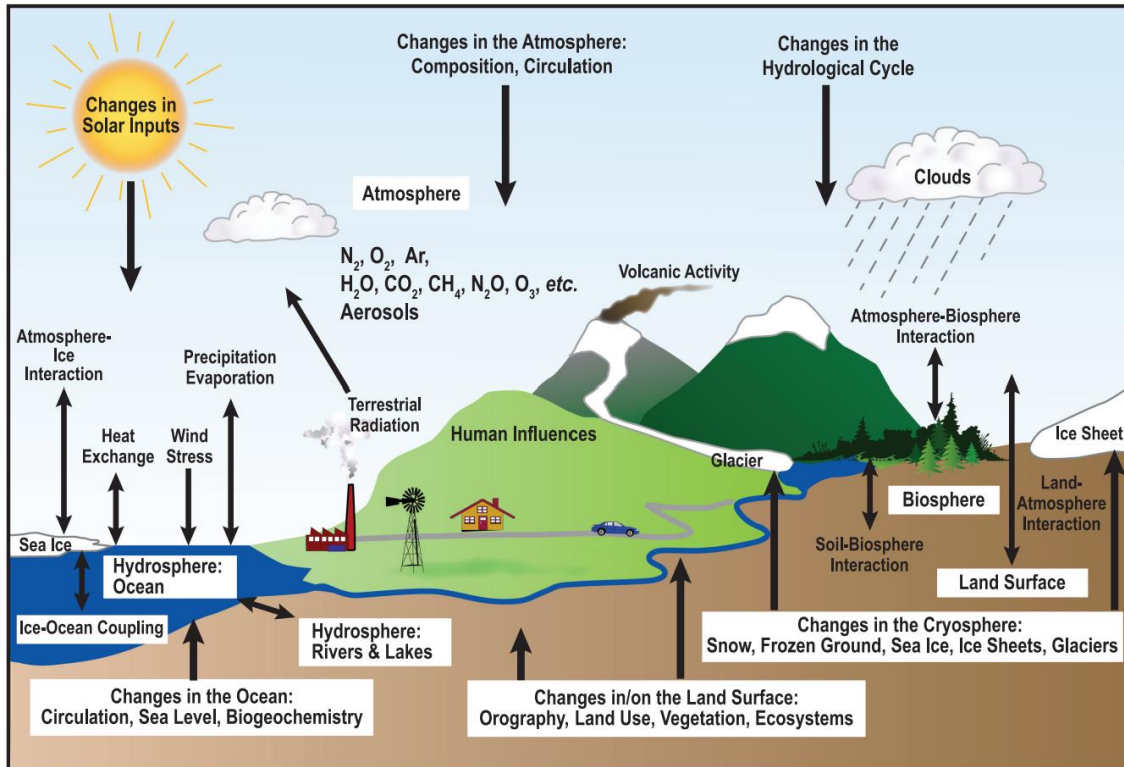
Figure 4: Processes and interactions of CO₂. (Le Treut et al., 2007)

2.2 CCUS

The need to meet the goal of the United Nations Framework Convention on Climate Change (UNFCCC) has driven the improvement and development of new technologies aimed at addressing climate change. As mentioned by the Intergovernmental Panel on Climate Change (IPCC), in its Special Report on Carbone Dioxide Capture and Storage (Metz B. et al., 2005), one of the most important technological solutions for reducing carbon dioxide emissions and mitigating the greenhouse effect is Carbon Capture and Storage (CCS). The strong need to have mitigation options and the wide range of applicability have contributed to the rapid and increasingly substantial advancement of this technology. In general, CCS technology consists of three main steps: capture, transport, and storage of CO_2.

2.2.1 Capture

The capture of CO_2 is the process of extracting carbon dioxide from various sources using different techniques. Nowadays, the extraction of CO_2 mainly takes place from large point sources such as industrial plants and fossil fuel power plants due to their economic viability. These types of plants require combustion for their operations, resulting in the emission of flue gases that contain a significant amount of carbon dioxide and other combustion by-products. Various techniques can be employed to capture and sequester the carbon dioxide. However, implementing these technologies in a plant can reduce the

18

overall efficiency of the system due to the energy required for CO_2 extraction. Nevertheless, in recent years, there have been advancements in technologies that have improved their efficiency, leading to the emergence of new methods for extracting CO_2 from small-scale sources or directly from the atmosphere. Although these methods are less efficient compared to the CO_2 capture from large-scale sources, implementing renewable sources for this purpose could become a promising resource while minimizing the impact on efficiency or energy consumption. Many types of CO2 capture technologies can be implemented in industrial plants, including sorbent or solvent-based processes, membranes, and distillation methods. In general, as shown in Figure 5, CO_2 extraction techniques can be divided into four categories: post-combustion, pre-combustion, oxyfuel, and industrial processes. The selection of a specific technique depends on the plant where it is incorporated, and each technique can influence the efficiency of the plant to varying degrees.
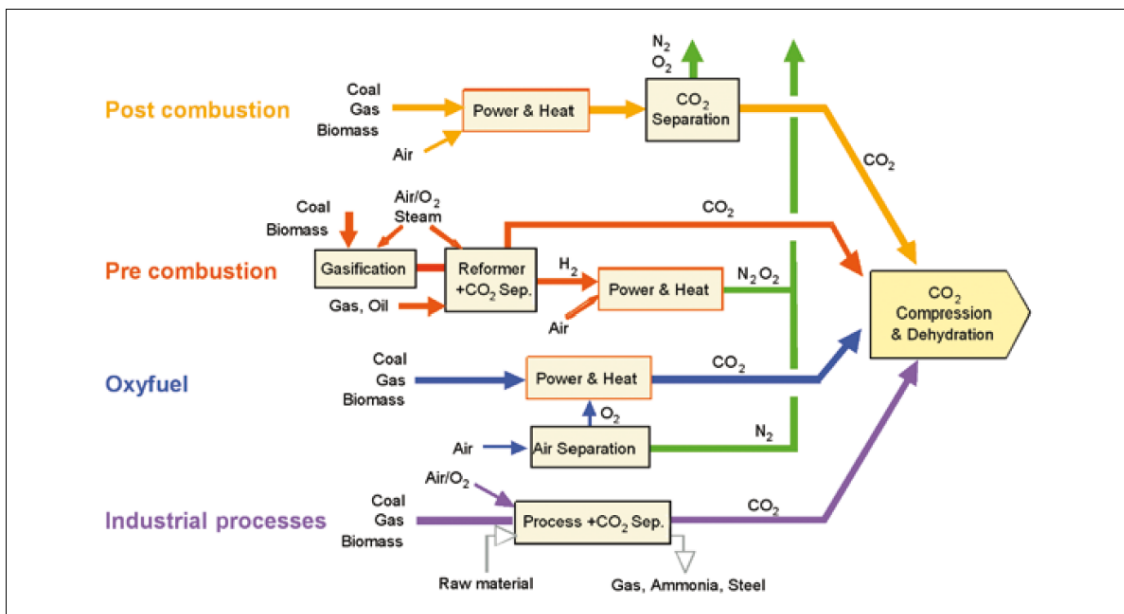
Figure 5: CO$_2$ capture systems. (Metz B. et al., 2005)

2.2.2 Transport

During the transport phase, carbon dioxide is transferred from extraction sources to the storage location. Nowadays, the most common viable options for CO_2 transport include onshore and offshore pipelines, shipping, and train transportation. Moreover, there is flexibility in determining the physical phases in which carbon dioxide is transported, whether it is as a gas, liquid, or supercritical fluid. For the latter two phases (liquid and supercritical), pressurization units are utilized to guarantee the continuous physical state of CO_2.

The selection of transportation methods depends on various variables. In general, using pipeline transportation ensures a continuous flow of CO_2 to the storage location over time, but it requires a continuous extraction from sources. On the other hand, using shipping or train transportation requires the use of storage units, which increases the installation cost

and reduces the overall system efficiency, but this method is more suitable when dealing with not-continuous sources. Nevertheless, there are numerous possibilities in transportation selection, and it often requires an analysis in terms of economics and efficiency to find the most appropriate methods that strike a good balance between costs and benefits.

2.2.3 Storage

It is necessary to find a solution for storing the extracted CO_2 in a permanent o semi-permanent way. The IPCC Special Report (Metz B. et al., 2005) explores different possibilities, including on-shore or off-shore geological storage, ocean storage, and carbonization, as shown in Figure 6. Let's examine each of these in more detail.
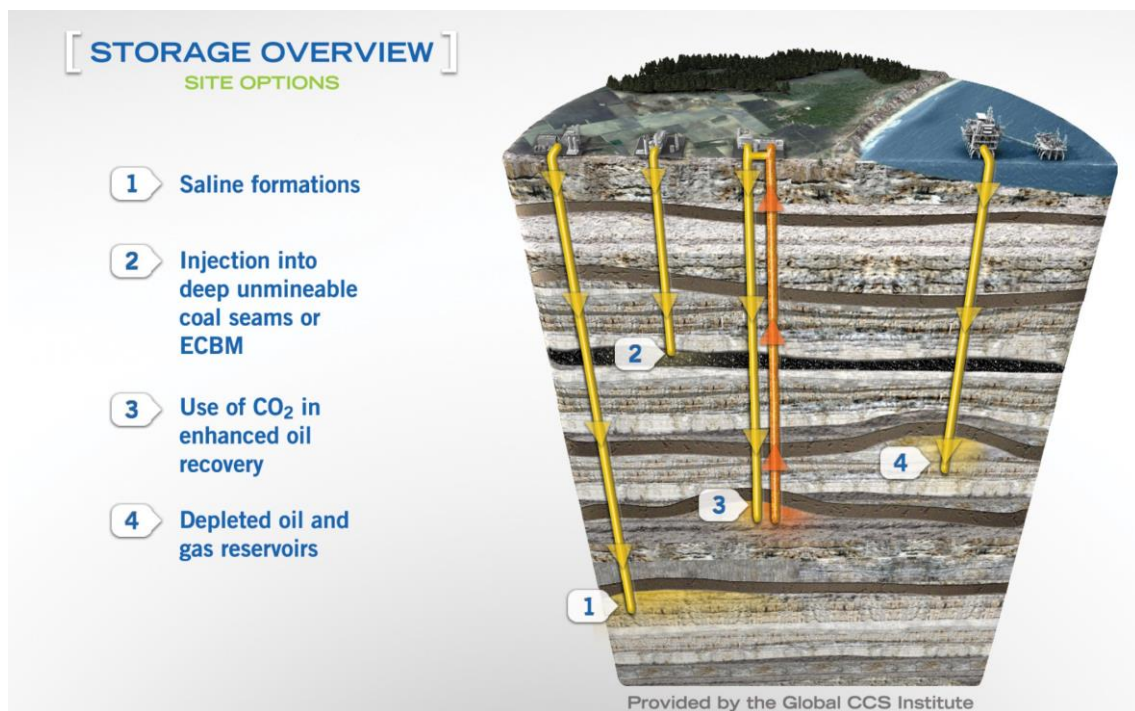
*Figure 6: Possible storage solutions. (*Global CCS Institute*, 2015)*

Underground geological storage

Naturally, carbonates have been stored in subsoil reservoirs for millions of years due to favorable concomitant conditions such as specific pressure, temperature, and the presence of reservoirs that trap hydrocarbons. Building upon this concept, the idea of injecting CO_2 into on-shore or off-shore geological structures has emerged. These structures include depleted oil fields, salt mines, and coal mines, which possess the favorable conditions mentioned earlier. Moreover, these structures are already equipped with infrastructures such as platforms, oil wells, pipelines, and other components which were necessary for extracting carbonate or salt. One of the first projects involving CO_2 injection into underground structures was developed for Enhanced Oil Recovery (EOR) in Texas. EOR is a technique developed to extract more quantities of crude oil by the injection of CO_2 into oil wells. Over the years, this technique has been adopted in other cases, leading to

technological advancements. Nowadays, given the need to reduce CO_2 emissions, similar techniques used in EOR can be applied to develop projects focused on underground CO_2 storage, as demonstrated by Sleipner Project in 1996 and other recent projects.

Ocean storage

Another storage solution involves trapping CO_2 under the ocean, where it can remain confined for centuries. The role of oceans in the capture of CO2 is truly important, as they are estimated to absorb around 25% of anthropogenic CO2 emissions yearly. It is important to note that this process involves both the ocean surface and the seabed, which make significant contributions (Sallée et al., 2012). However, injecting a large amount of CO_2 into the seabed could lead to modifications in seawater acidification, causing a decrease in pH and potentially affecting the organisms in the surrounding area of injection.

Mineral carbonation

Mineral carbonation is a technique that involves using metal oxides to fix the CO_2 as carbonates with other by-products. However, natural carbonation is a slow process and releases a small quantity of energy because it is an exothermic reaction. To increase the reaction rate, intensive energy preparation of the solid reactants is necessary. Carbonation is already used in various industrial processes to produce urea, methanol, inorganic and organic carbonates, polyurethanes, or other niche products. However, implementing carbonation in power plants results in a significant increase in energy consumption, ranging from 60 to 180%, which consequently reduces the overall efficiency of the plant.
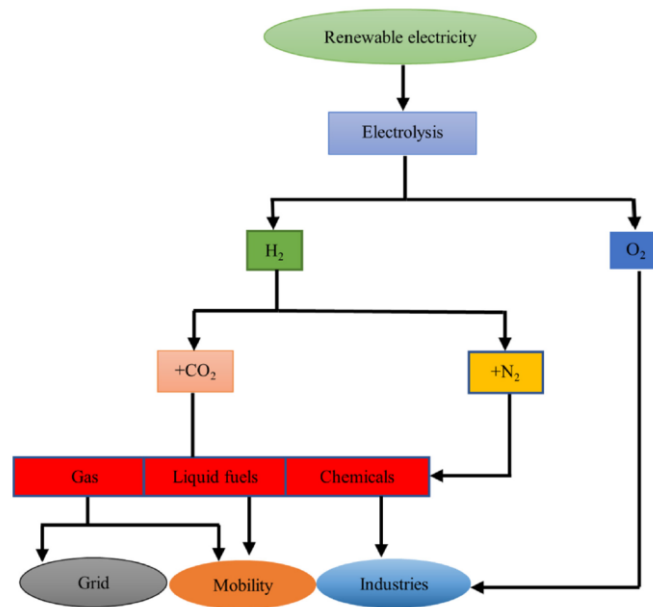
Figure 7: P2X's schematic representation. (Dahiru et al., 2022)

Utilization

In addition to carbonation, other processes can fix carbon dioxide for an extended period, and some applications can produce valuable carbon-containing products. This concept is

known as Carbon Capture Utilization and Storage (CCUS). Power-to-X (P2X) technologies, for example, use renewable energy to transform CO_2 into various products. While the primary objective of P2X is the production of hydrogen (H_2), it can also be combined with CO_2 to produce both gaseous and liquid fuels. This process is known as Power-to-Gas (P2G) and Power-to-Liquid (P2L). Additionally, as shown in Figure 7, it is possible to generate other industrial products, making this application flexible and adaptable for multiple purposes. (Dahiru et al., 2022)

2.3 Site and Infrastructure Selected

The selected offshore platform for the project is known as GREEN1 located 18 kilometers far away from the Adriatic Sea Coast near Ancona and Rimini. This region has the highest concentration of oil platforms in Italy, accounting for approximately 90% of them (A.C. Uggenti et al., 2022). GREEN1 was chosen primarily for its similarities with other oil platforms in the country, enabling the possibility of extending the project to other similar cases. The availability of documentation and data regarding the platform and reservoir played a crucial role in selecting the site, as it ensures realistic results by the end of the project.

In the area of interest, the mean wind speed is almost uniform during the year, ranging between 4 and 5 m/s. The study of the seismicity in the region has been previously evaluated due to the platform's operating activities, and it does not affect the conversion operations of the platform.
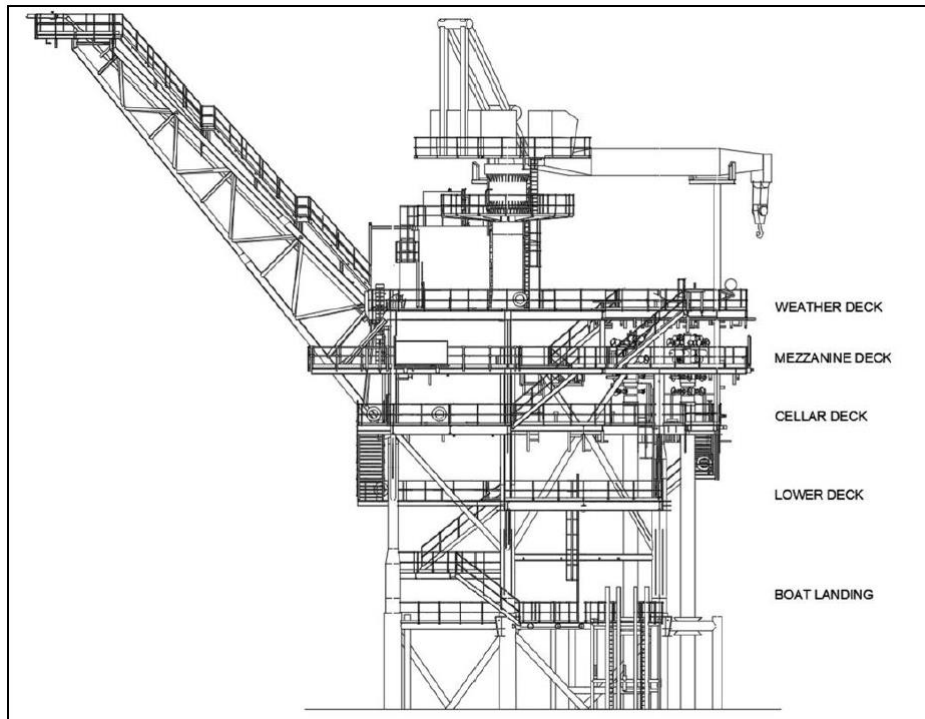
Figure 8: Lateral view GREEN1. (A. Aliberti, 2021)

GREEN1 is an offshore fixed oil platform designed for natural gas extraction, distinguishing it from the perforation platforms due to the different items with which it is

equipped. Given its components, GREEN1 is considered representative of other oil platforms located in Italy. The platform consists of a fixed jacket with six legs directly anchored to the seabed, approximately 25 meters below the sea surface. As shown in Figure 8, the platform comprises four decks: the Lower deck, Cellar deck, Mezzanine deck, and Weather deck located respectively at 11, 15, 18, and 21 meters from the water surface. (A. Aliberti, 2021) The following paragraphs will discuss how the design and the rearrangement of the entire structure of the platform have changed and how this can impact risk analysis, highlighting the need to simulate supercritical CO_2 releases, the main objective of this thesis.

In addition, the platform is connected to a subsea power line that supplies the necessary electricity for unattended operations. Furthermore, it is connected to a pipeline that, in its pre-conversion state, transported natural gas from the platform to the coast. In the current project, the pipeline is repurposed to transport CO_2 for storage purposes from the sources to the platform.

The oil platform is connected to four oil wells, which are in line with the average number of oil wells typically associated with similar infrastructures in Italy. The CO_2 phase change from gas to the supercritical state will occur in the subsea region of the well due to the high pressure that incomes in the low level of the well. Each well is supported by a casing made of concrete and steel to ensure long-term durability. A Christmas Tree is connected to the wellhead (the lowest part of the well) to prevent the release of crude oil or hydrocarbons into the atmosphere.

Another crucial element to analyze is the reservoir, as it significantly influences the rearrangement design of the system. Factors such as reservoir depth, fracture pressure, starting pressure of storage activity, volume, and temperature gradient need to be taken into account. Pertuso F.'s master thesis highlights that the reservoir characteristics used in this project are based on average values derived from data collected from various reservoirs in the country. However, conducting an accurate analysis of the reservoir is essential to ensure the safety of the reservoir structure itself. Table 1 presents the data used for the design, providing an initial understanding of the pressure and temperature magnitudes involved during the simulation of the supercritical CO_2 releases, which constitutes the core focus of this thesis.

Table 1: Characteristics of the reservoir. (F. Pertuso, 2022)

characteristic	values
depth	*2000 m*
max. fracture pressure	*145 bar*
min. operating pressure	*79 bar*
volume	*485 MSm^3*
temperature gradient	*15 °C/Km (for the first 3Km)*

2.3.1 New platform configuration

Having thoroughly studied the layout of a typical offshore platform and considering the fundamental parameters of the reservoir, Pertuso F.'s master thesis focused on the rearrangement of the platform layout. This process began with the analysis of CO_2 capture

and transport, exploring the possible sources and transportation options available in the area near the platform. Subsequently, using a MATLAB code, the focus of the analyses shifted to calculating the properties of CO_2 that would change during its injection into the reservoir. The examination of carbon dioxide's physical properties will be covered in the next chapter, as they play a crucial role in CFD analysis. Furthermore, a rearrangement of the platform was presented to assess which existing components can be utilized and how the introduction of new components impacts the available space on the platform. This point holds significant relevance for the arguments that will be extensively discussed in the upcoming chapters due to its relevance to risk analysis.

At the end of the analysis, the deck items that were identified for decommissioning are highlighted with an "*X*" in Table 2. These components are unnecessary for the new purpose of the plant, and therefore, the components that influence the installation area of the new components must be removed. Alternatively, another possible solution is to ensure the safety of these components by leaving them on the platform, minimizing the decommissioning procedure, as long as they do not conflict with the new purpose. The essential items required for the platform to operate as a CO_2 storage facility include the Compression Package, the Stock Buffer, the Uninterruptible Power Supply, and plant safety systems. When comparing the old design of the platform with the new one, the latter appears to be generally less bulky with lower footprint indexes, as shown in Table 3.

Table 2: Deck's items subject to decommissioning. (F. Pertuso, 2022)

Descrizione	*Smantellamento*	*Descrizione*	*Smantellamento*
WEATHER DECK		*LOWER DECK*	
Technical room		Nitrogen bottle rack	X
Main diesel generator package	X	Safety shower and eye wash station	
PA/GA system		Diesel fuel skid	X
Antenne/VHF Marine/GPS		Chemical & corrosion injection skid	X
Fireman equipment container		Water foam FF skid	X
Safety shower and eye wash station		Hydrate inhibitor skid	X
Water tank	X	*BOAT LANDING*	
Water pump	X	Vent KO drum booster pump	X
CELLAR DECK		KO Drum	
Drain manifold area	X	Sump Caisson	
Production manifold area	X	Sump Caisson Pump	
Test manifold	X	Life jacket storage box	
Test separator		*MEZZANINE DECK*	
Chemicals storage tanks	X	Piping separator	X
Hydrate inhibitor storage tank	X	Accumulator group	
Safety shower and eye wash station		Wellhead control pannel	
Launching trap		Diesel fuel storage tank	X

One of the key advantages of this project is not only studying the feasibility of CO_2 storage within former reservoirs but also the opportunity to utilize existing platform structures and components. This approach significantly reduces the costs associated with decommissioning, making it a cost-effective solution.

Table 3: Bulk index. (F. Pertuso, 2022)

	Indice di ingombro pre-riconversione	*Indice di ingombro post riconversione*
Weather Deck	47%	43%
Mezzanine Deck	30%	15%
Cellar Deck	44%	26%
Lower Deck	35%	25%
Boat Landing	27%	27%

2.4 Toxicity

As mentioned in Chapter 1, conducting simulations for incidental scenarios of supercritical CO_2 releases is crucial for QRA purposes for two main reasons including the new layout of the platform due to the introduction of new items for the new purposes of the infrastructure, and the toxicity of the CO_2 in high concentrations.

Before the advent of CCS systems, concentrated CO_2 inventories were limited, for example, in fire suppression systems or other limited technologies. The exposure to CO_2 from humans was controlled through localized hazard management measures. Nowadays, with the advancement of CCS technologies, the potential exposure to hazardous concentrations of CO_2 has become more realistic, resulting in an extensive analysis of the effects of CO_2 on human health.

Carbon dioxide is a component that humans come into contact with daily through inhaled air. The composition of air in the lungs contains approximately 75% nitrogen, 14% oxygen, 5% CO_2, and 6% water vapor, while the composition of air in the atmosphere contains only approximately 0.04% of CO_2. Epidemiological, toxicological, and health surveillance studies have demonstrated that inhaling a significant amount of CO_2 can lead to various effects, including headaches, increased respiratory and heart rate, dizziness, muscle twitching, confusion, unconsciousness, coma, and even death. These effects are not limited to the respiratory system but can also involve the cardiovascular system and the central nervous system. Table 4 provides an overview of the different effects that CO_2 can have on human health depending on the concentration of CO_2 in the air and the duration of exposure. (Holt H. et al., 2021)

Table 4: Effects on human health due to CO_2 concentrations in air and exposure time. (Holt H. et al., 2021)

CO₂ concentration in air (% v/v)	Exposure	Effects on Humans
17-30	Within 1 minute	Loss of controlled and purposeful activity, unconsciousness, convulsions, coma, death
>10 – 15	1 minute to several minutes	Dizziness, drowsiness, severe muscle twitching, unconsciousness
7 – 10	Few minutes	Unconsciousness, near consciousness
	1.5 minutes to 1 hour	Headache, increased heart rate, shortness of breath, dizziness, sweating, rapid breathing
6	1 – 2 minutes	Hearing and visual disturbances
	≤ 16 minutes	Headache, difficulty breathing (dyspnea)
	Several hours	Tremors
4-5	Within a few minutes	Headache, dizziness, increased blood pressure, uncomfortable breathing
3	1 hour	Mild headache, sweating, and difficulty breathing at rest
2	Several hours	Headache, difficult breathing upon mild exertion

Another important impact caused by the high CO_2 concentration that needs to be considered is the decrease in the concentration of other air components as they are replaced by CO_2. Specifically, Figure 9 represents how the oxygen concentration in the air decreases as carbon dioxide replaces it. Specifically, when the concentration of oxygen decreases, it can lead to asphyxiation in different stages depending on the level of oxygen reduction, causing varying degrees of harm to humans, as shown in Table 5.
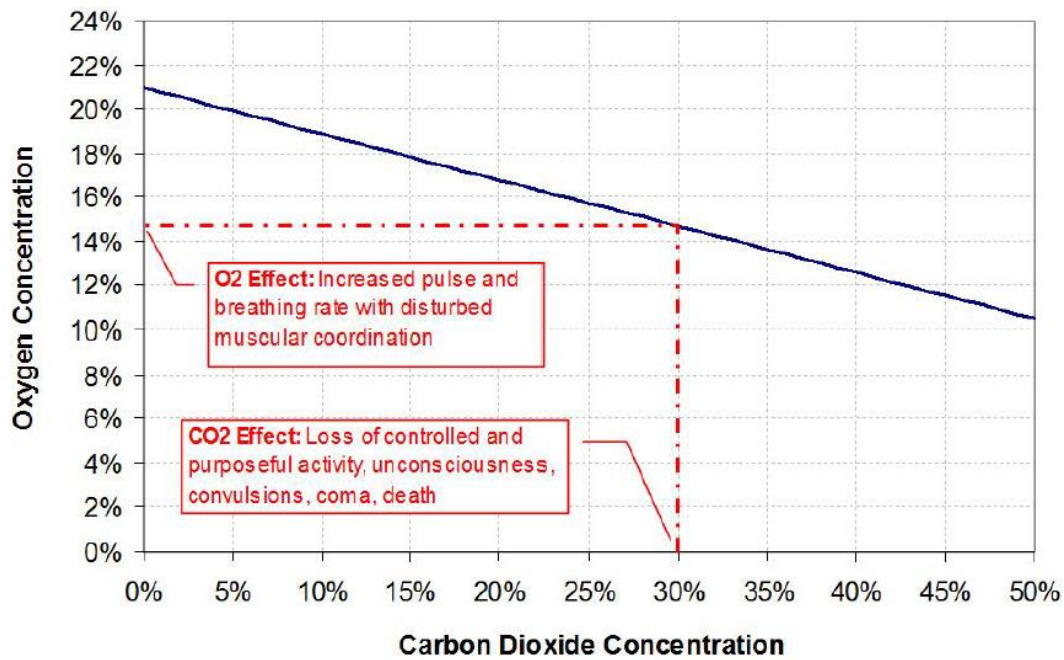
Figure 9: Oxygen concentration in the function of the carbon dioxide concentration. (Holt H. et al., 2021)

Table 5: Different asphyxiation levels due to the oxygen reduction in the air. (Holt H. et al., 2021)

Asphyxiation Stage	Oxygen Concentration (%v/v) Effects
1st	21 to 14% : Increased pulse and breathing rate with disturbed muscular coordination
2nd	14 to 10%: Faulty judgement, rapid fatigue and insensitivity to pain
3rd	10 to 6% : Nausea and vomiting, collapse and permanent brain damage
4th	Less than 6% : Convulsions, breathing stopped and death

Nowadays, there is limited information available regarding the evaluation of consequences related to CO_2 releases in CCS projects, with one of the most significant sources being a publication by the UK's Health and Safety Executive (HSE). The HSE has developed indexes, known as Dangerous Toxic Loads (DTL), which assess harmfulness on humans considering the concentration levels and the duration of the exposure to hazardous substances. Specifically, in this context, the Specified Level Of Toxicity (SLOT) and the Significant Likelihood Of Death (SLOD) are the most important because represent relatively the dose that can cause fatality in susceptible individuals and the dose that results in a 50% fatality rate (commonly referred to LD50) in the exposed population. For CO_2, the following expressions are used to calculate the SLOT DTL and SLOD DTL, where c represents the concentration of CO_2 in the air, and t represents the duration of exposure:

SLOT DTL: $$1.5 * 10^{40} = c^8 * t \qquad (1)$$

SLOD DTL: $$1.5 * 10^{41} = c^8 * t \qquad (2)$$

Figure 10 illustrates both the SLOT and SLOD DTL, demonstrating the small difference between the two curves, representing the sensitivity of the human body to even slight variations in CO_2 inhalation.
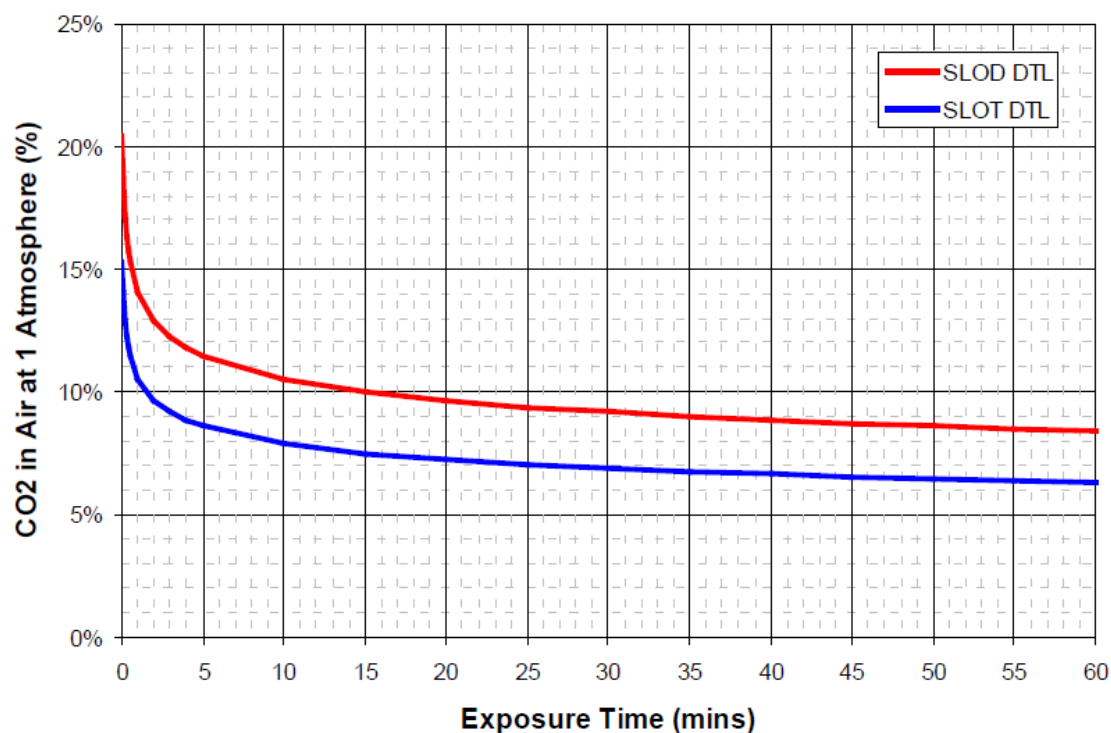
Figure 10: SLOD and SLOT DTL representation. (Holt H. et al., 2021)

Table 6: Example of exposure limits for OELs purposes. (Holt H. et al., 2021)

Exposure Time	% CO$_2$	Comment	Reference
10 hours	0.50%	Time weighted average	NIOSH (US)
8 hours	0.50%	Time weighted average Occupational Long Term Exposure Limit (LTEL)	OSHA (US) COSHH HSE (UK)
60 mins	4%	Emergency Exposure Level for submarine operations	USA Navy
	2.5%	Emergency Exposure Level for submarine operations	National (US) Research Council
	5%	Suggested Long Term Survivability Exposure Limit	HSE (UK)
	2%	Maximum exposure limit	Compressed Gas Association 1990
20 mins	3%	Maximum exposure limit	Compressed Gas Association 1990
15 mins	1.5%	Occupational Short Term Exposure Limit (STEL)	COSHH HSE (UK)
	3%	Short Term Exposure Limit (STEL)	Federal occupational safety and health regulations (US)
10 mins	3%	Recommended Short Term Exposure Limit (STEL)	NIOSH (US)
	4%	Maximum exposure limit	Compressed Gas Association 1990
7 mins	5%	Maximum exposure limit	Compressed Gas Association 1990
5 mins	5%	Suggested Short Term Exposure Limit (STEL)	HSE (UK)
	6%	Maximum exposure limit	Compressed Gas Association 1990
3 mins	7%	Maximum exposure limit	Compressed Gas Association 1990
1 min	15%	Exposure limit	NORSOK (Norway)
<1 min	4%	Maximum Occupational Exposure Limit	Federal occupational safety and health regulations (US)

Occupational Exposure Limits (OELs) are indexes that represent the maximum acceptable concentration of hazardous substances in the workplace. These limits are set by national authorities and therefore vary around the world. Table 6 reports some of the published CO_2 exposure limits for humans found in the literature. It is important to note that further analysis on CO_2 exposure limits needs to be conducted due to the increasing adoption of CCS technologies in energy scenarios, as these technologies may introduce new considerations and potential exposure situations.

The effect of CO_2 toxicity in CCS technologies on human health was extensively discussed in Gallo A.'s master thesis (Gallo A., 2021). Moreover, other critical aspects emerged from this research work, such as the effects of blast and cryogenic on human health. These three critical effects were compared together, revealing the SLOD areas defined by the heat radiation is larger than those defined for toxicity. However, in this thesis, the focus is primarily on the use of Computational Fluid Dynamics (CFD) simulations to estimate CO2 concentration in the case of incidental leakages scenarios due to the not accurate results provided by the semi-empirical methods (Phast) used also in (Gallo A., 2021). As a result, the topics related to blast and cryogenic effects were not extensively addressed in this thesis.

2.5 Risk Assessment

The information provided below is given from educational documents written by Prof. Carpignano (Carpignano A., 2009), Moscatello A.'s Doctoral of Philosophy thesis (Moscatello A., 2023), and scientific papers from Det Norske Veritas (DNV) (Hamish H. et al., 2021c).

The previous paragraphs have emphasized that CO_2 is a toxic substance, highlighting the need to focus on risk analysis in the context of CCS application. Moreover, it has been noted that the layout of the platform has changed, and as a result, the risk analysis conducted previously for the hydrocarbon extraction processes cannot be used for this new purpose. It was concluded that a risk analysis is required primarily due to two reasons: the new platform layout and the change in substance hazard from hydrocarbons to carbon dioxide. Let's delve into the details of what it means for risk analysis.

Risk analysis is a tool applicable to several disciplines and aims to estimate the damages resulting from accident scenarios that can occur during normal operations by quantifying the risk. The objective of this methodology is to suggest preventive and mitigation actions that can render the risk acceptable. Two main approaches, qualitative and quantitative, can be used to evaluate risk concerning people, the environment, assets (of any kind), and reputation (related damage in the loss of Company reputation).

Qualitative approach

This analysis uses qualitative criteria to assess the impact of accidents or failures in terms of damage to individuals and financial losses, including repair costs and production losses. However, numerical data are not involved in this approach, resulting in a less precise model. Instead, tables are used with various indices for different aspects such as safety, health, environment, production, maintenance, and reputation. Once these indices are identified, a risk matrix is developed, highlighting three regions: Unacceptable,

ALARP (As Low As Reasonably Practicable), and Acceptable. This approach is typically used in the preliminary stages due to its ease of application and speed.

Quantitative approach

In contrast to the qualitative approach, Quantitative Risk Assessment (QRA) utilizes numerical data to estimate the risk for a specific scenario. This approach is considered the most appropriate method, as defined by the European Union (EU) Offshore Safety Directive 2013/30/EU (Moscatello A., 2023). The general formulation of the risk, denoted as "R", is presented in the equation below. The variable "L" represents the likelihood, typically estimated through a Probabilistic Risk Assessment (PRA) and expressed as an event per year. The variable "D" represents the damage caused by the same event and it is expressed as damage per event.

$$R = f(scenario, L, D) \qquad (3)$$

At the end, "R" is expressed in damage per year, and the total risk of an activity is calculated as follows:

$$R_{tot} = \Sigma_{scenarios} R \qquad (4)$$

It is important to note that "R_{tot}" represents the total risk, and the summation is performed over all the considered scenarios.

The procedure for Risk Analysis is outlined in the flow chart presented in Figure 11, which includes several steps leading to a Risk Assessment and the quantification of the risk. The hazard identification phase aims to identify all the events that could potentially cause an incident. This is typically achieved using tables or databases that systematically examine the components and possible failure modes. For example, the Hazard and Operability Study (HAZOP) procedure is often employed for this purpose.
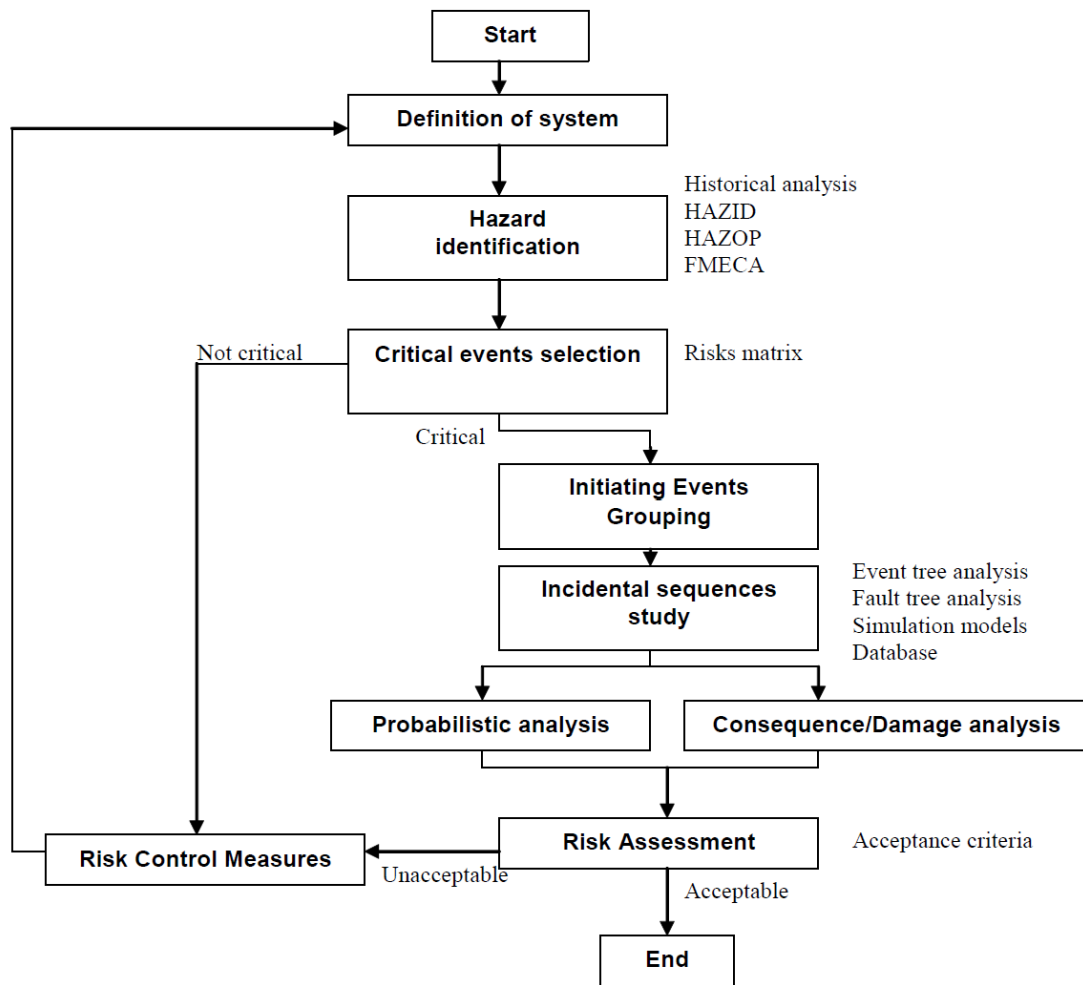
Figure 11: Risk Analysis flowchart. (Carpignano A., 2009)

After identifying the hazards, it is necessary to associate a certain frequency with which these accidental events can occur. Methods such as Event Tree or Fault Tree Analysis are employed for this purpose. These techniques consider not only the probability that an event can occur but also include all the incidental sequences that link multiple events together. The risk is determined by combining the frequency and consequence of these events.

In the end, the total risk is plotted in a diagram, as shown in Figure 12, and can fall into three possible areas: unacceptable, ALARP, or acceptable. By implementing preventive or mitigation measures, it may be possible to shift the risk to a safer area.

Practically, there is a wide range of accidents that can occur during normal operations. In a risk analysis, various scenarios are considered, including pool fires, jet fires, flash fires, explosions, vapor clouds explosions, BLEVE (Boiling Liquid Expanding Vapor Explosion), dust explosions, and the release of toxic and flammable materials. In this thesis, the focus is specifically on the release of carbon dioxide, which is known to be toxic at high concentrations, as mentioned in the toxicity section of this thesis.
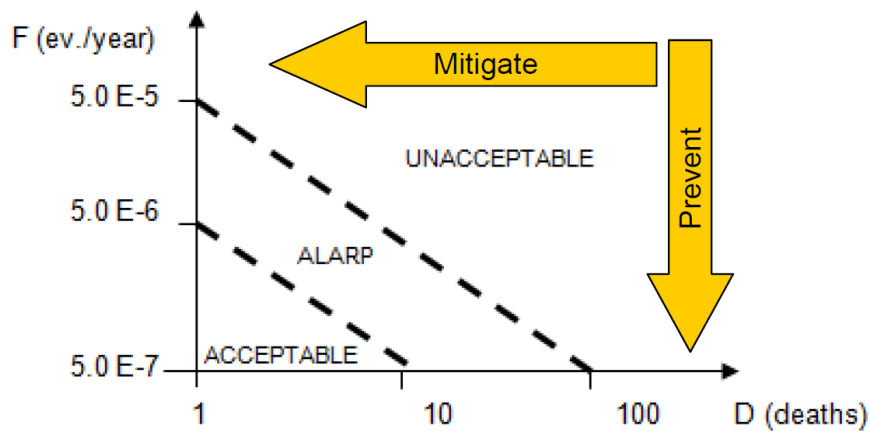
Figure 12: Diagram for the estimation of Tolerability. (Carpignano A., 2009)

The industrial sectors that involve numerous hazard components result in complex cases that require the analysis of a significant number of accidental scenarios. Nowadays, simple and fast methods are employed to estimate the risk due to the high number of scenarios and the time required for estimation. This time must be comparable to the time required for the design phase for practical reasons. However, as discussed in detail in Moscatello A.'s Doctoral of Philosophy thesis (Moscatello A., 2023), conventional techniques usually employed by companies, such as PHAST and AHOLA software, tend to overestimate the risk values because they do not consider factors such as layout complexity, physical phenomena like turbulent free-jects, and gas dispersion to provide quick results.

In the context of converting a decommissioned oil platform for CCS installation, supercritical CO_2 is utilized. Therefore, a risk analysis must be conducted due to the toxicity of the employed substance and the redesign of the platform layout. For this reason, the main objective of this thesis is to focus on simulations of supercritical CO_2 releases.

3 Methodology and Analysis Framework

This chapter provides an overview of the methodologies utilized in this thesis work. In the previous chapter, a discussion was presented regarding the selected platform and the applicable CCS technologies. It was concluded that a risk analysis is required primarily due to two reasons: the new platform layout and the change in substance hazard from hydrocarbons to carbon dioxide.

To analyze the incidental scenarios of supercritical CO_2 releases, which is the main objective of this thesis, a general overview of the theory related to under-expanded jet releases is presented in this chapter. Understanding the characteristics of the jet from supercritical CO_2 releases is crucial for the subsequent CFD analysis.

Furthermore, a study on the properties of CO_2, with a specific focus on supercritical CO_2, is necessary to simulate its behavior during high-pressure releases. The choice of an appropriate equation of state (EOS) for the substance is particularly important in this regard.

Additionally, for risk analysis purposes, it is essential to understand the potential types of pipeline failures that could occur. Therefore, a statistical analysis is proposed to evaluate pipeline failure probabilities and the dimensions of the holes.

However, as will be discussed in the next chapter, it will be highlighted that there is a literature gap concerning the numerical modeling of supercritical CO_2 releases, and there is no established methodology for simulating the releases of supercritical CO_2 using classical CFD software. In this regard, finding a method to develop CFD simulations for the release of supercritical CO_2 would support the SBAM model, becoming a new important objective for this thesis. The SBAM model is designed for the analysis of accidental gas leakages from high-pressure (HP) components in the industrial field. By finding a way to simulate these types of releases, it would be possible to expand the range of applicability of the SBAM model to include supercritical CO_2. An overview of the SBAM model will be provided in this chapter to demonstrate its potential in analyzing such scenarios.

At the end of this chapter, a recap is provided regarding certain characteristics of the phenomenon analyzed and the context in which the study is situated. This recap will help in designing a specific approach to the problem and defining a suitable methodology for conducting CFD simulations of supercritical CO_2 releases for QRA purposes.

3.1 Under-expanded jets release

This paragraph was designed to provide clarity on the characteristics of an under-expanded jet release from a high-pressure pipeline or tank. Understanding this concept is essential before analyzing numerical models and experiments found in literature, and the SBAM model used for the incidental scenarios in QRA (Quantitative Risk Assessment).

An under-expanded jet occurs when a fluid is released from a component at a higher pressure than the ambient pressure while adhering to certain criteria. To better understand when this phenomenon occurs, the introduction of the pressure ratio η_0 is necessary. The pressure ratio can be defined as:

$$\eta_0 = \frac{P_0}{P_a} \tag{5}$$

Where, P_0 represents the pressure inside the component, while P_a represents the external ambient pressure that is assumed to be 1 bar. The condition for a fluid to exhibit the structure of an under-expanded jet is to be choked, which means the fluid exceeds its critical pressure R_{cr}. The calculation of this gas property is based on the following formula, which γ represents the adiabatic expansion coefficient:

$$R_{cr} = \left(\frac{2}{\gamma+1}\right)^{\frac{\gamma}{\gamma-1}} \tag{6}$$

At the end, a flow is considered critical when the following condition is met:

$$\frac{1}{\eta_0} = \frac{P_a}{P_0} < R_{cr} \tag{7}$$

In this type of flow, it is possible to divide the flow into three zones: the nearfield, the transition, and the far-field zones, extending from the release nozzle to the distant ambient region.

The nearfield zone

The nearfield zone exhibits various flow structures depending on the pressure ratio η_0. For moderately under-expanded jets, the structures can be like a "diamond" or an "X". In the case of highly under-expanded jets, the structures can appear as a "barrel" or a "bottle" with a Mach disk formation in the middle. Figure 13 illustrates a typical structure of a highly under-expanded jet, where a discontinuity region known as the "Mach disk" is visible in the middle. Practically, in the initial part of the release, the flow velocity is higher than the speed of sound, after a certain distance the flow velocity reduces under the value of the speed of sound. When this transition occurs the Mach disk become visible. In other words, the Mach disc is the visible transition from supersonic to subsonic flow. It is worth noting that in the region before the Mach disk, the Mach number (Ma) is greater than 1, indicating supersonic flow, while after the Mach disk, the Mach number is less than 1, indicating subsonic flow. Additionally, it is common to observe a high Reynolds number (Re) in this region, indicating turbulent flow. (Munson B.R. et al., n.d.)

The far-field zone

In the far-field region, compressible effects are also present due to the Mach number that is higher than 0.3, but qualitatively, the flow behaves similarly to a classical jet. This region is commonly referred to as the subsonic flow region since the Mach number after the Mach disc remains below 1. After a certain distance (Ma < 0.3), the flow is assumed to be incompressible.

Concerning the Mach number, it is a dimensionless number that represents the relationship between the velocity (v) of the fluid flow and the speed of sound (c) in the fluid. It can be calculated using the equation:

$$Ma = \frac{v}{c} \tag{8}$$
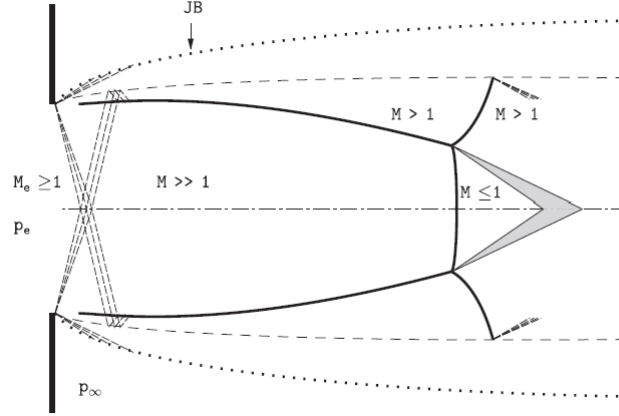
Figure 13: Typically structure of an under-expanded jet in the nearfield region. (Franquet et al., 2015)

The analytic estimation of the Mach disk distances "x" is provided in the literature by (Crist et al., 1966), where D_e represents the diameter of the release nozzle:

$$x = D_e \sqrt{\frac{\eta_0}{2.4}} \tag{9}$$

3.2 Carbon Dioxide Properties and Behavior

As previously announced, during the storage operations, CO_2 undergoes a phase change from the gas phase to the supercritical phase during the descent along the well due to the increasing pressure. It is crucial to understand the physical and chemical properties of CO_2 before proceeding with the discussion of the following argument presented in this thesis. Given the limited knowledge regarding numerical modeling of high-pressure supercritical CO_2 releases into the environment, this thesis aims to propose numerical models to simulate and estimate the behavior of CO_2 in case of accidental releases as its primary objective. In this regard, the information regarding carbon dioxide's properties is primarily sourced from Det Norske Veritas (DNV), the leading company in the world in assurance services and risk management. (Hamish H. et al., 2021)

3.2.1 Properties

Carbon dioxide (CO_2) is a stable, non-flammable molecule that has two oxygen atoms covalently bonded with a carbon atom.

The supercritical phase appears after the critical point highlighted in the phase change diagram in Figure 14. In this state, CO_2 presents high density like in a liquid state while maintaining the viscosity of a gas.

Table 7 shows the most important properties of CO_2, highlighting the critical pressure, critical temperature, and density at the critical point, which are crucial for the scope of this thesis.

The supercritical phase appears after the critical point highlighted in the phase change diagram in Figure 14. In this state, CO_2 presents high density like in a liquid state while maintaining the viscosity of a gas.

Table 7: CO₂ properties. (Holt H. et al., 2021)

Property	Unit	Value	Property	Unit	Value
Molecular Weight	g/mol	44.01	Standard (gas) density	kg/m³	1.98
Critical Pressure	bara	73.8	Density at critical point	kg/m³	467
Critical Temperature	°C	31.1	Liquid density at 0°C, 70bars	kg/m³	995
Triple point pressure	bara	5.18	Sublimation temp, 1bar	°C	-79
Triple point temperature	°C	-56.6	Solid density at freezing point	kg/m³	1562
Aqueous solubility at 25°C, 1 bar	g/L	1.45	Colour	-	None
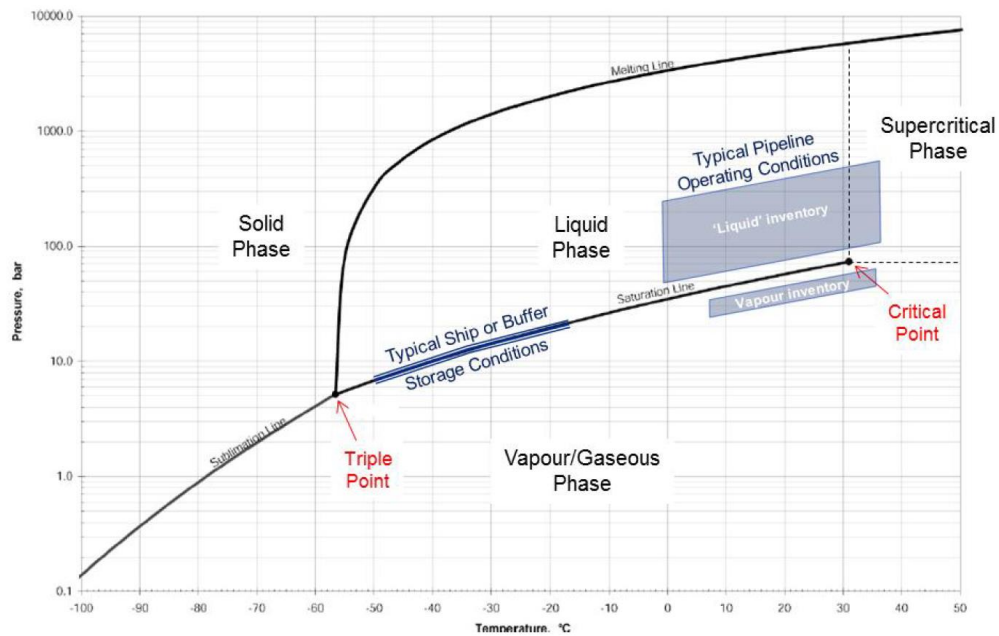
Figure 14: phase change diagram. (Hamish H. et al., 2021b)

It is important to note that below the triple point, CO_2 exists in the solid state (T=-56.6 °C). This point is relevant when considering a conventional under-expanded jet of

supercritical CO_2, as it can lead to the formation of an ice cloud. This aspect will be extensively discussed in the chapter dedicated to the experimental literature review.
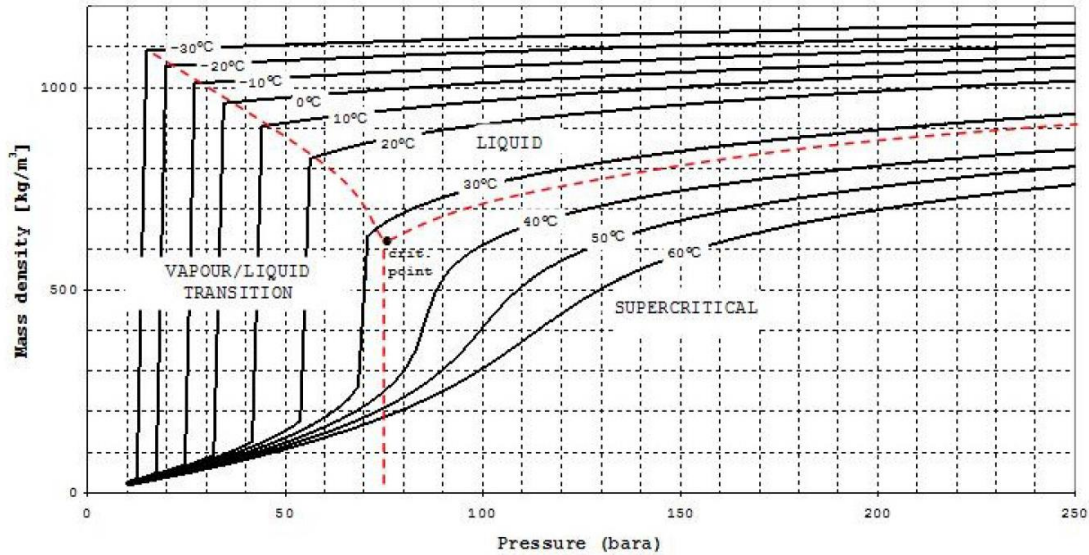
Figure 15: Density as a function of pressure at different isothermal using P-R equations of state. (Holt H. et al., 2021)

The behavior of density is best described by the chart in Figure 15, which clearly illustrates the significant differences in density values between the supercritical, liquid, and gaseous states of CO_2. For this reason, it is important to consider the variation of the density in any application that involves the liquid and supercritical state. The implementation of a real gas equation of state (EOS) that accurately describes the behavior of the density is recommended. Figure 15 and Figure 16 differ in the EOS employed for density estimation, with the Peng-Robinson EOS used in one case and the Span Wagner EOS used in the other case.
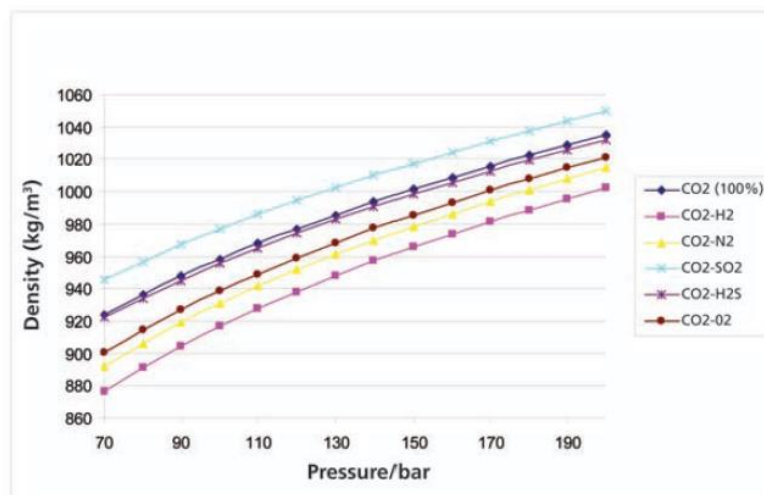
Figure 16: Density as a function of pressure at 4 °C using Span Wagner equation of state. (Energy Institute, 2010)

Another important property characterizing the supercritical state is viscosity. As already mentioned, viscosity values in the supercritical state have comparable order of magnitude with the values registered in the gas state.
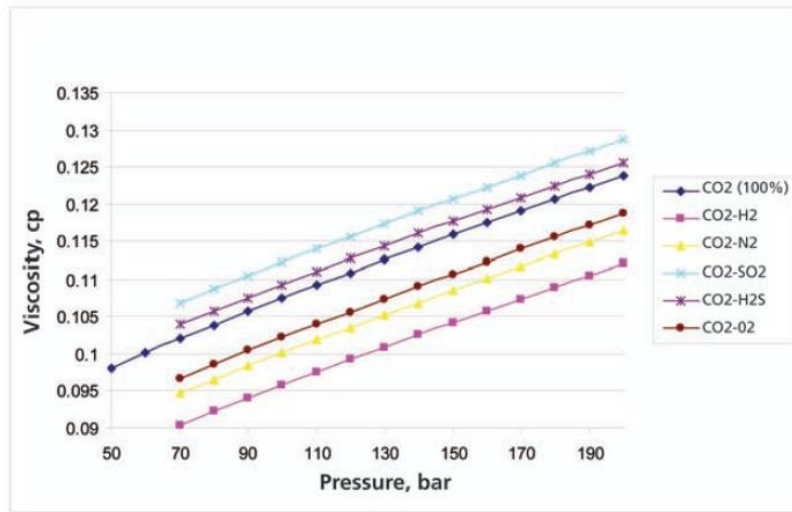
Figure 17: Viscosity as a function of pressure. (Energy Institute, 2010)

Viscosity and density in supercritical state guarantee respectively less expensiveness in transportation due to the low fluid dynamic resistance, and easy storage in smaller volumes which are two advantageous factors for our purposes.

Figure 17, not only illustrates the trend of CO_2 viscosity as a function of pressure at a constant temperature but also highlights the crucial aspect regarding the impact of contaminants on its properties. Figure 18, provides a better understanding of the influence of impurities on the behavior and properties of CO_2, as they can significantly affect the critical point occurring at different temperatures and pressure. In the context of CCUS, predicting the behavior of CO_2 results in a challenging task, and for this reason, it is recommended to use pure CO_2 as much as possible.
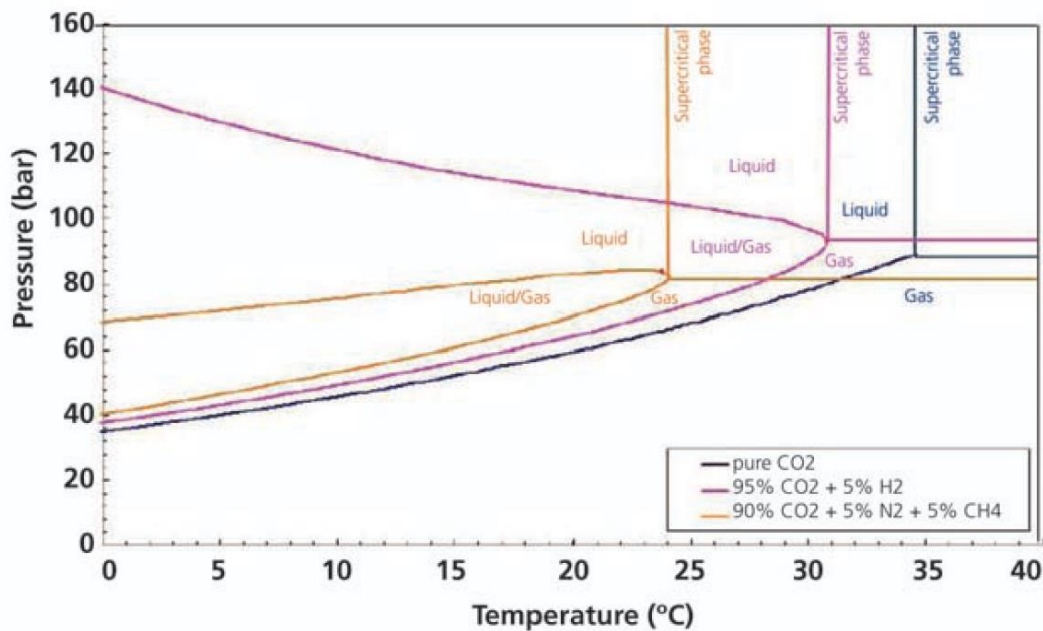
Figure 18: phase change diagram as a function of certain impurities. (Energy Institute, 2010)

3.2.2 Equation of State (EOS)

This topic is included in this chapter to have a comprehensive understanding of the behavior and properties of CO_2. Several scientific papers compare different equations of state (EOS) for supercritical CO_2, such as Zanzi S.'s master thesis (Zanzi S., 2017) and Liu B.'s Doctor of Philosophy thesis (Liu B., 2016a).

An equation of state (EOS) is a mathematical relationship that describes the thermodynamic behavior of systems by relating pressure, volume, temperature, and quantity of the substance. In the context of this thesis, it will be demonstrated that using the ideal gas law, which is the simplest EOS, is not accurate for predicting the behavior of CO_2. Specifically, the ideal gas law assumes that the gas is in a low-pressure and low-temperature condition, and its predictions of properties become inaccurate outside these ranges. However, the supercritical phase of CO_2 is very far away from the gas phase and as a result, a dedicated description of the various EOSs that can accurately capture the real gas behavior is mandatory. There are many EOSs available in the literature that can predict the behavior of supercritical CO2. Below, we will discuss the advantages and disadvantages of some of them:

The Span-Wagner Model

A model based on the Helmholtz coefficient approach, which employs a specific functional form to calculate the thermodynamic properties of supercritical CO_2, was developed by Span and Wagner in 1996. (Span & Wagner, 1996) This model provides highly accurate results for estimating the behavior of supercritical CO_2. However, it is important to consider that implementing this EOS in CFD (Computational Fluid Dynamics) simulations can be challenging. As mentioned in Zanzi S.'s master thesis and

Liu B.'s Doctor of Philosophy thesis, the implementation of this model can be tricky. Therefore, it is crucial to find an equation of state that achieves a good balance between accuracy and ease of implementation.

The GERG-2008 Model

This is a generalized EOS developed by GERG, a group for the Study of the Kinetics and Reaction Mechanisms of Gas, that considers the interaction between 21 natural gas components, including CO_2. (Kunz O. & Wagner W., 2012) The GERG-2008 model is recognized as one of the most accurate EOS to be used in the case of supercritical CO_2. However, integrating it into the software used for the numerical model requires the utilization of User Defined Functions (UDFs). The implementation of UDFs will be further elaborated in the chapter dedicated to the numerical model, emphasizing the complexity associated with their use.

The Peng-Robinson Model

One of the most commonly used EOS in the case of supercritical CO_2 phase was developed by Peng and Robinson in 1976 as an alternative to the Van Der Waals EOS, both cubic equations. (Peng D. & Robinson D., 1976) Despite the differences, the Peng-Robinson (P-R) equation includes a pressure correction term to improve the description of phase behaviors, such as the formation of condensates or phase transitions. In this thesis, the P-R equation is chosen as the EOS because it represents a good balance between accuracy and simplicity in its application compared to the above-mentioned EOSs. In addition, the P-R equation has already been implemented in the CFD software utilized for this thesis work, providing a solid starting point for obtaining accurate results. For completeness, the P-R equations are shown below, with the corresponding parameters and their unit of measurement presented in Table 8.

$$P = \frac{R\,T}{V_m - b} - \frac{a\,\alpha}{V_m^2 + 2bV_m - b^2} \tag{10}$$

$$a = 0.45724 \frac{R^2 T_c^2}{P_c} \tag{11}$$

$$b = 0.07780 \frac{RT_c}{P_c} \tag{12}$$

$$\alpha = (1 + k(1 - T_r^{\frac{1}{2}}))^2 \tag{13}$$

$$k = 0.37464 + 1.54226\omega - 0.26992\omega^2 \tag{14}$$

$$T_r = \frac{T}{T_c} \tag{15}$$

Table 8: Peng-Robinson EOS parameters.

parameters	items	measurement unit
Pressure	P	*Pa*
temperature	T	*K*
universal gas constant	R	*(8.314) J/mol K*
molar volume	V_m	*m^3/mol*
critical pressure	P_c	*Pa*
critical temperature	T_c	*K*

acentric factor	ω	-

However, to explicit the density (ρ) from the above formulation of the P-R equation, a modified model of the P-R equation was proposed below. (Haghtalab et al., 2011) The modified model will be used for analytic calculations of the density or as mentioned above, for the implementation of the User Defined Functions (UDFs) due to its simplicity in directly incorporating the density term.

$$P = \frac{RT\rho}{1-b\rho} - \frac{a\rho^2}{1+2b\rho-b^2\rho^2} \tag{16}$$

$$a = 0.45724 \frac{R^2T_c^2}{P_c} \alpha(T) \tag{17}$$

$$b = 0.07780 \frac{RT_c}{P_c} \tag{18}$$

$$\alpha(T) = (1 + k(1 - \sqrt{T_r}))^2 \tag{19}$$

$$k = 0.37464 + 1.54226\omega - 0.26992\omega^2 \tag{20}$$

$$T_r = \frac{T}{T_c} \tag{21}$$

3.3 Statistical Analysis of Pipeline Failure Probability

The release of carbon dioxide can occur throughout the entire CCS chain, including capture, transportation, and storage. In this regard, the estimation of failure frequency in CCS applications has been accurately analyzed by (Teng et al., 2021). However, this thesis specifically focuses on leakages of CO_2 in the supercritical phase, with particular attention given to the injection well where the phase change from gas to supercritical occurs. Table 9 presents the average yearly failure rates for different modules in CCS applications, indicating an expected failure frequency of 0.18 failures per year for the injection well. However, the failure rates vary depending on the size of the hole, as shown in Table 10, where smaller holes have a higher failure frequency.

The estimation of failure frequency is based on natural gas pipeline failure rates, considering various factors such as external interference, construction defects, corrosion, ground movement, and unknown causes. The total failure rate is calculated as the sum of these factors. Additionally, correction factors such as wall thickness, population density near the pipeline, depth of cover, and prevention methods are considered. Figure 19 provides an overview of the methodology used to calculate the total failure frequency for the CO_2 pipelines.

Table 9: Average yearly failure rate for each CCS sector. (Vendrig M. et al., 2003)

Module in CCS		Expected failure frequency (per year)	Leak every x years (year)
1	CO_2 recovery at source	1.5×10^{-1}	7
2	Converging pipelines	4.6×10^{-3}	217
3	Booster station	4.0×10^{-2}	25
4	10 km pipeline	3.4×10^{-4}	2941
5	Injection well	1.8×10^{-1}	6

Table 10: Failure frequency for each CCS module based on hole size. (Vendrig M. et al., 2003)

Module	Small (3–10 mm)	Medium (10–50 mm)	Large (50–150 mm)	Full-bore (>150 mm)
1	9.6×10^{-2}	5.1×10^{-2}	2.0×10^{-3}	5.6×10^{-3}
2	3.5×10^{-3}	8.8×10^{-4}	1.0×10^{-4}	1.5×10^{-4}
3	3.5×10^{-2}	3.8×10^{-3}	3.0×10^{-4}	8.8×10^{-4}
4	1.4×10^{-4}	9.5×10^{-5}	2.0×10^{-5}	8.5×10^{-5}
5	1.2×10^{-1}	5.3×10^{-2}	2.1×10^{-3}	5.8×10^{-3}
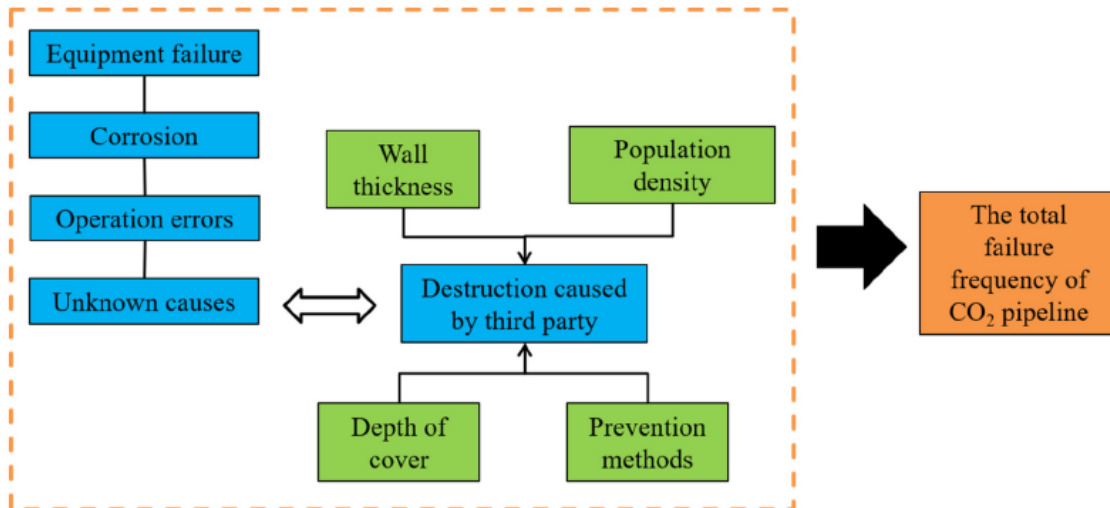
Figure 19: Sketch of the methodology used to calculate the total failure frequency of carbon dioxide pipelines. (Teng et al., 2021)

3.4 SBAM model

As mentioned earlier, conducting a Risk Assessment is mandatory in the case of industrial plants involving hazardous substances. Estimating the damaged area in case of accidents involving simulations is a crucial step because this measurement allows for the quantification of the risk. However, in the case of industrial plants, a huge number of accidental scenarios are possible, resulting in hundreds of potential scenarios. Nowadays, empirical methods are commonly used for simulating these scenarios due to their fast calculation and ease of use. Software such as PHAST and ALOHA enable the implementation of semi-empirical models, which can provide a simple estimation of the consequences area for QRA purposes with low computational effort. However, these methods are limited by the strict range of applicability. This topic is largely discussed by (Moscatello et al., 2021), and also it is evident in the results provided by (Gallo A., 2021). In addition, in congested environments, these methods tend to overestimate the resulting damaged areas because they do not consider the congested environment and the geometry of the domain, which significantly affects the evolution of events. For example, in the case of gas leakages, objects near the release region play an important role in the final gas dispersion. The gas, upon slamming against the surface of the object, disperses faster than a free jet simulated by the semi-empirical methods. On the other hand, Computational Fluid Dynamics (CFD) can be employed for these simulations, providing highly precise results for the risk estimation in QRA. However, CFD requires high computational resources, leading to long simulation times, as well as demands a certain technical competence. As a result, it is not usually used or is typically reserved for the most critical scenarios. To address these challenges, the Source Box Accident Model (SBAM) has been proposed, aiming to strike a balance between higher accuracy in the near jet region compared to the current empirical models, and reduced computational effort compared to full numerical approaches like CFD. (Moscatello et al., 2021)
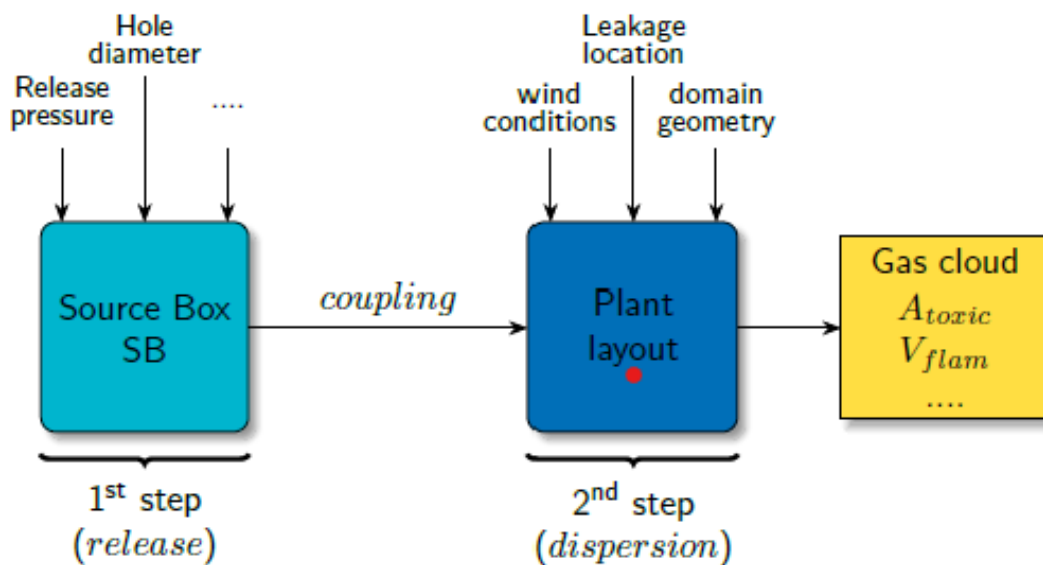
Figure 20: Schematic representation of SBAM model. (Moscatello A., 2023)

The SBAM method involves a two steps simulation based on CFD analysis to achieve highly accurate results. Figure 20 provides a schematic representation of the two steps that composed the SBAM model, which are the release and the dispersion phases. These steps are described in the following.

1° step

The first step focuses on the small domain near the release region, called Source Box (SB). The SB is characterized by high compressible effects, as stated in the under-expanded jet release theory. To account for space congestion, an obstacle is positioned in front of the release hole, following specific criteria depending on the components being represented. The size of the SB is determined based on the chosen criteria, which dictates that the compressibility effects near the obstacle are no longer significant. According to the under-expanded jet theory, this occurs after 10 times the Mach disk position. Therefore, the SB consists of a 3D simulation, comprising a nozzle located in the center of one face, a cubic region where the gas expands, and the obstacle. Consequently, certain input parameters need to be considered, including the release hole diameter, release pressure, gas type, obstacle distance, type, and dimensions. The SB introduces an innovative concept by exploiting the CFD, as it allows for storing the results of the SB simulation. These results can then be utilized as input parameters for the subsequent phase, which focuses on the dispersion simulation, enabling the simulation of various industrial layouts.
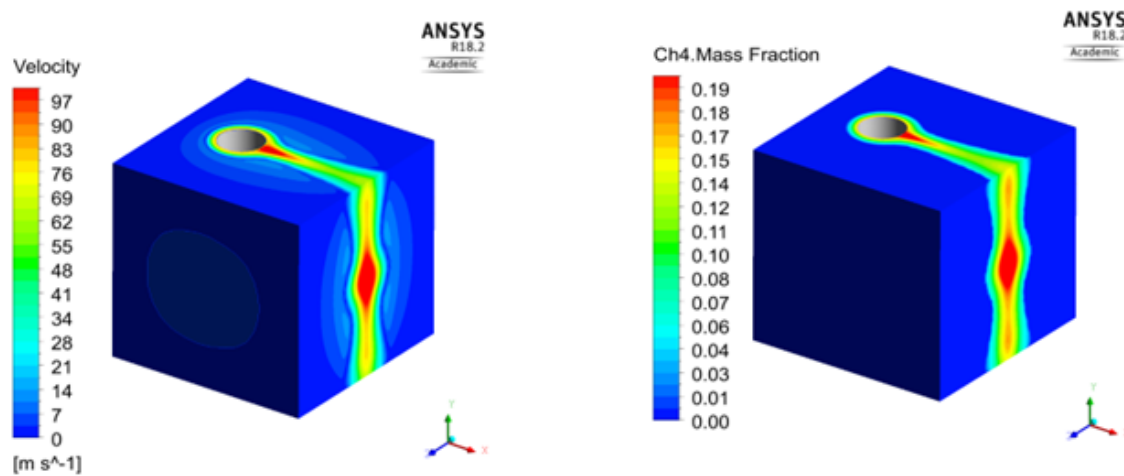
Figure 21: Source Box (SB) example result. (Moscatello A., 2023)

2° step

After the release phase, the simulation progresses to the dispersion phase, where the entire geometry of the industrial plant is considered. This phase considers additional parameters such as wind velocity, wind direction, and the position and direction of the release to accurately represent the accidental scenario. During the dispersion phase, the simulation provides results that include information about the distribution of the released fluid within the plant's geometry. Special attention is given to the concentration of hazardous substances, as this information is crucial for assessing the risk associated with accidents. By establishing a systematic approach for estimating the SB, as described earlier, it

becomes possible to analyze a large number of accidental scenarios in a shorter amount of time compared to traditional CFD simulations. Despite the reduced computational effort, this approach still maintains accurate results, ensuring a comprehensive analysis of the risk involved.
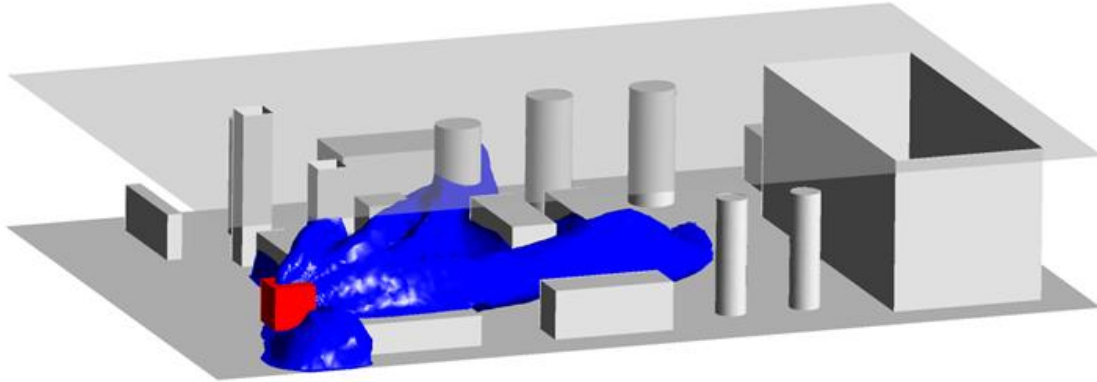
Figure 22: Release simulation of flammable volume in a platform with an SB as input. (Moscatello et al., 2021)

The coupling of the SB as input parameters in the dispersion simulation allows for the simulation of multiple incidental scenarios or simulations for different layouts of the same industrial plant without the need to recalculate the SB. This leads to significant time savings, as the dispersion simulation is easier and cheaper compared to the SB simulation. Moreover, it enables the creation of a library of SBs characterized by different input values, which can be utilized when necessary. However, it is important to note that the range of applicability of the SBAM method is still restricted. This includes limitations such as the pressure ratio range, the limited SB length, and its focus on steady-state analysis. Furthermore, the range of substances that can be modeled is currently limited, with only methane gas being introduced into the model.

In this regard, this thesis provides further support for the SBAM method by focusing on simulating the release of supercritical CO_2 for QRA purposes. The SBAM model primarily focuses on the loss of containment, which is a major accident scenario in energy industries particularly concerning gas leakages from high-pressure (HP) components. However, a literal review of the numerical modeling of supercritical CO_2 jets reveals limited information on this type of release and the numerical methods used to model it. The aim is to refine the model and equations that best describe this specific phenomenon. The SBAM model is implemented using ANSYS Fluent software, and a series of simulations concerning the concepts discussed above are described in the next chapter.

3.5 Strategic Framework

From the introductory chapter, specifically in Chapter 1.2, it is evident that the main objective of this thesis is to simulate supercritical CO_2 releases for QRA purposes in the context of repurposing oil platforms by implementing CCS technology. However, as the next chapter will demonstrate, there is a literature gap in terms of a specific approach to simulating supercritical CO_2 releases using CFD methods. Therefore, it is crucial to find a suitable method to simulate this phenomenon. Additionally, this thesis aims to extend

the range of applicability of the SBAM model by including CO_2 in the supercritical phase in the inventory of the model. SBAM is developed for accidental leakage scenarios in the industrial field, so utilizing the methodology employed in SBAM for simulating incidental release scenarios aligns with the context of this thesis.

Before implementing numerical models for the simulation of supercritical CO_2 releases, it is necessary to recap certain characteristics of the phenomenon in question. This recap will help in designing a specific approach to the problem and defining a suitable methodology. Specifically, it is important to consider the pressure values encountered in this specific application, the resulting physical state of CO_2, and the range of possible hole diameters where the releases can occur. These considerations are essential in defining the strategy for the work conducted in this thesis.

As mentioned in Chapter 2.3, with particular reference to Table 1, the minimum operating pressure within the reservoir is 79 bar, while the maximum fracture pressure of the reservoir is 145 bar. Therefore, during the storage operations of CO_2 in the reservoir, it is important to ensure pressure above the minimum value but with particular attention to the maximum pressure to ensure the structural safety of the well and reservoir.

This range of pressures, 79-145 bar, is above the CO_2 critical pressure, which is 73.8 bar, as mentioned in Table 7, so the CO_2 results in a supercritical phase.

Regarding the dimensions of the holes that typically occur during incidental leakage scenarios, as mentioned in Chapter 3.3, it is more probable to encounter small diameters (3-10 mm) instead of a Full-bore rupture (>150mm). However, the decision of the release diameter for the simulations is influenced by the scientific research investigated. To ensure that the model applied to the CFD simulations regarding the release of supercritical CO_2 is accurate, a comparison of the numerical model results and the data provided by scientific research is necessary. Although, in this phase, the diameters proposed by the experiment are used, they are of the same order of magnitude as the diameters discussed in the paragraph on break probability.

Concerning the CO_2 concentrations, as shown in Table 6, it is necessary to pay particular attention when the concentration of CO_2 exceeds a certain level. However, there are no concise rules, and the limits for CO_2 concentrations primarily depend on the duration of exposure. Generally, special attention is given when the concentration is higher than 3% for 20 minutes of exposure. However, exposure to 0.5% for more than 8 hours can lead to permanent damage to humans. It is important to stress that the rules depend on the competent authority and may vary from different countries, in principle however follow the indications that the scientific community has tested.

4 Literature Review

This chapter aims to discuss the numerical models available in the literature that has been developed for simulating the release of supercritical CO_2 from pipelines or vessels. The objective is to determine if accurate methods have been developed and adequately explained. Developing a numerical model to simulate accidental scenarios in industrial applications is a crucial step in the evaluation of risk. However, as will be demonstrated in this chapter, there is a literature gap related to the numerical modeling concerning the simulation of supercritical CO_2 releases. For this reason, in the absence of a just verified model, this thesis proposes the use of the SBAM model, which is specifically designed for the intended purpose. In general, validating a numerical model requires comparing experimental data with simulation results. Therefore, it is necessary to conduct a literature review on the experiments conducted on the release of supercritical CO_2 to fulfill this requirement.

4.1 Numerical Model

This paragraph aims to describe the numerical models available in the literature for simulating the release of supercritical CO_2 from high-pressure components such as pipelines and tanks. However, there is a limited number of scientific papers that specifically address the release of supercritical CO_2, and among those, only a few are considered particularly relevant.

One of the studies present in the literature was conducted by (Joshi Preeti, 2016) in their master's thesis at Osmania University. This study was supported by an experiment conducted by the DNV, which will be discussed in the next paragraph related to the experimental review.

The computational domain was divided into two parts: the first part considered the phase change of supercritical CO_2 and its release from a high-pressure pipe, while the second one focused on the large-scale dispersion of the fluid in ambient air. Both simulations were developed using ANSYS Fluent software. The initial data obtained from the experiment are listed in Table 11, and the following assumptions were made during the modeling phase:

- The inventory contains pure CO_2.
- The pipe was assumed to be insulated from the external environment, with no heat transfer.
- A short section of the pipe, 5.98 m in length, was considered without frictional effects, where the maximum changes occur in the upstream pipe. The pressure drop was entirely converted into the kinetic energy of the fluid.
- Water vapor or moisture condensation has not been included in the design together with the solid fraction after the nozzle.
- The ratio between the hole diameter and the pipe diameter was small, so there was no crack propagation.
- The ambient space was assumed to be short, precisely 10 m in length.

Parameter	Value/ Configuration
Release orientation	Horizontal
Release orifice diameter	1/2" (11.94 mm)
CO_2 pressure in the vessel at the beginning of the experiment	157.4 bar
CO_2 temperature in the vessel at the beginning of the experiment	148.1 ℃
Wind speed at heights 8.55m, 5.05m, 3.25m respectively	5.5 m/s, 5.2 m/s, 4.9 m/s
Atmospheric pressure	0.96 bar
Atmospheric temperature	7.8 ℃
Solid drop out	None
Release time duration	121 sec

The near-field region

The geometrical set-up of the near field was considered to be 2D axisymmetric with a pipe acting as a nozzle, which had a diameter of 11.94 mm and a length of 20 mm. The measurements of the remaining sections of the pipe and the surrounding regions are depicted in Figure 23.
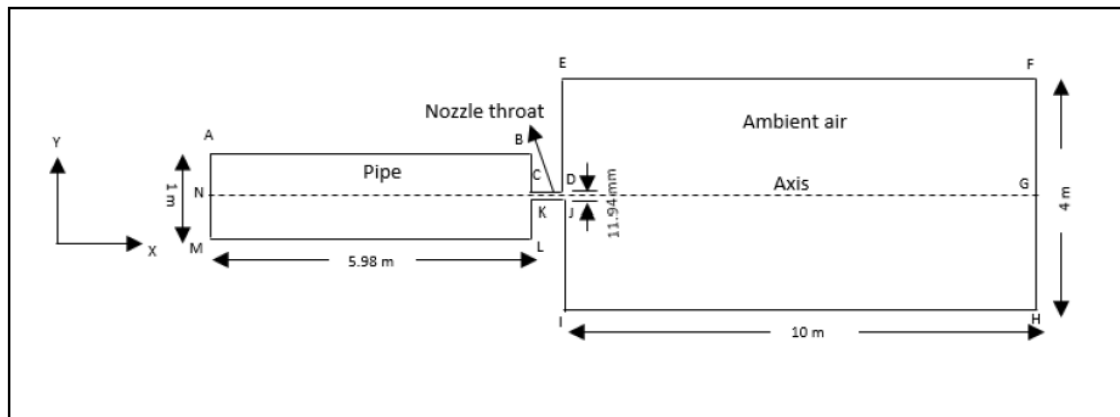
Figure 23: schematic representation of the near-field zone release. (Joshi Preeti, 2016)

A series of evenly distributed meshes were proposed for the near-field region. However, after a grid independency analysis concerning the deviation of the X-directional velocity, the mesh containing 0.41 million cells was chosen because represents a good balance between accuracy and computational effort, as shown in Figure 24.
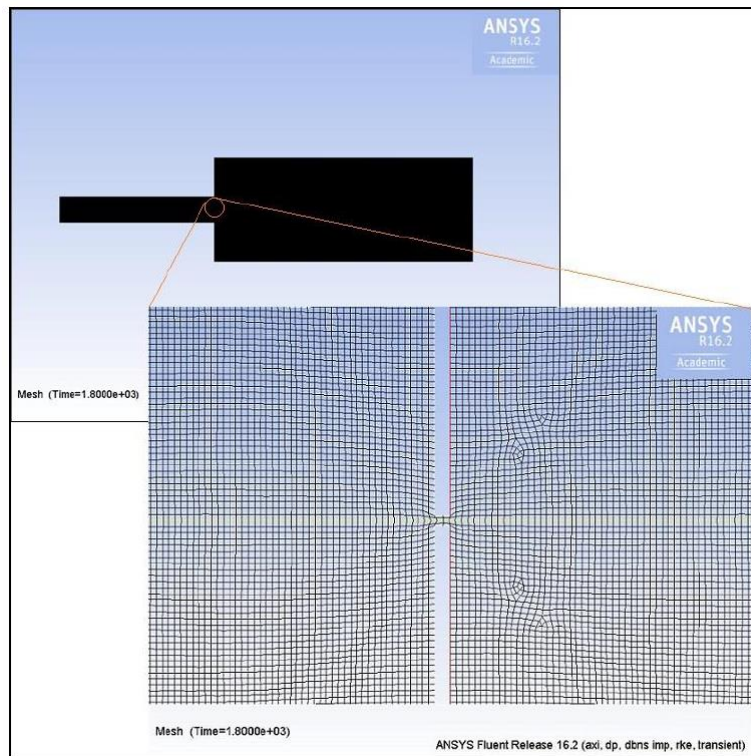
Figure 24: Graphical representation of the near-field region mesh. (Joshi Preeti, 2016)

The boundary conditions employed for the mesh were as follows:

- Pressure Inlet Boundary condition on the AM edge with pressure and temperature values specified in Table 11.
- Pressure Outlet Boundary condition on the FH edge with an ambient pressure of 0.96 bar and a temperature of 7.8°C.
- Wall Boundary condition on the AF and HM edges, with a no-slip condition and a default roughness of 0.5.

A transient simulation was carried out for 1800 seconds, assuming it to be sufficient time to achieve a steady state flow. A density-based solver was selected, along with a *Realizable k-ε* model for the turbulence modeling. The behavior of the CO_2, including the CO_2 vapor-liquid transition, was predicted using the real gas Peng-Robinson EOS. For the transient formulation, an implicit second-order scheme was chosen, with a Courant number of 0.5 to ensure solution convergence. The residuals were monitored and kept below 0.001 for convergence.

The results regarding the release phase are as follows:

- The jet structure is represented using a contour plot of the Mach number in the release region, as shown in Figure 25.
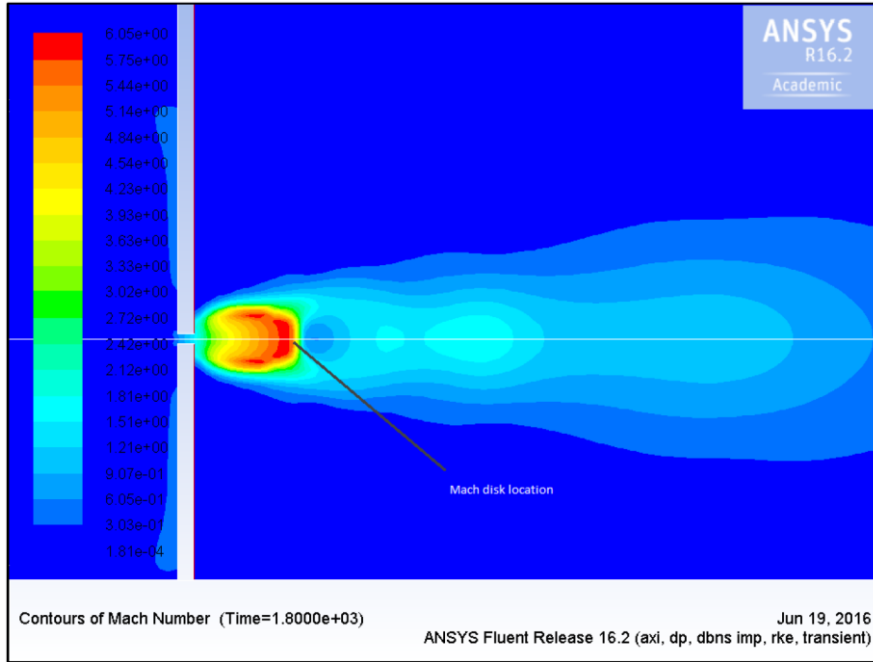
Figure 25: Mach number representation. (Joshi Preeti, 2016)

In this regard, the *Realizable k-ε* model was chosen instead of the *Standard k-ε* model due to its better performance near the nozzle leak. In this representation, the Mack disk is positioned at 0.113 m, which corresponds to 9.5 times the diameter of the nozzle.

- The mass flow rate at the nozzle exit was calculated as the average value over a 20-second interval. During this time, a decrease in the average mass flow rate was observed. However, in the end, the average value of the mass flow rate was determined to be 3.427 Kg/s, resulting in an overestimation of 1.09 % compared to the average mass flow rate recorded during the replicated experiment. This result is displayed in Table 12.

Table 12: Mass flow rate results in the near-field region. (Joshi Preeti, 2016)

Time (s)	Mass Flow Rate (kg/s)
20	3.776
40	3.687
60	3.579
80	3.523
100	3.193
121	2.733
Average from Calculations	3.427
Average from Experiment	3.39
% Error = +1.09	

- The temperature distribution shown in Figure 26 indicates that the region near the Mach disc exhibited the lowest temperature value (below 173 K), suggesting that the liquid droplets underwent phase transition and condensed into the solid phase.
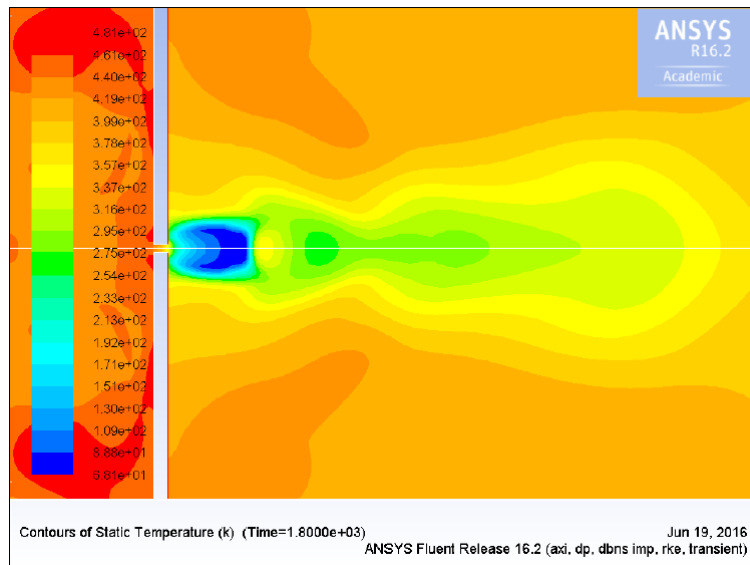
Figure 26: Temperature distribution in the near-field release region. (Joshi Preeti, 2016)

- The velocity profile along the central line, as depicted in Figure 27, reveals that the velocity reaches the highest value in the Mach disc region (774 m/s), and gradually decreases to a constant velocity of 9 m/s in the near-field release region. The outlet nozzle is located at 6 m, where a discontinuity in the velocity profile was observed due to the CO_2 expansion during the release.
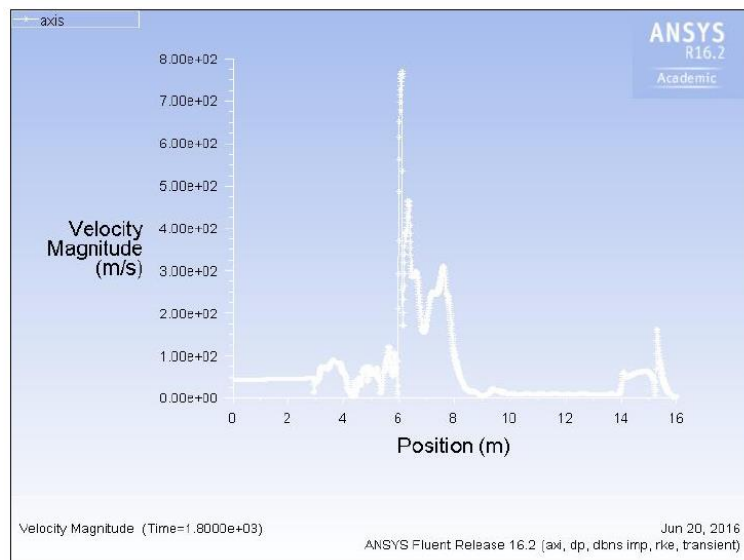
Figure 27: Velocity profile along the center line. (Joshi Preeti, 2016)

Other notable results are as follows:

- The initial volume of the tank, $V_0 = 6.3 \ m^3$.

- The density at the starting point (at P_0 = 157.4 bar and T_0 = 148.1 °C) is ρ = 250.13 Kg/m^3 (Span and Wagner 1996)
- The total mass of the tank, M_{tot} = 1575.8 Kg.
- Based on the given mass flow rate, the inventory was depleted by 26.3% in the first 121 seconds. At this rate, it is estimated that the vessel will be emptied in 8 minutes.

The dispersion region

The results obtained from the near-field region model were utilized as an initial reference for the dispersion model, which encompasses a 3D domain measuring 100 m x 80 m x 50 m. The left face of the domain contained the inlet boundary conditions for both CO_2 and wind. Specifically, the area designed as the CO_2 inlet was larger compared to the dimensions of the previously described release nozzle, approximately 0.053 m^2. Furthermore, the CO_2 inlet point was positioned at 0.041 m from the inlet wall and at 1.1 m above the ground. The remaining faces of the domain were assigned as ground and wall boundary conditions.
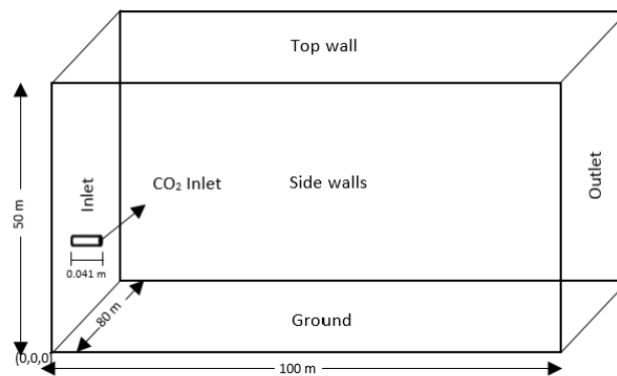
Figure 28: Dispersion model computational domain. (Joshi Preeti, 2016)

The boundary conditions applied to the computational domain are as follows:

- Inlet Boundary condition for the CO_2 was set as a mass flow rate of 3.4274 Kg/s and a vapor mass fraction of 0.887 at 194 K.
- Inlet Boundary condition for the wind was divided into two case studies. In the first case, a constant velocity of 5.51 m/s was used. In the second case, a UDF (User Defined Function) was implemented to incorporate a power law for the wind velocity profile.
- Pressure outlet condition setting the pressure and temperature at ambient conditions.
- Top and two side walls as symmetry boundary conditions with no shear slip and normal flux set to zero.
- The ground was treated as a wall boundary condition with no shear slip and a constant roughness of 0.5 points.
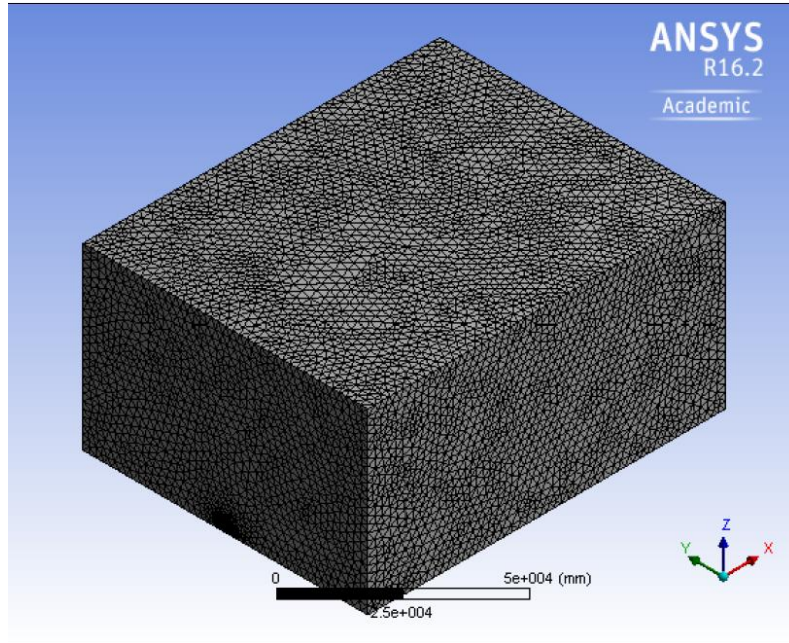
Figure 29: Dispersion model mesh. (Joshi Preeti, 2016)

The mesh proposed in Figure 29 was created by initially setting the minimum element size to 2.8 mm around the CO_2 inlet pipe. The mesh was constructed to ensure an orthogonal quality close to 1 and skewness close to 0. Additionally, Adaptive Mesh Refining (AMR) was applied in the vicinity of the inlet area to define the mesh density based on the step gradient near the fluid source.
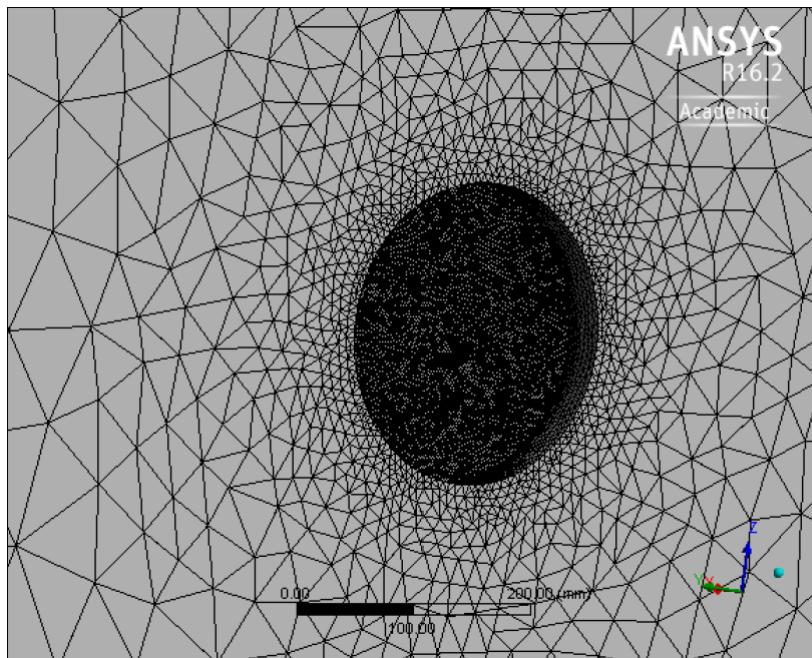
Figure 30: Zoom on the CO_2 inlet zone. (Joshi Preeti, 2016)

In this regard, a pressure-based model was employed for steady and transient simulations, with the support of the *viscous k-ε* model used to solve the turbulent model.

Initially, a steady state simulation was conducted, where the wind profile was imposed using a UDF. After achieving a uniform wind profile, a transient simulation was carried out for 121 seconds using the results from the release simulation as input parameters.

The dispersion model provided the following results:

- Figure 31 presents a series of comparisons between the experimental data on CO_2 concentration and the simulation results obtained using two different methods for the wind profile. The concentration showed a generally good prediction. However, for the graphs related to 10, 15, 20, and 40 meters, the simulation overpredicted the concentration. In addition, Table 13 reports the maximum CO_2 concentration levels for both the experimental data and the simulation results in ANSYS Fluent, highlighting the overestimation at measurement points located further away. It is important to note that the simulation results represent time-averaged values based on a time interval of 20 seconds.
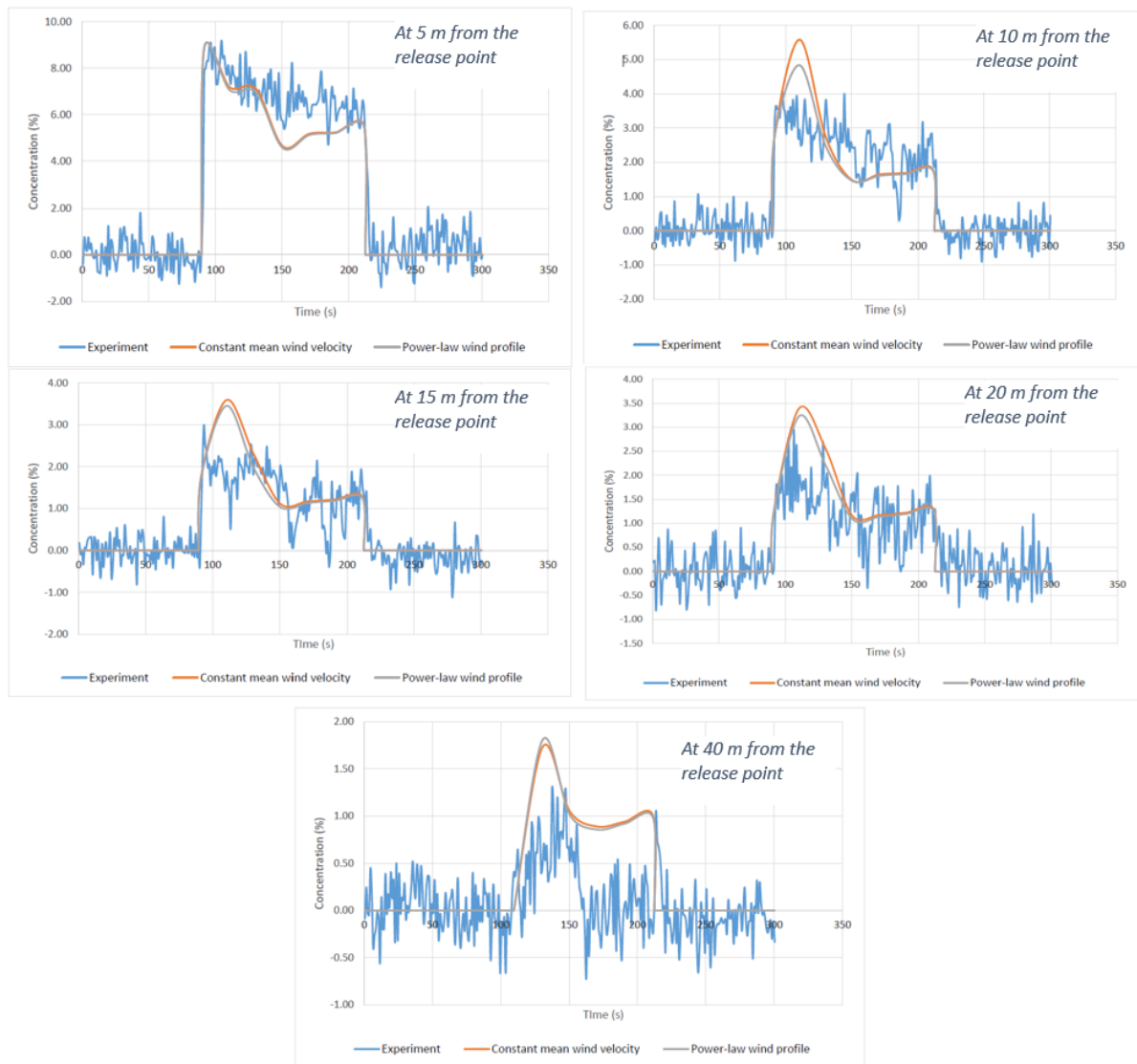
Figure 31: CO₂ concentrations at 5, 10 and 15, 20, and 40 m from the release point for two different UDFs in comparison with the experimental data. (Joshi Preeti, 2016)

Table 13: Maximum CO$_2$ concentration level for data experiment and simulation results. (Joshi Preeti, 2016)

Distance downstream (m)	Maximum concentration (% vol) (Experiment)	Maximum concentration (% vol) (20 seconds Time averaging)- FLUENT
5	9.185	8.870
10	4.061	5.582
15	2.987	3.591
20	2.951	3.395
40	1.299	1.731

- An analysis of concentration as a function of distance was proposed in Figure 32, with the corresponding graphs generated at 10 and 20 seconds after the release. It can be observed that the concentration rapidly decreases near the inlet conditions over time, but increases in the far field zone. On the other hand, Figure 33 illustrates the graphical representation of CO$_2$ concentration at different time intervals.
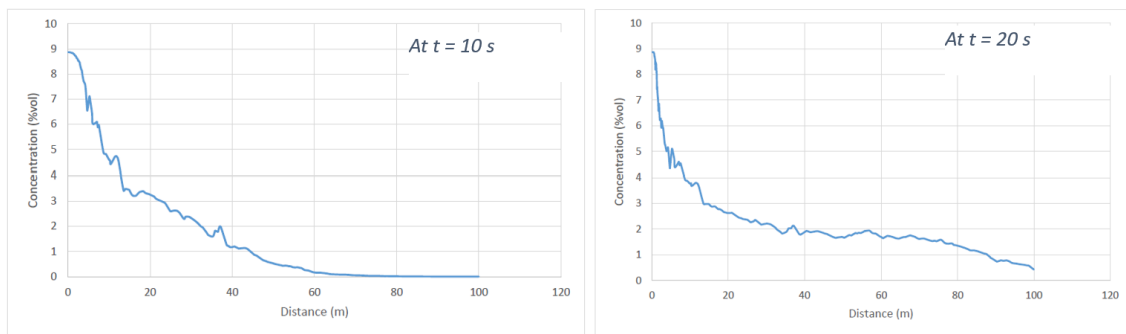
Figure 32: CO$_2$ concentration vs distance at 10 and 20 seconds. (Joshi Preeti, 2016)
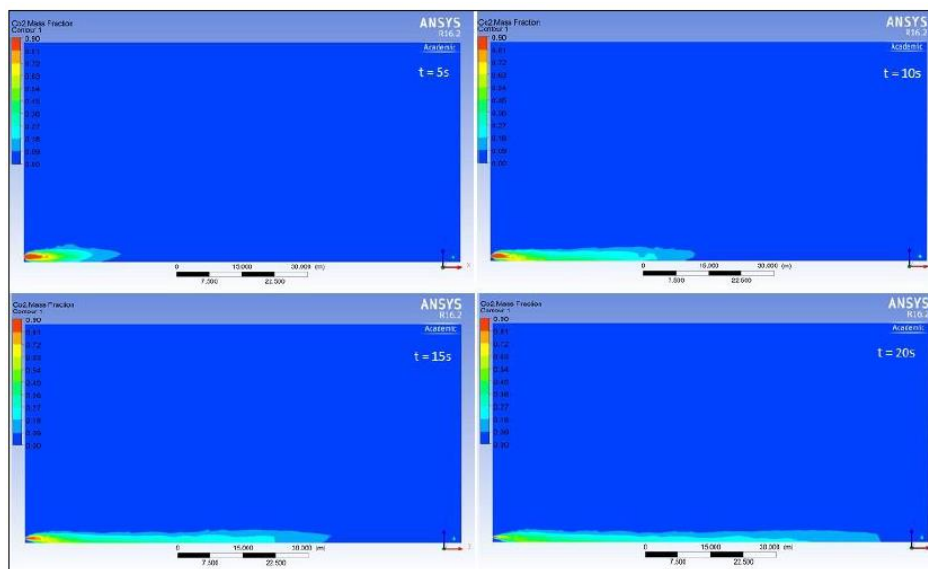
Figure 33: Graphical representation of CO$_2$ concentration. (Joshi Preeti, 2016)

The dispersion region in the presence of obstacles

Even more interesting for this thesis was the analysis of the dispersion region conducted in the presence of obstacles. The obstacles had dimensions of 10 m x 10 m x 2 m (height) and they were placed at varying distances from the release point. Specifically, the proposed domain is represented in Figure 34 and Figure 35, with three obstacles positioned at distances of 8 m and 20 m from the release point.
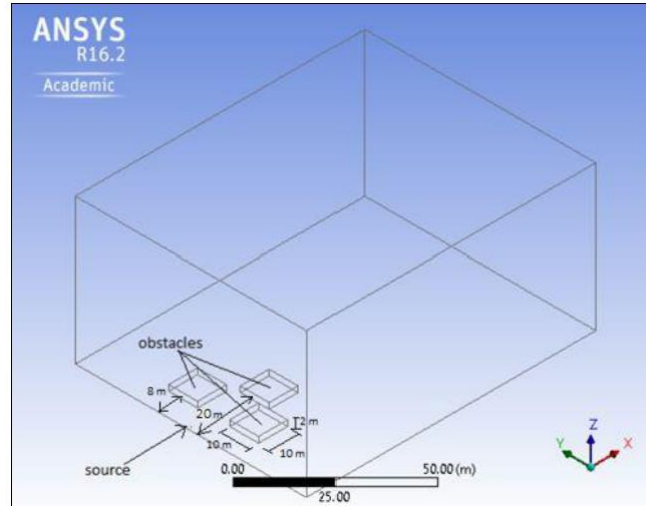
Figure 34: Geometrical representation of the dispersion case in the presence of obstacles. (Joshi Preeti, 2016)
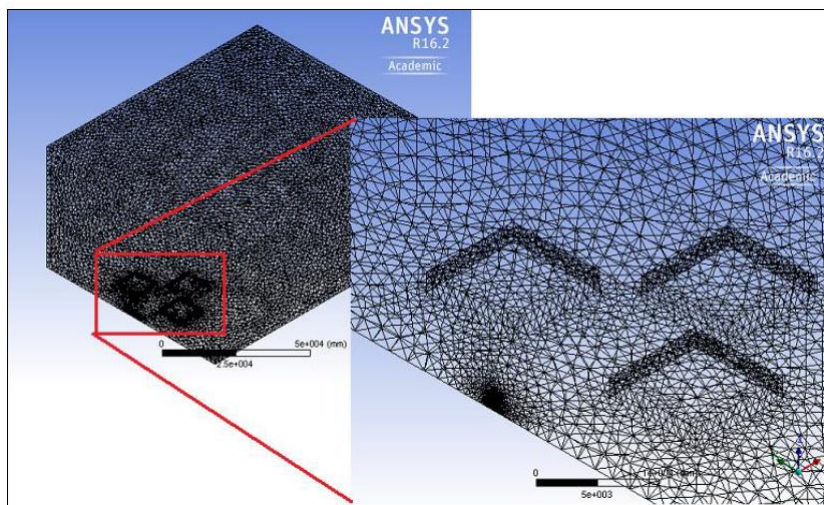
Figure 35: Mesh related to the domain of the dispersion case in the presence of obstacles. (Joshi Preeti, 2016)

Also, in this case, similar to the dispersion case, a preliminary steady-state simulation was conducted for the convergence of the wind profile. Subsequently, a transient simulation of 20 seconds was performed to model the release of the CO_2, using a mass flow rate as a boundary condition for the simulation.

The results obtained in this scenario are presented below, specifically:

- A concentration analysis along the centerline after 20 seconds is reported in Figure 36. It is important to note that the graph displays a discontinuity in the line due to the presence of an obstacle. Immediately after the obstacle, the concentration was

below 3%, on the other hand, the concentration increased to 6% in front of the obstacle.
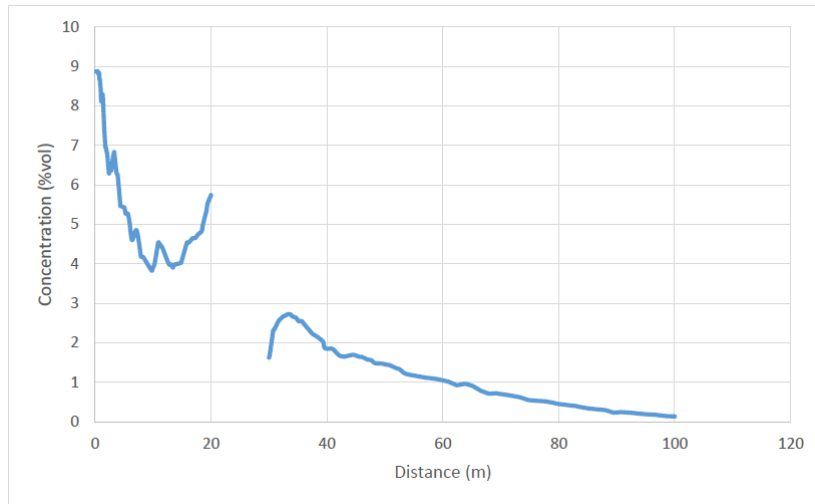
Figure 36: CO$_2$ concentration along the centerline after 20 seconds. (Joshi Preeti, 2016)
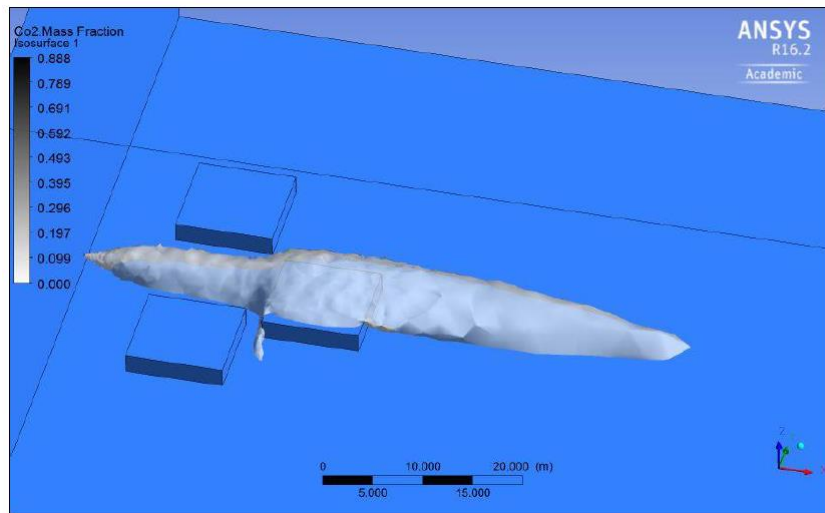
Figure 37: Graphical representation of the CO$_2$ plume after 20 seconds. (Joshi Preeti, 2016)

Another important reference regarding the simulation of an under-expanded CO$_2$ jet that needs to be mentioned was described in Liu B.'s Doctor of Philosophy thesis. (Liu B., 2016b) This research not only proposed the simulation of pure supercritical CO$_2$ but also the simulation of a mixture with CO$_2$ as the main component. However, for clarity and simplicity, only the part related to pure CO$_2$ is presented below.

To predict the properties of the CO$_2$, a user-defined real gas model was implemented in the software, and a Peng-Robinson real gas EOS was used for pressure and temperature calculations. To validate the user-defined real gas model, an air jet simulation was compared with a corresponding experiment. The same settings will also be employed for the simulation involving the release of CO$_2$, which will be discussed below.

For the release simulation, a 2D axisymmetric computational domain consisting of 70.000 cells was selected, as shown in Figure 38.
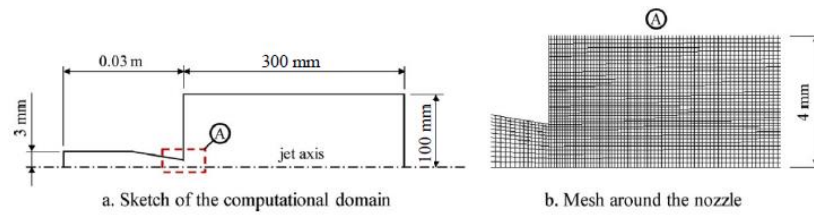
Figure 38: computational domain with a zoom on the nozzle. (Liu B., 2016b)

The following is a description of the software configuration regarding the release of CO_2 from a nozzle with a diameter of 2.7 mm.

A pressure-based simulation with the use of the *Standard k-ε* model was carried out for solving the turbulent model. A pressure inlet of 6.6 atm was selected as the boundary condition. The results are listed below:

- The temperature distribution near the release zone exhibited the Mach disc, with the lowest temperature recorded along the central line, around 113 K, as a result of the Joule-Thompson effect.
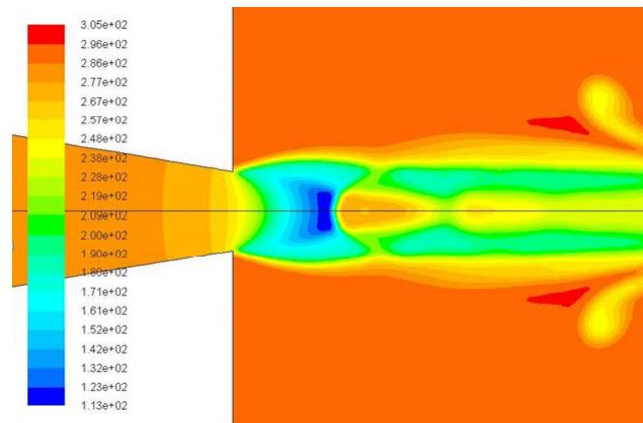
Figure 39: Distribution temperature near the release zone. (Liu B., 2016b)

- Additionally, the velocity distribution near the release zone exhibited the formation of the Mach disc, where the highest velocity of approximately 498 m/s was observed in this vicinity. However, the exit nozzle velocity was nearly 220 m/s, which is close to the speed of sound, indicating the presence of discrepancies. If the condition of the nozzle is considered chocked, the speed of sound should have been recorded, this discrepancy was shown in Figure 41.
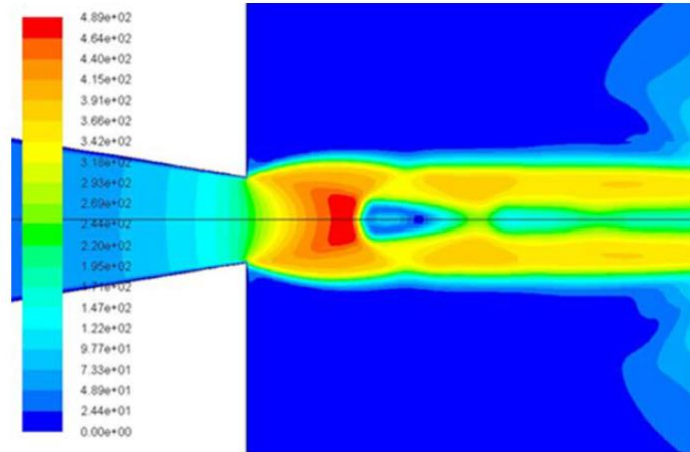
Figure 40: Velocity distribution in the near-field release region. (Liu B., 2016b)
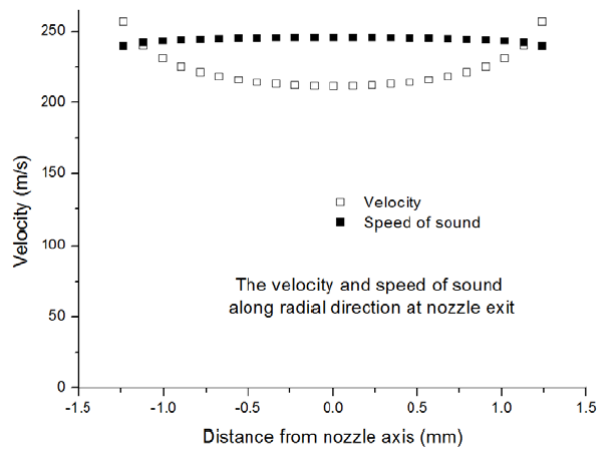
Figure 41: Discrepancy between the speed of sound and the velocity along the radial direction at the nozzle exit. (Liu B., 2016b)

- At the Mach disk discontinuity was registered the higher Mach number value, nearly 2.8.
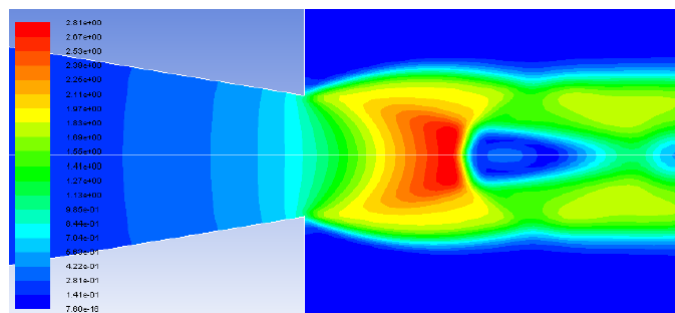
Figure 42: Mach number distribution in the near-field release region. (Liu B., 2016b)

- A comparison between velocity and Mach number was proposed in Figure 43 below:
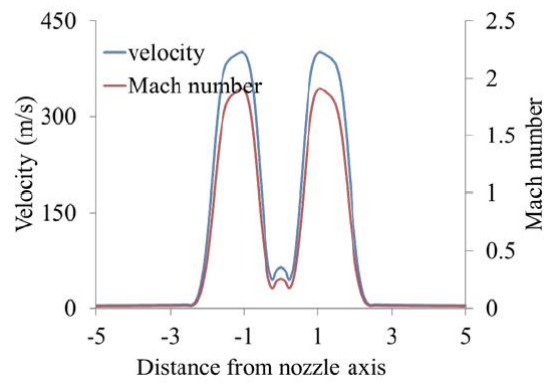
Figure 43: Comparison between velocity profile and Mach number near the nozzle. (Liu B., 2016b)

- The pressure distribution near the nozzle region is proposed in Figure 44, indicating a region with pressure lower than the ambient pressure as a result of the Mach disc discontinuity.
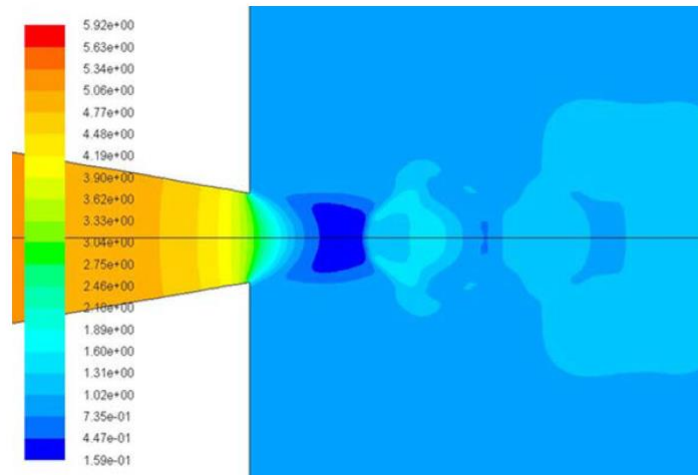
Figure 44: Pressure distribution near-field release region. (Liu B., 2016b)

4.2 Experimental Data

This section provides a summary of recent scientific research papers regarding the accidental release of supercritical CO_2 from high-pressure components. Numerous research programs have investigated this phenomenon, focusing on various aspects of the release. Typically, experiments involve tanks or pipelines filled with CO_2 up to the desired pressure and heated to achieve the supercritical condition. The tanks and pipelines are joined with a nozzle that acts as a hole, simulating the rupture of pipelines or vessels and allowing for the rapid release of supercritical CO_2 into the external environment within seconds, depending on the diameter of the nozzle.

The objective of this paragraph is to investigate such experiments concerning the release of supercritical CO_2. The description of the experiment and subsequent analysis of the collected data will be crucial for developing a numerical model that aims to replicate the experiment. This will be followed by a comparison between the experimental data and the results obtained from the numerical model. The purpose of this comparison is to validate the numerical model by assessing the agreement between the numerical results and the experimental data, ensuring that equations, boundary conditions, and other constraints applied to the numerical model represent an acceptable compromise between results accuracy and simplifications applied to the numerical model. Once the numerical model is verified, it will be possible to utilize the same equations and conditions for further analyses, such as steady-state modeling of the accidental release of supercritical CO_2 in partially confined spaces.

The experiments analyzed in the next section were selected based on their clear data, allowing for a comparison between the recorded experimental data and the numerical model results. However, there is a limited number of scientific papers specifically dedicated to the release of supercritical CO_2.

The experiment conducted by (Teng L. et al., 2021) was chosen for its detailed description of the near-field structure of the jet release. Additionally, this research provides easily interpretable graphs that are relevant to the research conducted in this thesis, as they are of fundamental importance in determining the appropriateness of the models used in the numerical model. The research focuses on a novel experimental setup designed to study the structure of the under-expanded jet created by the high-pressure release of CO_2. Data collection was carried out using various instrument measurements that recorded several essential parameters for jet analysis, including pressure, temperature, concentration, velocity, and mass flow rate in the near-field release region. Table 14 provides information on the distance at which each instrument of measurement is located from the orifice along the axial direction (along the centerline). The tags proposed by the authors are also used in numerical models proposed in this thesis to maintain consistency between the experimental data and the numerical model results. The instrument reliability and their typology have been omitted from the reader because this thesis's work is focused on the numerical modeling of the phenomenon. Furthermore, the setup and procedures of the experiment are only briefly described to provide a general overview since the aim is to validate the numerical model. Moreover, the sources of the articles are considered reliable.

Table 14: Representation of the positions of the instruments from the release point. Inspired by (Teng L. et al., 2018)

measure	tag	distance from the orifice	units of measurement
Temperature	t3	3	cm
Temperature	t4	6	cm
Temperature	t5	11	cm
Temperature	t6	19	cm
Temperature	t7	29	cm
Temperature	t8	49	cm
CO_2 concentration	c1	50	cm
Temperature	t9	69	cm
Temperature	t10	99	cm
CO_2 concentration	c2	100	cm
Velocity	v	105	cm
Temperature	t11	129	cm
Temperature	t12	169	cm
CO_2 concentration	c3	200	cm
Temperature	t13	209	cm
CO_2 concentration	c4	350	cm
Temperature	t14	259	cm

The experiment was conducted by using a vessel filled with CO_2 up to 80 bar. During the charging operation, the CO_2 temperature was decreased by a refrigeration unit, and after that, a thermostatic water path was used to accurately regulate the temperature. During the experiment, the pressure inside the vessel was measured and recorded, and, as a result, the recorded pressure data exhibited the typical behavior of a tank being emptied. However, as the vessel emptied during the release phase, the pressure inside decreased, causing all the recorded parameters to vary with time.

Furthermore, only circular orifice patterns are examined, while rectangular ones are not considered. This choice is justified by the fact that the Mach disc geometry is better visualized in the case of circular orifices. The high-pressure release of CO_2 was carried out using three different diameter sizes for the circular holes, respectively d=1, 2, and 5 mm. However, most of the available data is associated with the first and second diameter sizes. Thanks to a high-speed camera, it was possible to capture the supercritical CO_2 under-expanded jets that are shown in Figure 45 and Figure 46. These figures describe the evolution of a supercritical CO_2 release respectively at 7,7 MPa and 36°C using a circular hole with a diameter of 5 mm, and at 8 MPa and 313 K using a circular hole with a diameter of 2 mm. In addition, Figure 45 represents the release in different time steps to better visualize the structure of the under-expanded free jet. It is important to underline that after 127,7 milliseconds it is difficult to appreciate the structure of the flow that releases because contains a big amount of dry ice.
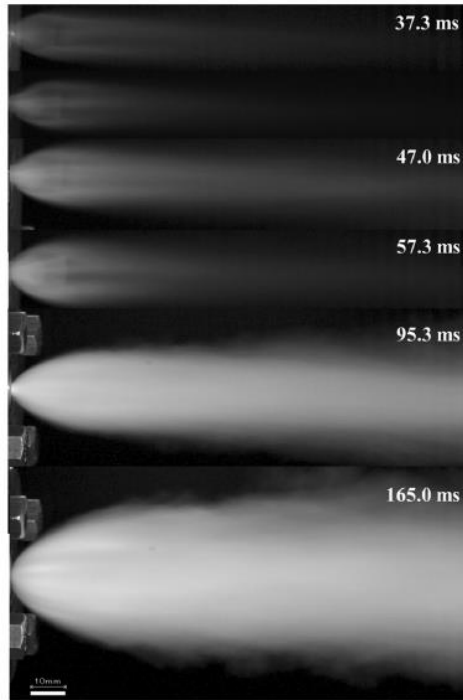
Figure 45: Evolution of release of supercritical CO$_2$ at 7,7 MPa and at 36 °C with a hole diameter of 5 mm. (Teng L. et al., 2018)
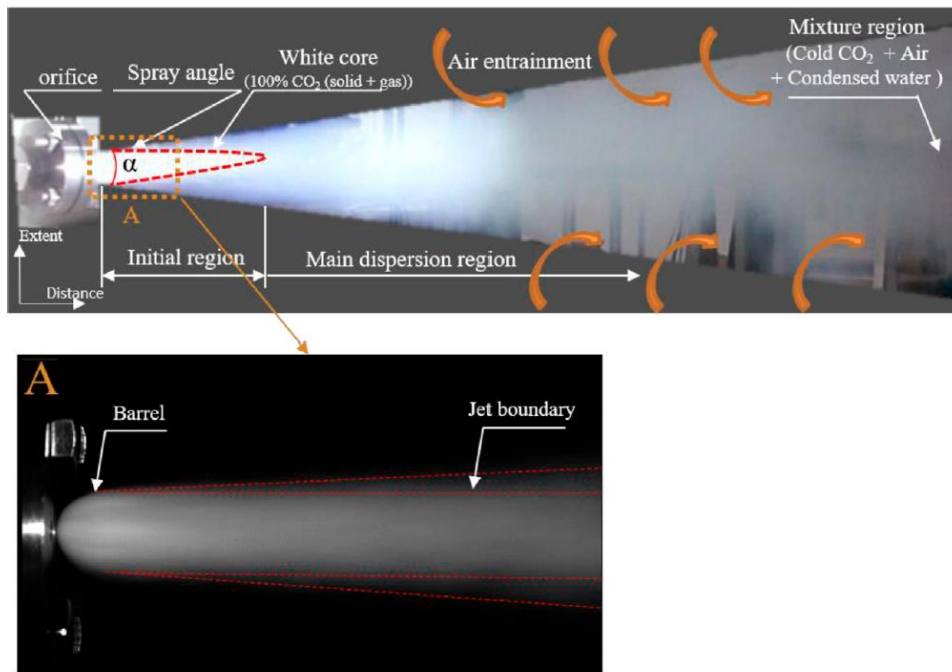
Figure 46: Evolution of release of supercritical CO$_2$ at 8 MPa and 313K with a hole diameter of 5 mm. (Teng L. et al., 2021)
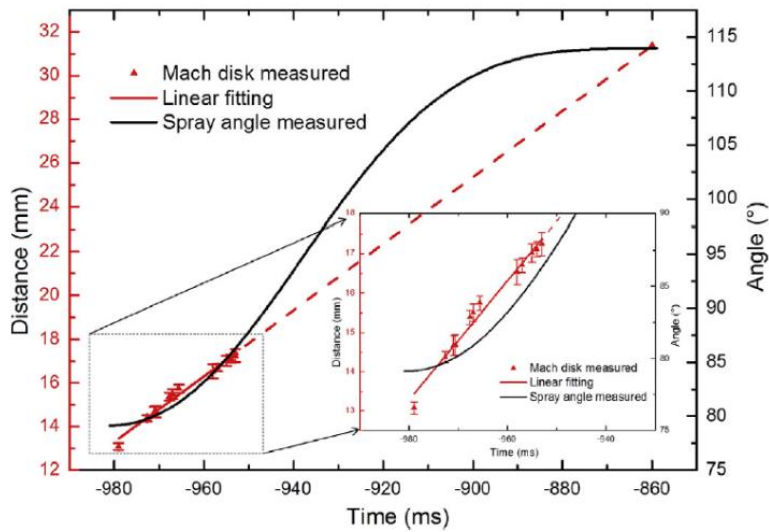
Figure 47: Mach disc positions measured during the discharge from a diameter hole of 5 mm, at P=7.7 MPa and T=36 °C. (Teng L. et al., 2018)

The Mack disc is the most important phenomenon that can be observed in the near region of the release point, and its shock waves influence the characteristics of the gas flow. Therefore, it is interesting to measure the distance of the Mach disc from the hole, as shown in Figure 47. It is important to note that the discharge time in the figure is represented as negative because the experiment employed a specific camera acquisition system known as the "mid-trigger mode acquisition system". As mentioned in the theoretical section, it is also possible to use analytic equations to predict the distance of the Mach disc. Consequently, Figure 48 presents a comparison between the results obtained from the analytic formulation and the experimental results using a release diameter of 2 mm. The analytic approach underestimates the Mach disc's position, mainly due to the phase transition of the supercritical CO_2 during the release phase.

Figure 48: Mach disk positions measured with a diameter of 2 mm in different pressure conditions and comparison with the analytic calculation. (Teng L. et al., 2021)

For this comparison, the research study in question has used the analytic equation, developed by (Ashkenas H. & Sherman F. S., 1966):

$$\frac{x_m}{d_e} = 0.67 * \sqrt{\frac{P_0}{P_\infty}} \tag{22}$$

Another important characteristic, according to the theory of under-expanded jet releases, is shown in Figure 49. This figure presents a pressure-temperature diagram for different types of release hole geometry. It highlights that the release phenomenon can be assumed almost isothermal in the initial stage. To enhance comprehension of the three distinct stages, Figure 50 is presented, illustrating a graph that describes the discharge pressure measured in the upper section of the vessel containing the supercritical CO_2. This graph provides insights into the pressure behavior and indicates the time scale involved in the experiment. In particular, the first stage corresponds to the depressurization of the supercritical CO_2. which rapidly decreases to the critical pressure.
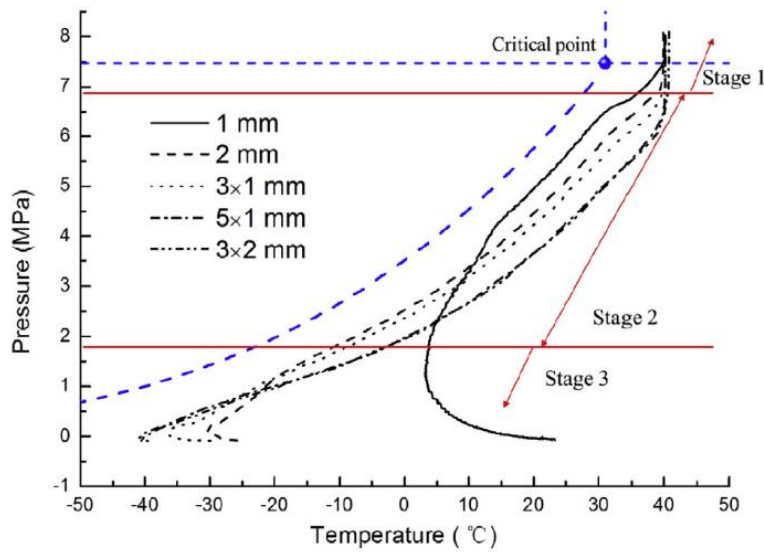
Figure 49: P-T diagram that represents the discharge stage using different hole diameters. (Teng L. et al., 2018)
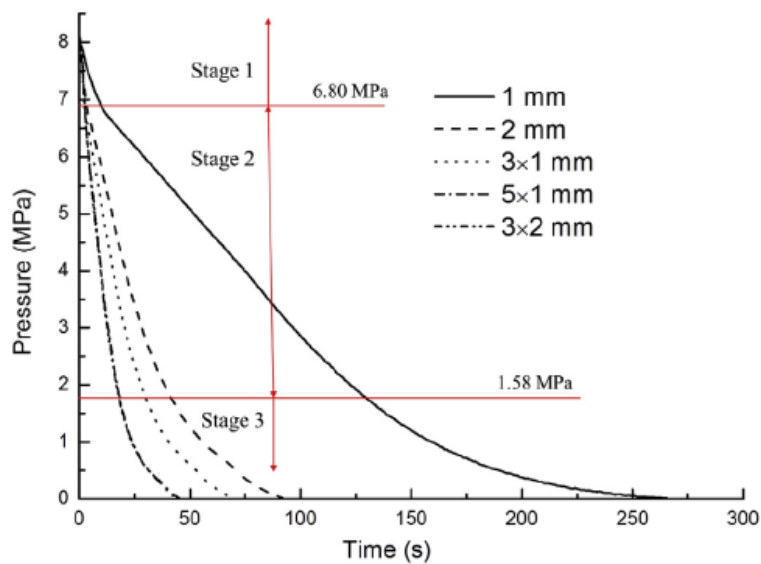
Figure 50: Pressure in the vessel during the discharge. (Teng L. et al., 2018)

The temperature evolution during the release of supercritical CO_2 with a hole diameter of 1 mm is described in Figure 51. The positions of the measurement points are described in Table 14. At the beginning of the discharge, the temperature decreases rapidly, reaching the lowest value of -41.9 °C after 20 seconds. This temperature profile is attributed to the shock wave generated by the Mack disc structure created due to the high-pressure difference between the supercritical CO_2 and the ambient pressure. It justifies the formation of dry ice.
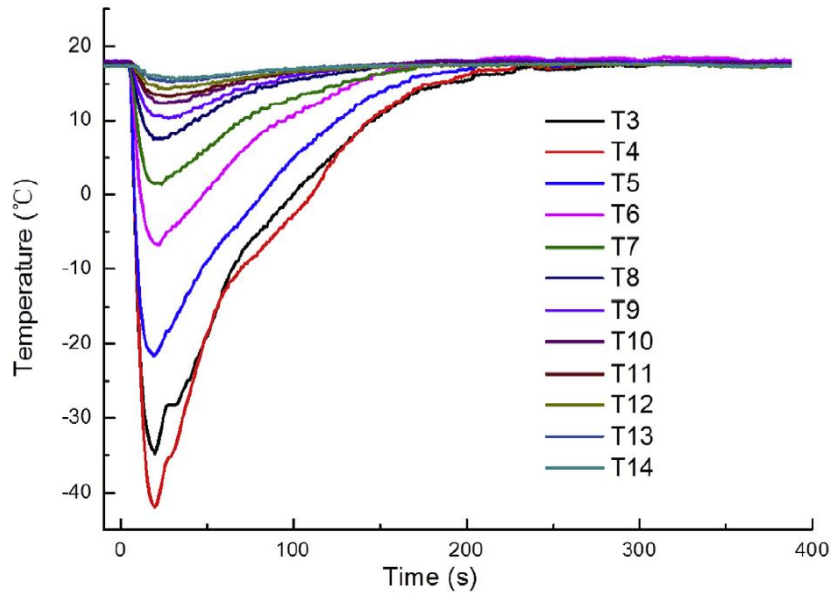
Figure 51: Temperature profiles of the release of supercritical CO$_2$ using a hole diameter of 1 mm. (Teng L. et al., 2018)
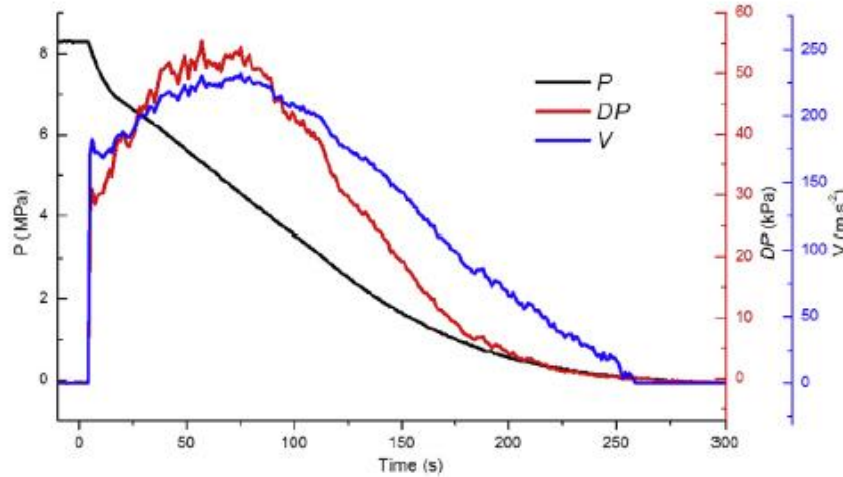
Figure 52: Discharge pressure, differential pressure, and velocity profile for the case with a hole diameter of 1 mm. (Teng L. et al., 2018)

Figure 52 shows various parameters as a function of time, specifically related to the case with a hole diameter of 1 mm. The release pressure, represented by the black line in the graph, has been previously described. The red line represents the differential pressure, which is necessary for estimating the velocity profile at a distance of 3 mm from the

release hole. The velocity profiles during the release are calculated using the equation below, where ΔP denotes the measured differential pressure near the jet release, and ρ represents the density of the supercritical CO_2 calculated using the Peng-Robinson Equation of State. The implementation of the Peng-Robinson EOS strikes a good balance between result accuracy and ease of implementation, as discussed in this thesis and another publication by the same authors (Teng L. et al., 2021).

$$V = \sqrt{2 * \frac{\Delta P}{\rho}} \qquad (23)$$

Furthermore, this scientific paper also provides velocity profiles measured at a distance of 105 cm from various orifice geometries, as shown in Figure 53. It is observed that the velocity in this region is slower compared to the velocity near the release point, indicating that the depressurization near the release point caused the rising of the velocity that reduced after the Mach disc.
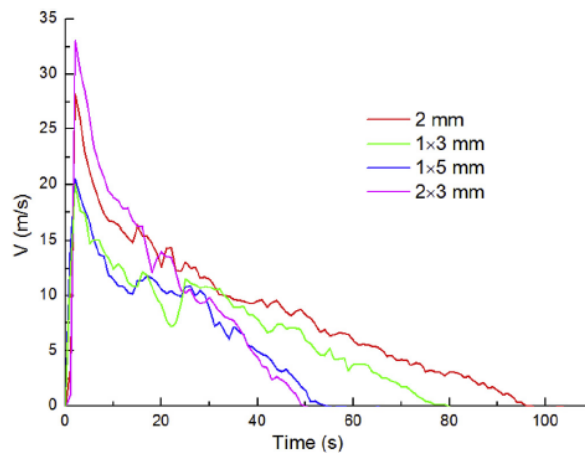
Figure 53: Many velocity profiles for different hole geometry measured at 105 cm from the release hole. (Teng L. et al., 2018)

Consequently, measurements of the mass flow rate of supercritical CO_2 release from different hole geometries and diameters are conducted, as shown in the figure below. To provide a clearer representation of the data, a zoomed-in view of the initial time instant was proposed in Figure 54.
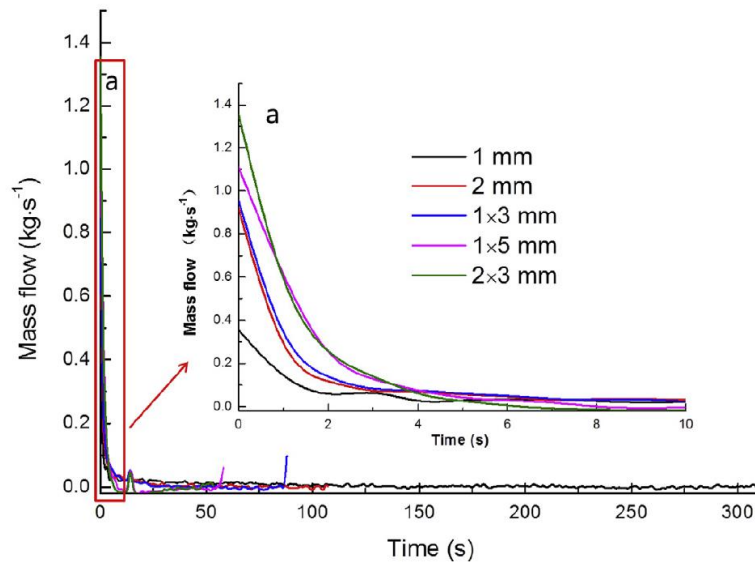
Figure 54: Mass flow rate for different hole geometries during the release. (Teng L. et al., 2018)

Even more important results for this thesis are the CO_2 concentrations in the vicinity of the leakage areas. Two types of measurements were presented in this context. Firstly, the measurement of CO_2 concentrations at a distance of 50 cm from the release point, and secondly, the measurement of the highest concentrations observed. In both cases, different diameters or geometries of the nozzle were considered to compare the results, and the measurements could be influenced by various phenomena. For instance, the depositions of dry ice on the ground and its subsequent re-suspension after a certain time may impact the measurements. Additionally, in the case of larger orifice geometries, the limited capacity of the vessel may result in a shorter duration of the maximum concentrations.
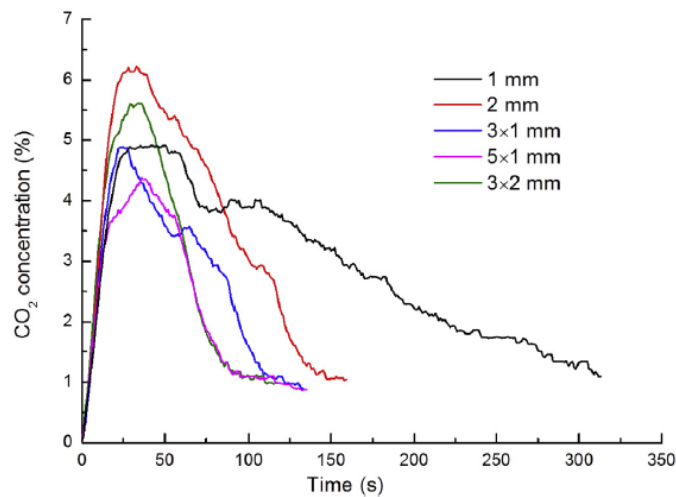
Figure 55: CO_2 concentrations measured at 50 cm from different hole geometries. (Teng L. et al., 2018)
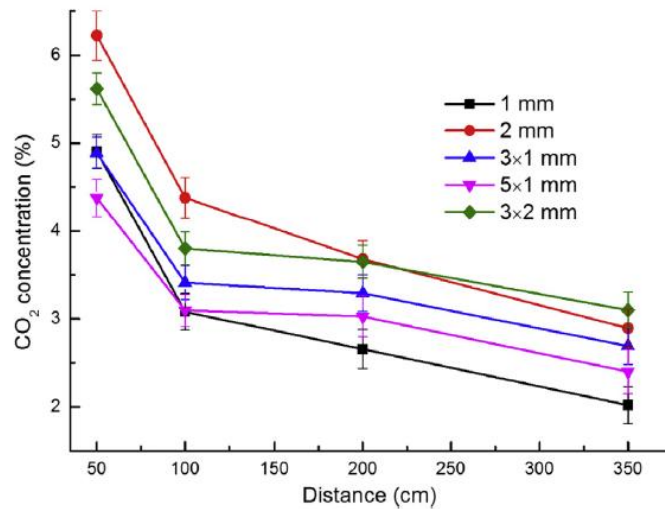
Figure 56: Maximum CO₂ concentrations for different hole geometries. (Teng L. et al., 2018)

One of the most relevant large-scale experiments was performed by (Guo et al., 2016) as a part of the CO₂QUEST project. The experiment utilized a 258 m long pipeline with three different release diameters respectively 15 mm, 50 mm, and Full-Bore Rupture (FBR). The pipeline had an internal diameter of 233 mm and a wall thickness of 20 mm. Initially, it was charged with CO_2 at 2.2 MPa and -10 °C, and then heated to reach the supercritical conditions needed for the experiments. To measure the discharge pressure inside the pipeline, two pressure transducers were installed at the end of the pipeline. In the discharged area, 18 thermocouples and 19 CO_2 concentration sensors were positioned at 1,3 m of height to measure temperature and CO_2 concentrations, respectively.
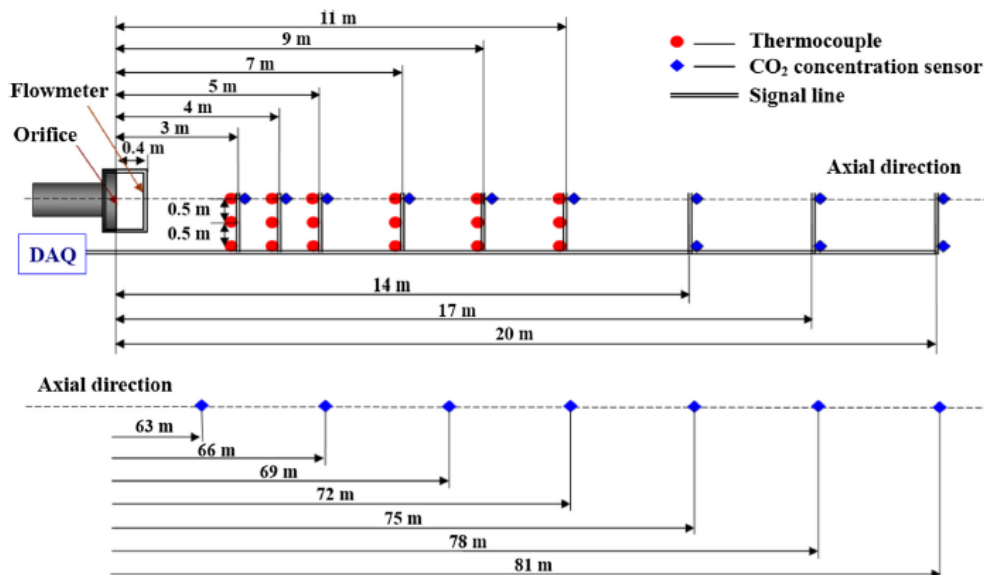
Figure 57: Experimental setup of the instrument involved in the experiment. (Guo et al., 2016)

The schematic representation of the instrument positions involved in this experiment is shown in Figure 57. The legend in the upper right part of the figure indicates that the red

points represent the thermocouples, and the blue rhombuses represent the CO_2 concentration sensors connected to the signal line to perform the data acquisition.

To analyze the various orifices, three separate tests were conducted. The experimental setup and the environmental conditions in which the experiment was carried out, were reported in Table 15 below. It is possible to note how the environmental conditions were different in each test. The first test was performed with a higher atmospheric instability and higher wind speed than the other two, and this condition will affect the result. As in the previous experiments described above, the release of supercritical CO_2 exhibited an under-expanded jet structure with the formation of the Mach disc in the near field.

Table 15: Environmental conditions and experimental setup of the three tests. (Guo et al., 2016)

Number	Test1	Test2	Test3
Pressure (MPa)	7.6	7.9	8.0
Temperature (°C)	35.1	33.4	36.9
Orifice (mm)	15	50	FBR
Inventory (tons)	3.14	6.27	3.59
Environmental pressure (kPa)	101.02	100.75	100.01
Environmental temperature (°C)	0.2–2.2	4.7	26.6
Humidity (%)	52.4–52.5	75.9	62.8
Wind speed (m/s)	5.5–7.2	1.5	0.8
Wind direction	290–348	188	198
Atmospheric stability	D	B	B

Figure 59, Figure 60, and Figure 61 presented below, corresponding to tests 1, 2, and 3, illustrate the pressure behavior throughout the entire release process. The time needed for the pipe to empty is strictly dependent on the diameter of the release hole (nozzle). For this reason, each test is characterized by different time durations, which become shorter when using larger diameters. Also, two differential pressures are considered where ΔP_1 represents the dynamic pressure along the axial direction near the release hole, while ΔP_2 represents the dynamic pressure also near the orifice but shifted 10 cm from the axial direction. For further details, refer to Figure 58. The measurements of dynamic pressure are necessary for the estimation of the type of jet involved during the release. For instance, by comparing the values of ΔP_1 and ΔP_2, it is possible to identify the transition from an under-expanded jet to a free turbulent jet when ΔP_1 results higher than ΔP_2.
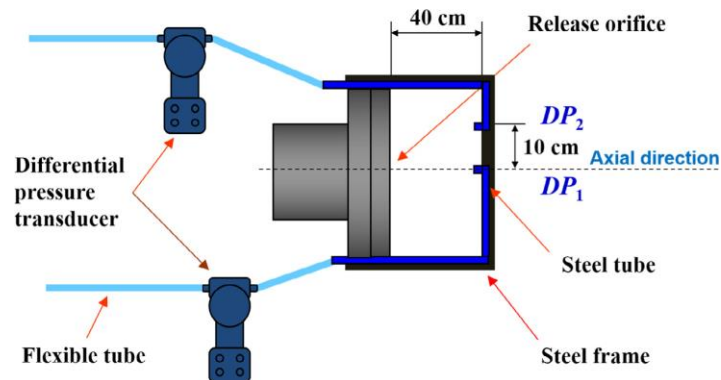
Figure 58: Dynamic pressure measurement setup. (Guo et al., 2016)
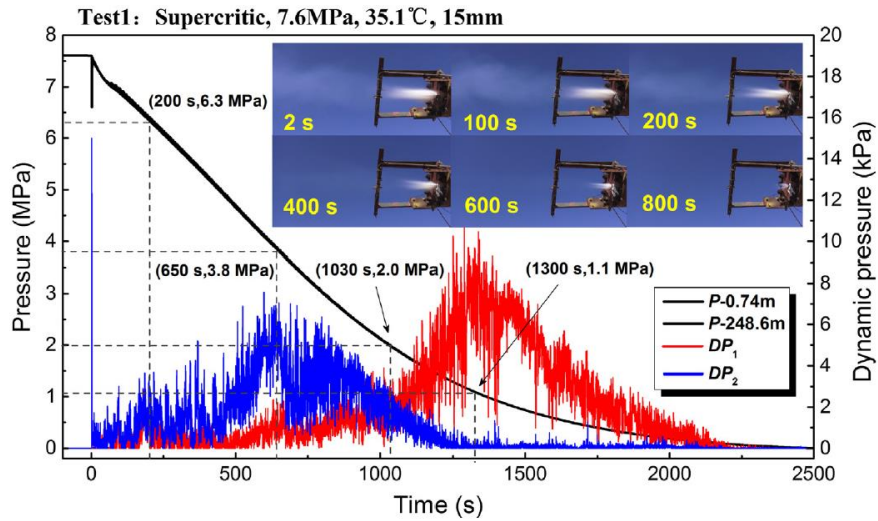
Figure 59: Pressure release and Dynamic pressure registered during test 1. (Guo et al., 2016)

The dynamic pressure was also involved in the estimation of the jet velocity in the near field that, as in the previous experiment in the upper part of this paragraph, it was calculated by the formulation:

$$V = \sqrt{2 * \frac{\Delta P}{\rho}} \tag{24}$$

However, instead of using an appropriate Equation of State to estimate the density of the supercritical CO_2, an average value was used, in particular, $\rho = 2.5745$ Kg/m^3.

As a consequence of the Joule-Tomson effect, the temperature dropped sharply. Consequently, it became possible to observe the formation of the dry ice particles, that make the jet white. This phenomenon was captured by a camera installed in the proximity of the release point. By examining the provided images, it is feasible to conduct a qualitative analysis of the jet's structure for tests 1, 2, and 3. However, due to the presence of ice particles, it is impossible to discern the formation of the Mach disc near the release region, thereby hindering the interpretation of the results.
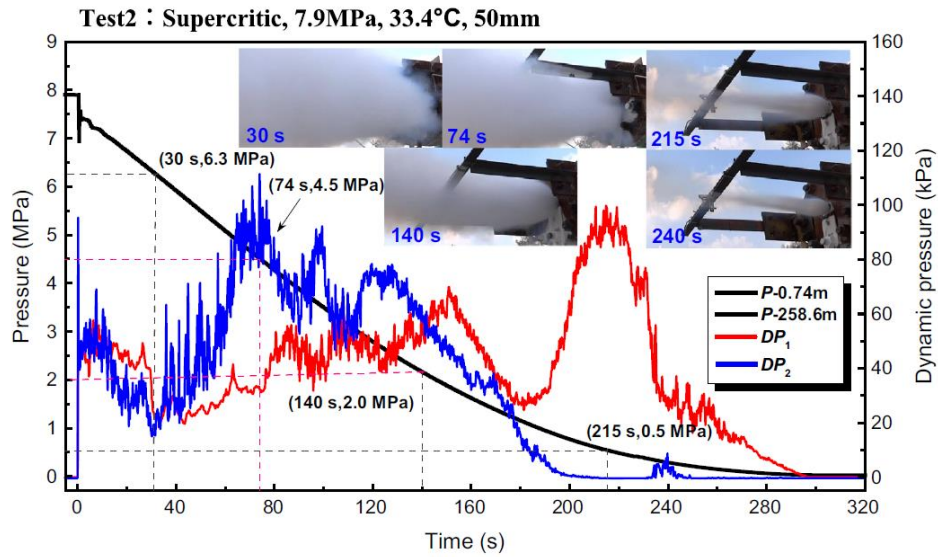
Figure 60: Pressure release and Dynamic pressure registered during test 2. (Guo et al., 2016)
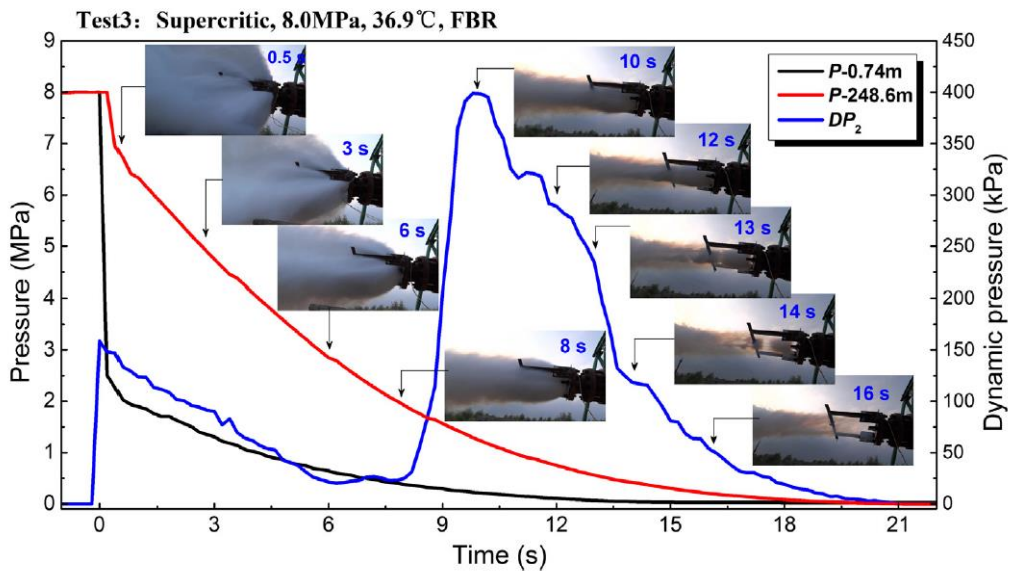
Figure 61: Pressure release and Dynamic pressure registered during test 3. (Guo et al., 2016)

The temperature distributions during the release for tests 1, 2, and 3 were measured using thermocouples installed along the axial direction. These temperature readings were then plotted in Figure 62. The observed temperature distribution follows the physical behavior of an under-expanded jet, as it exhibits the lowest temperature near the release point due to the generation of shock waves during the release process. For test 1, the temperature fluctuation can be attributed to unstable atmospheric conditions and the small diameter of the release hole. The temperature profiles are affected by the amount of CO_2 present in the pipeline and the density of the CO_2 used for the release. This influence becomes evident by examining the minimum temperature registered in test 2, which was significantly lower, around -47 °C, compared to the -3.2 °C recorded in test 1. In fact, in test 2, the mass of CO_2 filled in the pipe was almost double compared to the other two cases, resulting in a higher density, as indicated in the experimental setup table (Table

72

15). During test 3, the high power of the release caused the unavailability of the thermocouples installed at 3 and 4 meters from the release point. As a result, the data recorded from these thermocouples were not considered in the chart.
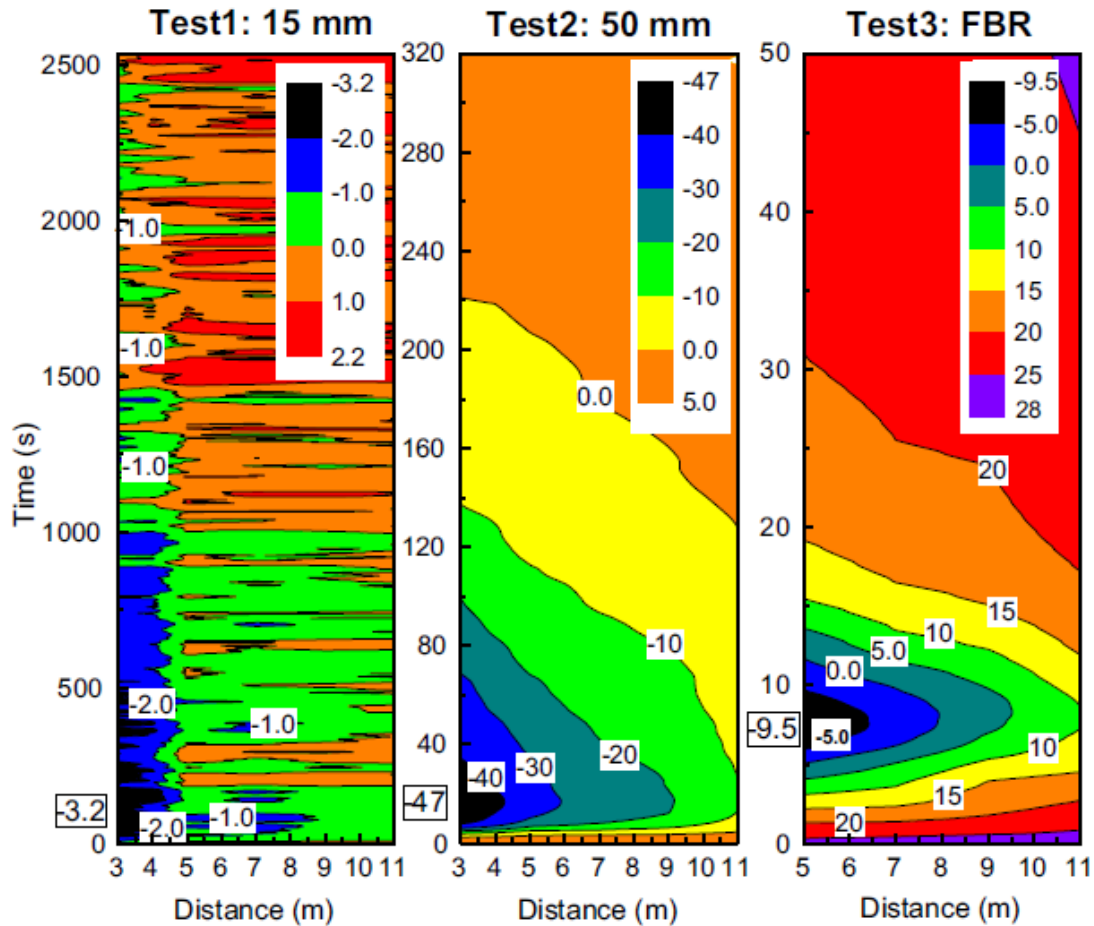
Figure 62: Temperature distribution along the axial direction during the release for tests 1, 2, and 3. (Guo et al., 2016)

Graphical representations of the temperature distributions along the axial and vertical directions for tests 1, 2, and 3 are shown in Figure 63. The y-axis represents the axial direction, while the x-axis represents the vertical direction. As shown in the experimental setup representation, thermocouples were installed not only along the axial direction after the release section but also, for each point, two additional thermocouples were positioned below this axis, respectively at 0.5 and 1 m from the axial axis in the direction of the terrain. However, this research paper does not indicate the specific time instance at which the temperature distributions in the discharge area were captured. Also, there aren't pieces of information regarding the positions of the Mack disc that appears during the release, making impossible a comparison with the analytic results provided by the equation proposed in the theory chapter. In addition, due to the considerable distance between the thermocouple locations and the position of the Mach disc, it is not feasible to visualize the structure of the Mach disc in the images. Consequently, temperature readings in the near field cannot be recorded. However, the temperature distributions shown in Figure 63 (which are not time-dependent) exhibit a similar order of magnitude to those presented in Figure 62.
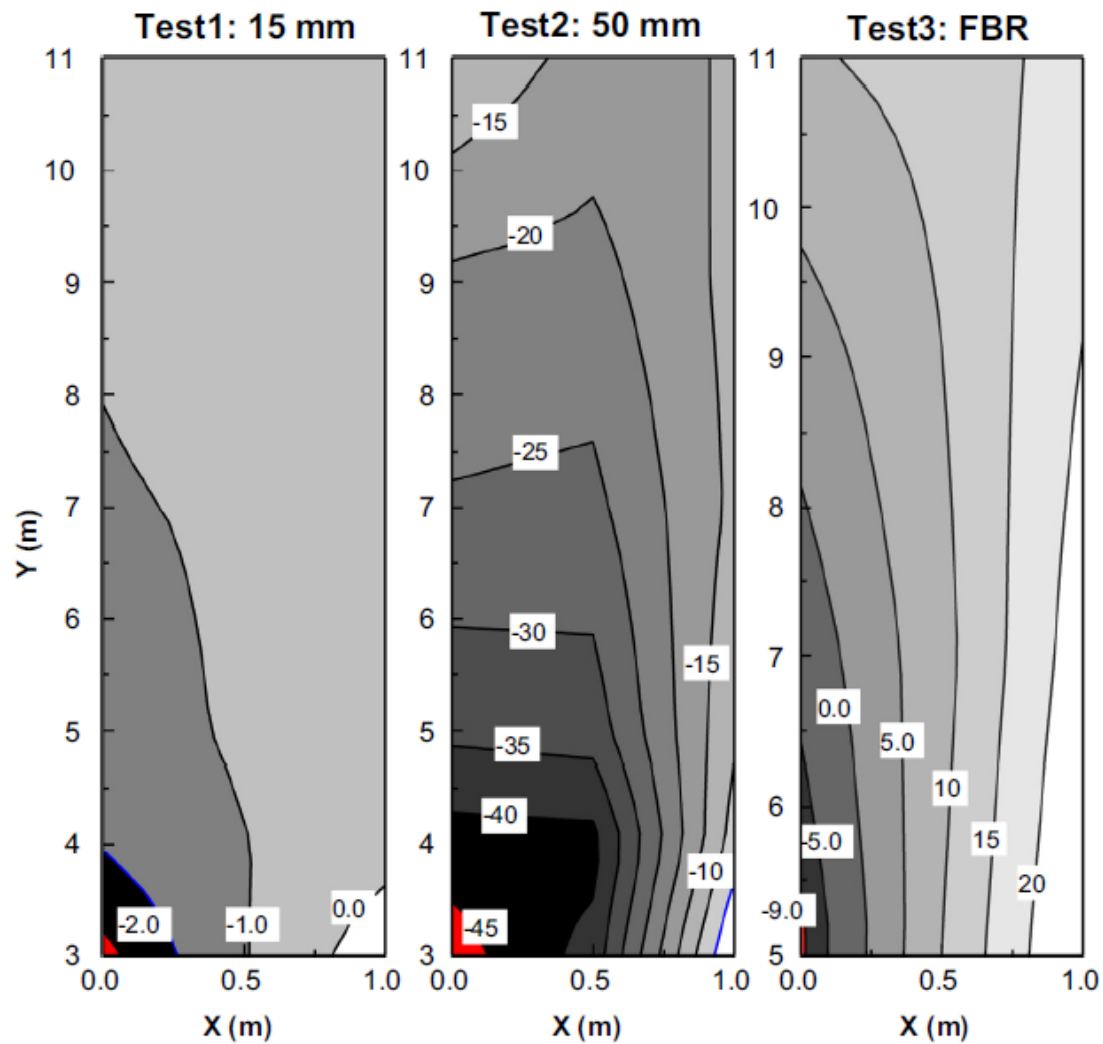
Figure 63: Temperature distribution along axial and vertical directions for tests 1, 2, and 3. (Guo et al., 2016)

The measurement of the CO_2 concentration along the axial direction was performed using CO_2 concentration sensors that were installed as indicated in the experimental setup diagram. As shown in Figure 64, during test 1, the CO_2 concentration along the axial direction remained below 3.2% throughout the entire release period. The distortion of the data of test 1 compared to the distributions observed in tests 2 and 3 can be attributed to the prevailing climatic conditions, which resulted in an underestimation of the concentration values. The high wind speed recorded during the experiment caused the CO_2 to disperse in the air. Indeed, in test 2, the CO_2 concentration was higher than in test 1, highlighting the influence of atmospheric conditions on the results of the previous test. The higher concentration registered in test 2 was explained by the larger release diameter and the bigger amount of CO_2 filled in the pipe before the experiment. The concentration of CO_2 was even higher during the third experiment, which involved the use of a full-bore diameter. From this final experiment, it was noted that the measurement of CO_2 concentration was affected by the dispersion of the dry ice particles of CO_2 on the terrain. This posed a challenge in accurately measuring the concentration of the CO_2 itself because, over time, the dry ice evaporates, leading to an increase in concentration in the area and thus affecting the measurements.
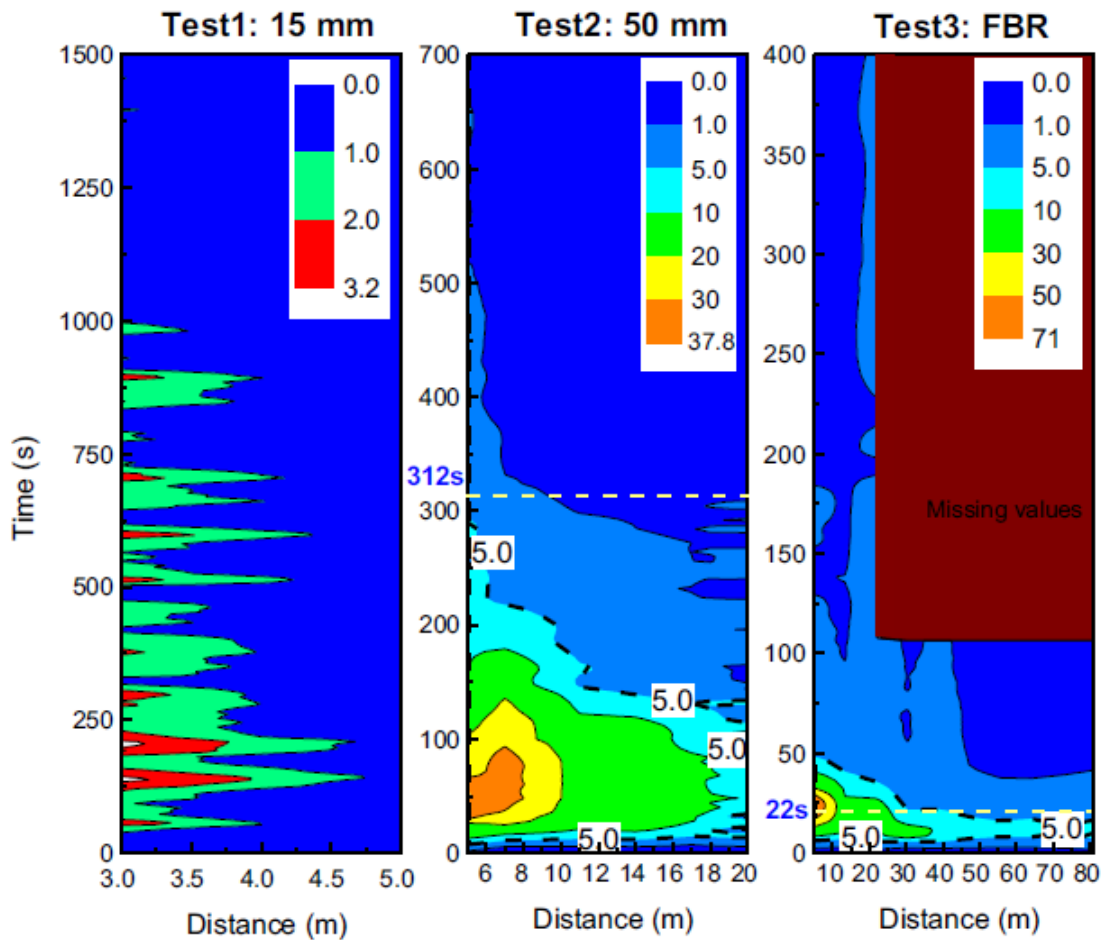
Figure 64: CO₂ concentrations measurements for tests 1, 2, and 3. (Guo et al., 2016)

For example, after 200 seconds, there was still a certain CO_2 concentration present at 20 meters from the release point, while at 10 meters away, the concentration had diminished. This indicates that the strong force of the release propelled the dry ice particles approximately 20 meters from the release point. To aid in the interpretation of this phenomenon, Figure 65 illustrates how the ground influenced the measurements of CO_2 concentration.
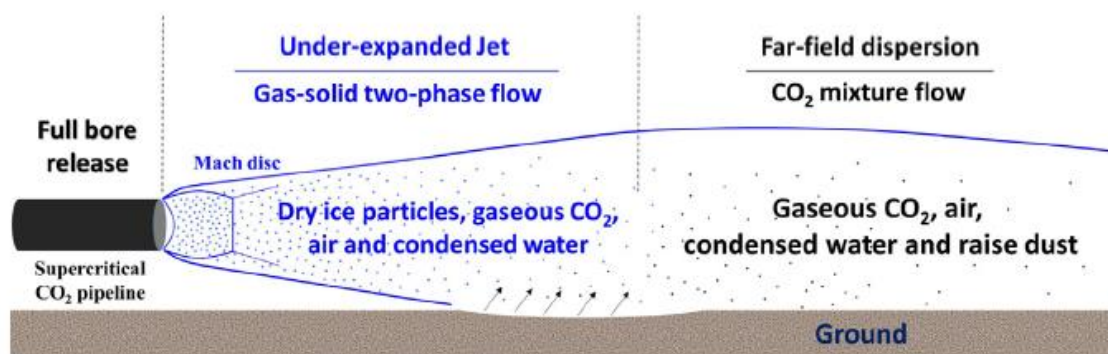
Figure 65: Simplification scheme for easy interpretation of the influence of the ground in a general supercritical CO₂ release. (Guo et al., 2016)

Also, the DNV provides a series of 12 tests regarding the release of supercritical CO_2 in different conditions. However, the data regarding these tests are not completely freely available. Table 16 reports only nine out of the total tests conducted in recent years. Since there is limited information available on these tests, additional details are provided by (Joshi Preeti, 2016). In this context, tests 8 and 8R (the repetition of the same test) are described below.

Table 16: Experimental conditions for many tests. (Witlox et al., 2012)

Input	Test1	Test2	Test3	Test5	Test6	Test11	Test8	Test8R	Test9	Input for models
Discharge data										
steady-state/transient	steady	steady	steady	steady	steady	steady	trans.	trans.	trans.	–
storage phase	liquid	liquid	liquid	liquid	liquid	liquid	vapour	vapour	vapour	DISC, TVDI
storage pressure (barg)	103.4	155.5	133.5	157.68	156.7	82.03	157.76	148.7	154.16	DISC, TVDI
storage temperature (C)	5	7.84	11.02	9.12	9.48	17.44	147.12	149.37	69.17	DISC, TVDI
vessel volume (m^3)	–	–	–	–	–	–	6.3	6.3	6.3	TVDI
orifice diameter (mm)	11.94	11.94	11.94	25.62	6.46	11.94	11.94	11.94	11.94	DISC, TVDI
release duration (s)	60	59	60	40	120	58	120	132	179	–
Ambient data										
ambient temperature (C)	14.2	7.5	10.6	5.8	6.1	11.6	11.19	11.1	8.2	DISC, TVDI, UDM
ambient pressure (mbara)	999.4	958.2	972.5	985.4	938.4	960.2	957.99	957.1	958.9	DISC, TVDI, UDM
relative humidity (%)	74.4	96	95.8	96.7	1	94	100	100	99.9	DISC, TVDI, UDM
wind direction (degrees)	322.4	265.6	288.8	278.6	299	270.8	269.3	270	270.7	UDM uses 270°
wind speed (m/s)	4	3.44	3.37	5.13	2.20	5.99	4.71	0.76	4.04	UDM
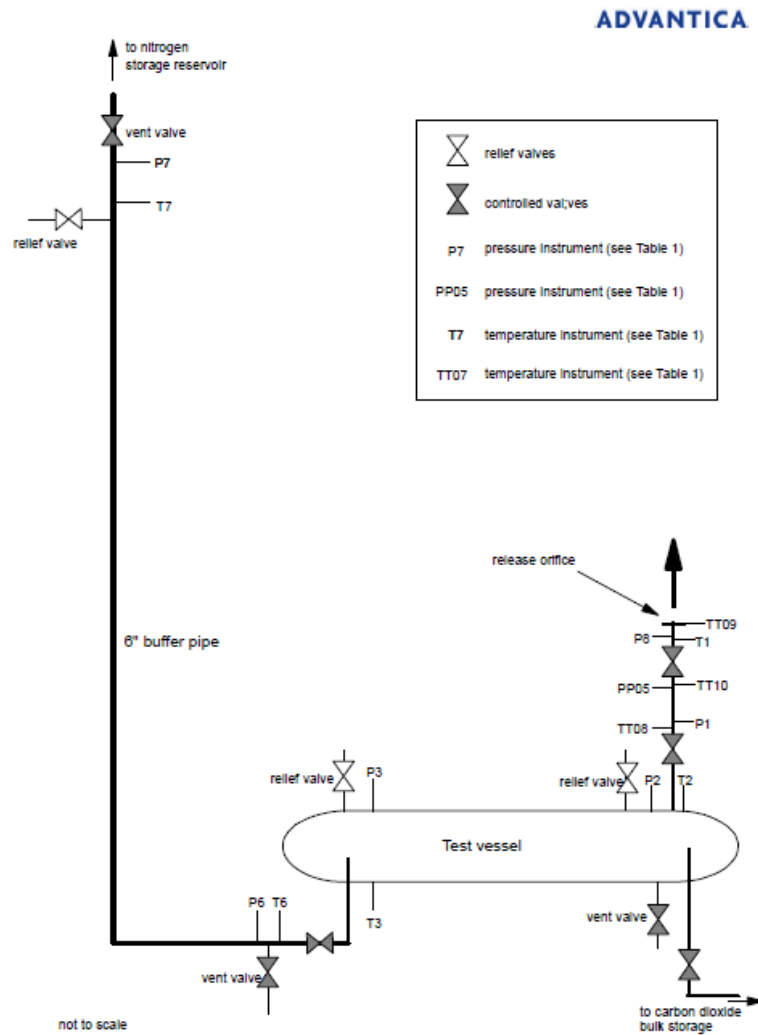
Figure 66: Experimental setup of the tests. (Joshi Preeti, 201In

The experimental setup, which is proposed in Figure 66, consisted of a 100 m x 100 m platform where a vessel with a length of 24 m and a diameter of 0.6096 m (that corresponds to 24") was positioned above. The vessel has a volume of 6.3 m^3 and was completely insulated to achieve the desired temperature. The CO_2 was heated to reach the desired temperature before the experiment.

Two flexible pipes were connected to opposite ends of the release vessel. One pipe was attached to the release nozzle, while the other was connected to the 6" buffer line. The buffer pipe contains nitrogen and served the purpose of expelling the fluid from the vessel to simulate a constant steady-state release. The nitrogen was maintained at the same pressure as the CO_2 inside the vessel and was injected from the opposite end to facilitate the release of CO_2. However, in experiments 8 and 8R, which involve transient releases, the pressure was used as the driving factor for CO_2 release, and the buffer pipe was not used in these cases.

According to the table, the diameter of the release nozzle was 11.94 mm, and it was placed at 1.1 m from the ground. Figure 67 shows the instrument layout used to measure pressure, temperature, and concentration of the release along the release axis at different distances and angles.
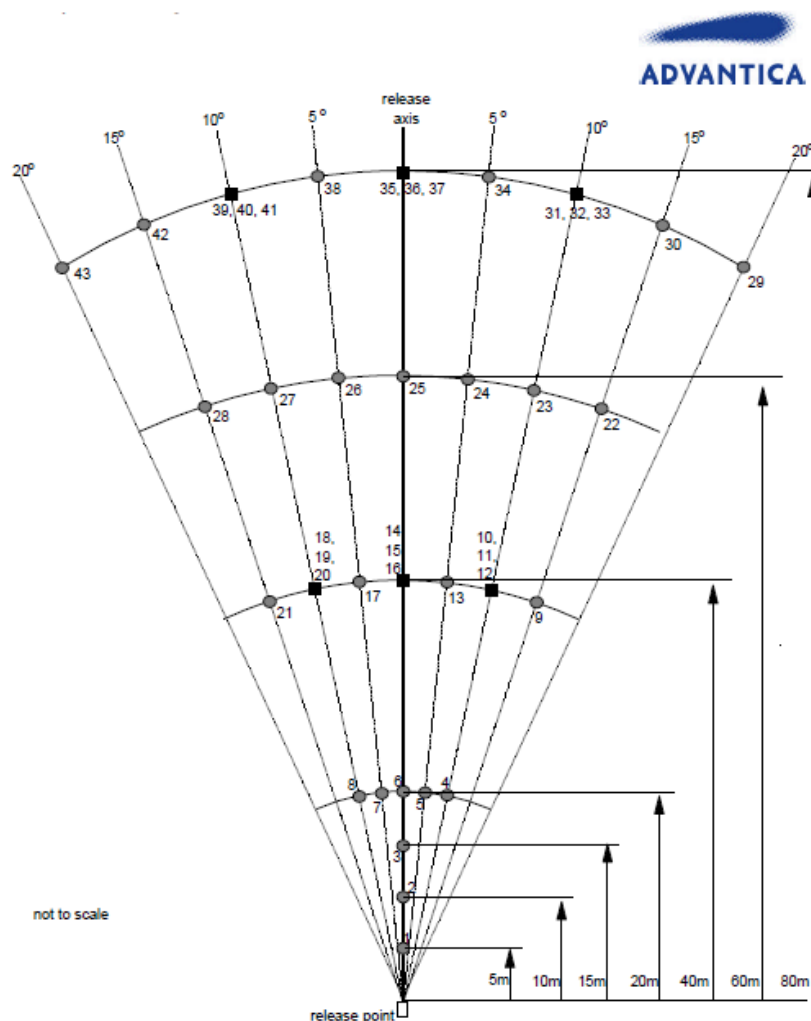
Figure 67: Instruments positions at different angles and distances from the release point. (Joshi Preeti, 2016)

A measurement of the wind speed was provided at 3.25 m, 5.05 m, and 8.55 m from the ground, as well as at a distance of 17.2 m from the release point. To summarize the detail of test 8, Table 17 was proposed:

Table 17: Test 8 conditions. (Joshi Preeti, 2016)

Parameter	Value/ Configuration
Release orientation	Horizontal
Release orifice diameter	1/2" (11.94 mm)
CO_2 pressure in the vessel at the beginning of the experiment	157.4 bar
CO_2 temperature in the vessel at the beginning of the experiment	148.1 °C
Wind speed at heights 8.55m, 5.05m, 3.25m respectively	5.5 m/s, 5.2 m/s, 4.9 m/s
Atmospheric pressure	0.96 bar
Atmospheric temperature	7.8 °C
Solid drop out	None
Release time duration	121 sec

The data collected during the release of various tests, as well as the data available from the literature, are presented in

Table 18. This table includes the acronyms DISC (Phast steady-state discharge model) and TVDI (Phast time-varying discharge model), which are two empirical numerical models used respectively in steady-state conditions and in time-varying conditions. This table was concerned to validate these empirical models by comparison with the experimental data. However, only the mass flow rate results are available.

Table 18: Observed and Predicted results for many tests. (Witlox et al., 2012)

	Test1	Test 2	Test3	Test 5	Test6	Test 11	Test 8	Test 8R	Test 9
Discharge rate									
DISC initial discharge rate (kg/s)	8.84	10.98	9.988	50.75	3.21	7.03	4.19	3.90	6.86
DISC/TVDI discharge rate (kg/s) (averaged over first 20 seconds for tests 8,8R,9)	8.84	10.98	9.988	50.75	3.21	7.03	4.01	3.73	6.25
Observed discharge rate (kg/s) (averaged over first 20 seconds for tests 8,8R,9)	–	11.41	9.972	41.17	3.50	7.12	4.07	3.80	6.05
Deviation predicted from observed	7.8%	−3.9%	0.16%	+23%	−8.2%	−1.1%	−1.5%	−1.8%	+3.4%
Final (Post Expanded) State (UDM input)									
Discharge rate (kg/s) (from experiments)	8.2	11.41	9.988	41.17	3.50	7.12	4.07	3.80	6.05
Temperature (K) (DISC output)	194.6	194.1	194.26	194.4	193.8	194.1	198.2	204.8	194.1
Solid fraction (-) (DISC output)	0.397	0.403	0.384	0.399	0.397	0.330	0	0	0.154
Velocity (m/s) (DISC output)	156.7	189.8	179.2	191.7	191.3	154.2	466.5	472.8	289.0
'Droplet' Diameter (μm) (DISC OUTPUT)	9.35	6.53	7.29	6.16	6.54	10.0	0	0	2.82

In particular, the behavior of the mass flow rate and its prediction with the TVDI model is represented in the figure below. The red line represents test 8, while the purple one represents the repeated test 8R.
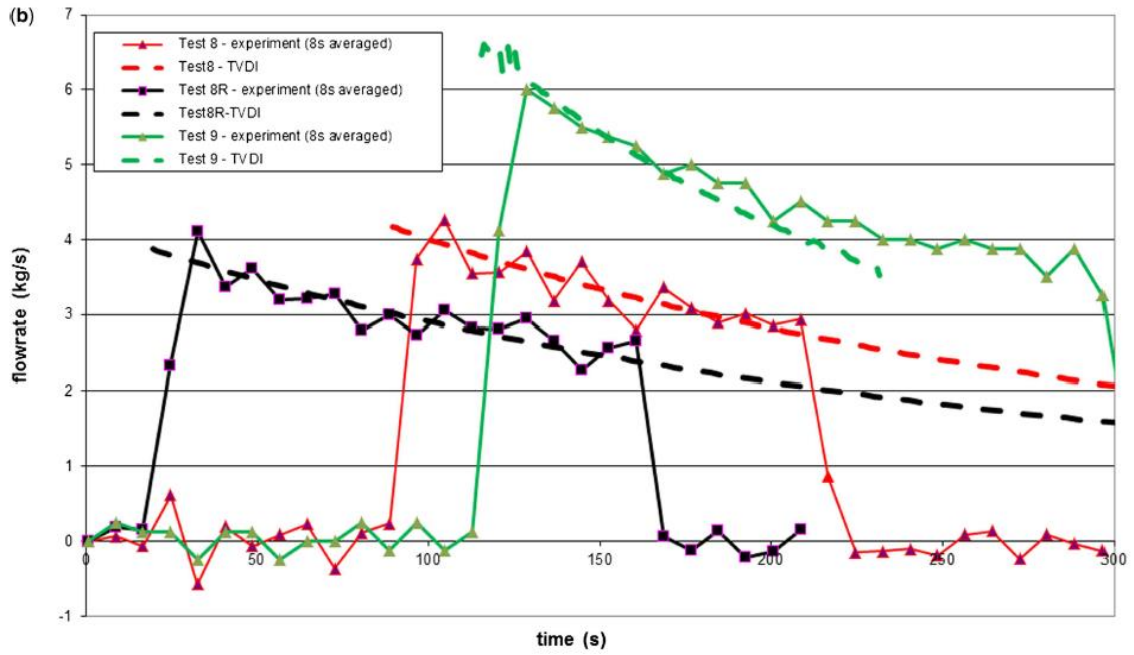
Figure 68: Experimental and predicted mass flow rate. (Witlox et al., 2012)

In addition, (Joshi Preeti, 2016) provides a comparison between the numerical results and the experimental data for the concentration of CO_2. These results were just discussed in the paragraph that provides an overview of the numerical model. For more detailed information, refer to Figure 31.

5   CFD modeling and results

The literature review about the numerical modeling of supercritical CO_2 releases highlighted that the available information and the methodology for conducting CFD simulations of this phenomenon are incomplete. Due to this existing literature gap, the objective of this thesis work is to investigate strategies for the numerical modeling of supercritical CO_2 releases from high-pressure components for QRA purposes through a series of tests. Moreover, understanding how to model this phenomenon can significantly support the implementation of supercritical CO_2 in the SBAM model.

The literature review on numerical modeling serves as a guide for setting up the CFD simulations, while the review of experimental research is utilized to compare experimental data with simulation results, ensuring that the simulation setup is appropriate for the scope of this thesis.

This chapter utilizes technical terminology associated with the ANSYS Fluent software to describe the proposed CFD simulations. In general, the simulations presented are divided into two parts. The first part describes the system's geometry, mesh, and boundary conditions, while the second part analyzes the results obtained from the simulation. To ensure clarity, these parts are respectively referred to as "Configuration Setup" and "Results". Additionally, a range of possibilities to implement a Real gas model is described to highlight the advantages and disadvantages of their applicability.

5.1 Preliminary Simulation

At first, a numerical simulation employing the ideal gas equation of state (EOS) is presented. The simulation was carried out using ANSYS Fluent software and aims to replicate a specific case study described in an experimental review, to compare the numerical model results with the experimental data provided by (Teng L. et al., 2021).

Configuration setup

In the scientific papers, the measurement instrument was positioned in a specific way. To ensure consistency, the numerical model was also configured to register data at the same positions and using the same tags. Therefore,

Table 19 provides a summary of the distances from the orifice where the measurements are conducted. Moreover, the measurement points considered for the numerical model are within the first 105 cm from the release point, resulting in reduced computational effort compared to including all the measurement points considered in the experiment.

All measurements are taken along the centerline, in front of the orifice, where the under-expanded jet release of supercritical CO_2 occurs.

Table 19: Representation of the positions of the measurements from the release point for both the numerical model and the experiment.

measure	tag	distance from the orifice	units of measurement
temperature	t3	3	cm
temperature	t4	6	cm
temperature	t5	11	cm
temperature	t6	19	cm
temperature	t7	29	cm
temperature	t8	49	cm
CO_2 concentration	c1	50	cm
temperature	t9	69	cm
temperature	t10	99	cm
CO_2 concentration	c2	100	cm
velocity	v	105	cm

In this case, as shown in Figure 69, a 3D geometry was proposed and consisted of a convergent-divergent nozzle with a 2 mm release diameter, and an ambient region extended approximately 105 cm from the orifice.
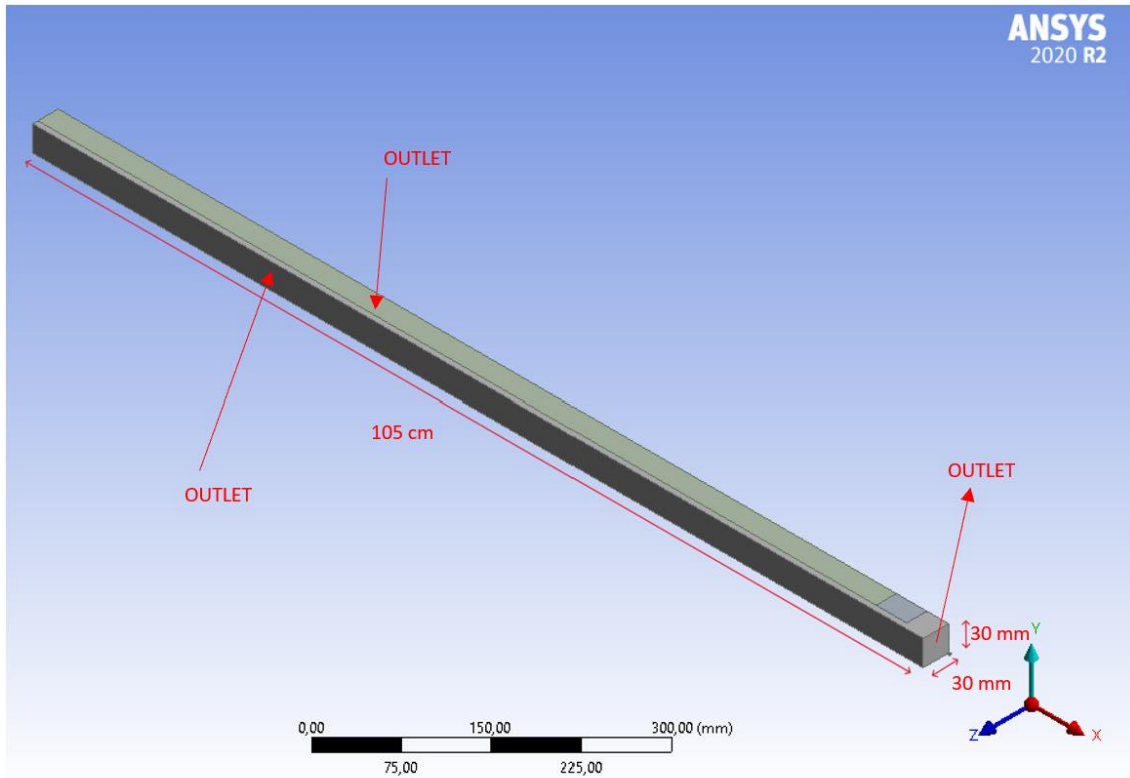
Figure 69: "Isometric view" of the computational domain.

The computational domain of the nozzle and the ambient is a quarter of the total domain, allowing for a reduction in computational effort by exploiting symmetries. Figure 69 proposed the "isometric view" of the computational domain, highlighting the dimensions of the ambient region. Specifically, the ambient region, where the release occurs, spans a length of 105 cm from the nozzle outlet and extends laterally 30 mm relative to the nozzle. All faces associated with the ambient region are assigned a *Pressure Outlet Boundary Condition,* except for the faces related to the symmetry, which are set to an *Axis Boundary Condition* to be able to set an *axisymmetric* simulation. These symmetry faces correspond to the sides where the domain is cut, specifically the y-x plan and the z-x plan. It is important to note that there is always a reference axis present in the lower part of the figures, aiding in understanding the orientation of the displayed domain.

However, due to the large length of the ambient region aimed at capturing the results of the parameters during the simulation, the nozzle is not adequately visualized. Therefore, a zoomed-in view of the nozzle is proposed in Figure 70. In this picture, it is possible to observe the shape of the nozzle, which features an inlet radius of 2 mm, which is double in comparison to the size of the outlet radius which is 1 mm. This design ensures a choked condition in the nozzle and a *Pressure Inlet Boundary Condition* is set on the inlet face. Moreover, thanks to the "isometric view", it is possible to appreciate the face related to the *Wall Boundary Condition,* which plays an important role in the stability of the simulation.
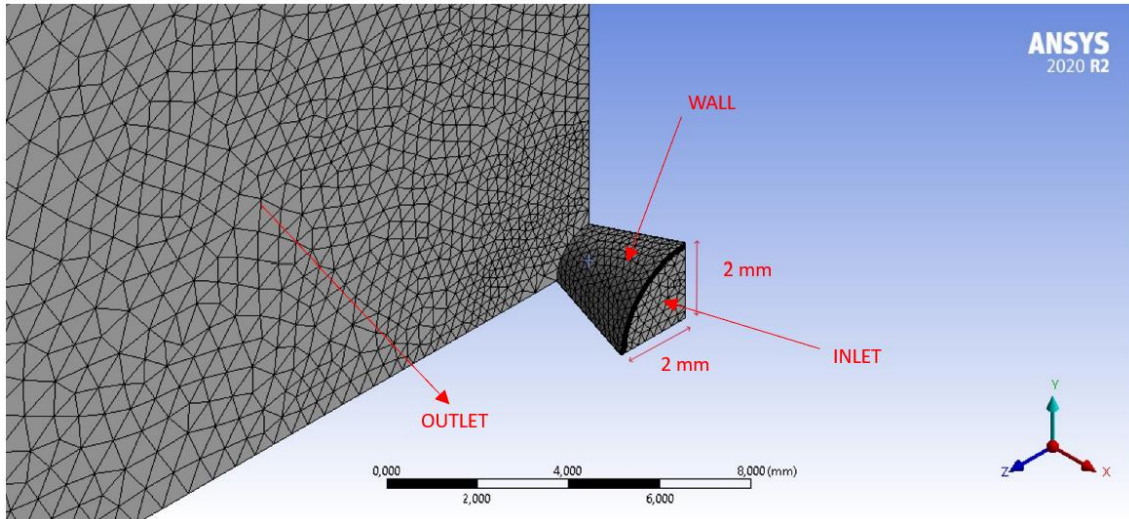
Figure 70: Zoomed-in "isometric view" of the release nozzle.

A "lateral view" is proposed for the pictures below because it better illustrates the system's geometry. In this context, the "lateral view" refers to the x-y plan, which, as previously mentioned, represents the symmetry side. However, Figure 71, referring to the x-y plan, lacks sufficient details, necessitating a zoomed-in view of the nozzle.
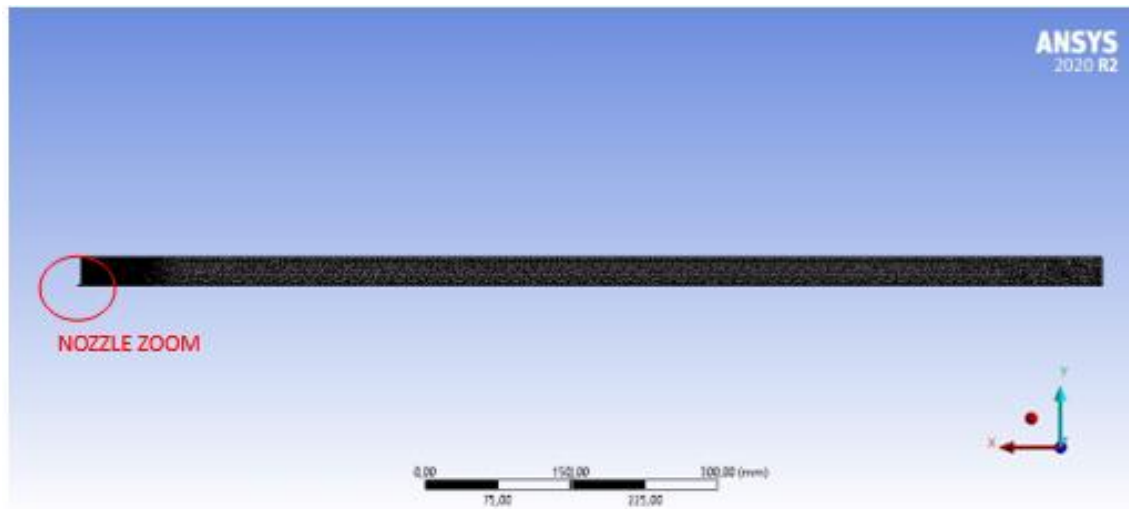
Figure 71: "Lateral view" of the computational domain.

Figure 72 shows a zoomed-in view of the nozzle, and thanks to the "later view", it allows for a clear understanding of the nozzle length, which is designed at 3 mm. Moreover, it provides better visualization of the inlet (on the left side) and the outlet of the nozzle. As previously described in Figure 70, the inlet has a radius of 2mm, while the outlet has a radius of 1 mm.
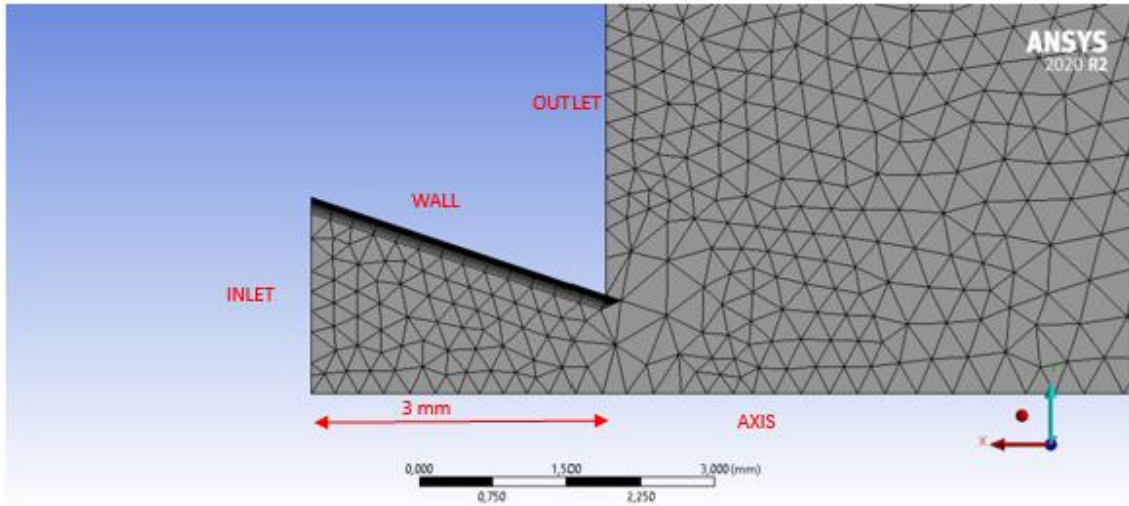
Figure 72: Zoomed-in "lateral view" of the release nozzle.

After the description of the computational geometry, it is necessary to explain the methods used to create the mash. The mesh of the 3D domain consists of nearly a million elements, employing a *growth rate* of 1.05. The following settings were used to realize the mesh:

- A general *growth rate* of 1.05 is applied in the mesh settings to minimize the difference between smaller elements near the release zone and larger elements in the farthest area at the release point.
- A *sphere of influence* is used for the nozzle region with an element size of 0.25 mm. This setting is visible in Figure 73.
- A *sphere of influence* is used for the near-release region (only for the first 20 mm) with an element's size of 0.4 mm. This setting is visible in Figure 73.
- A *body of influence* is implemented with an element's size of 1.5 mm as soon as after the second *sphere of influence*.
- A *body of influence* is implemented in the end part of the domain to control the last elements to not exceed the size of 3 mm.
- An *inflation layer* is applied to the wall, with a first layer height of 0.001 mm and a maximum layer number of 19. The growth rate for the inflation layer is set to 1.2. The mesh near the wall boundary condition, modeled by the inflation layer setting, can be observed in Figure 72. The *inflation layer* is necessary at the wall to ensure stability during the simulation, as the turbulent fluid dynamics equations rely on the parameter "Y+" to describe the flow state near the solid surface.
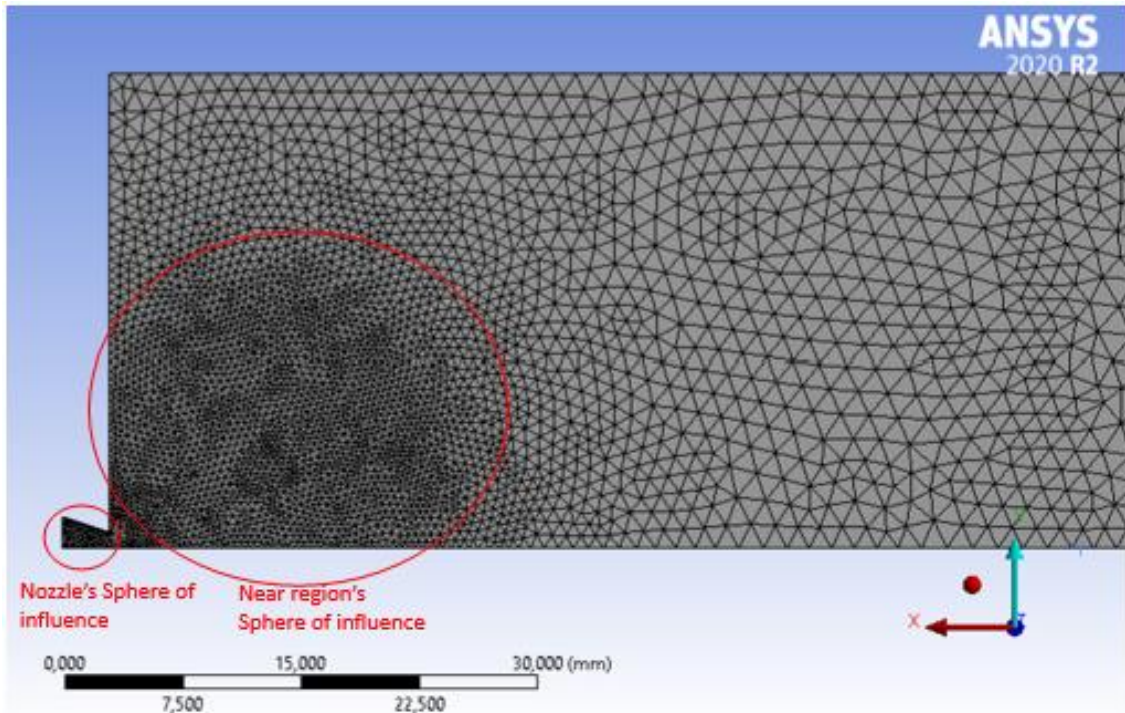
Figure 73: Zoomed-in "lateral view" with positions of the spheres of influence.

At the end of the configuration setup, it is necessary to provide a summary of the boundary conditions that were mentioned during the explanation of the geometric setup:

- *The Pressure Inlet Boundary Condition* is selected based on the available data obtained from the experiment conducted by (Teng L. et al., 2021). Specifically, in this case, the pressure value is variable in time, and it is represented in the graph shown in Figure 50. Using software capable of extracting data from graphs, the pressure data and their corresponding time steps were stored in a table, which was then utilized as a "transient table" in the ANSYS Fluent software. At the beginning of the simulation (t = 0 s) the pressure value is set to 80 bar, gradually decreasing over a transient period lasting approximately 91.6 seconds. Additionally, a temperature of 330 K was assigned to this boundary condition, with the specification that the molar fraction consists entirely of CO_2.
- *The Pressure Outlet Boundary Conditions* on the ambient faces are kept at their default settings.
- *The Axis Boundary Conditions* on the cutting domain, which enable the reduction of the computational effort, are maintained at their default settings.
- *The Wall Boundary Condition* on the nozzle wall is also kept at its default settings, which include a Stationary wall with No Slip condition and a roughness constant of 0.5.

Finally, a transient pressure-based simulation is carried out, considering the influence of gravity along the y-axis. The SST k-omega model is used to solve turbulence, considering both viscous heating and compressibility effects. For the selection of the material, a mixture of CO_2 and air from the ANSYS Fluent database is selected. The Ideal Gas low

is used as EOS for the estimation of the density. Moreover, a coupled scheme for the Pressure-Velocity Coupling is employed, using the First Order Upwind method for the discretization. Although this method is less accurate, it offers more stability for the convergence of the solution. The High Order Term Relaxation is employed to ensure stability to the simulation that was carried out with a high time step of 0.1 seconds.

Results

The results provided by the CFD simulation carried out on ANSYS Fluent are compared with the data collected by (Teng L. et al., 2021). The experimental data, as mentioned in the setup of the pressure boundary condition, is extracted using software capable of extracting data from graphs due to the absence of just tabulated data. Although this method is not highly accurate, it is sufficient for a qualitative analysis of the results. Comparative graphs containing "numerical model result" and "experiment data" are presented below for easy comparison. The discussion of the obtained results follows the same scheme as the related experimental review part for the sake of consistency.

The Pressure-Temperature graphs shown in Figure 74 represent the first qualitative comparison between the numerical results and the data collected during the experiments. It is important to underline that the simulation was carried out for the case that involve the use of a nozzle with a release diameter of 2 mm. However, the curve in the left graph presents a qualitative behavior closer to the curve concerning the release during the experiment involving a nozzle with a diameter of 1 mm (continuous line in the right graph legend). Regarding the minimum temperature recorded, both the numerical model result and experiment for the release with a nozzle diameter of 2 mm show approximately the same value, respectively -31°C and -30 °C. However, these two minima were registered in two different time instants. For instance, the minimum regarding the numerical model occurs when the pressure at the inlet is still approximately 2 MPa, while during the experiment, the minimum is registered when the pressure inside the tank is approximately 0 MPa. The minimum points are highlighted in Figure 74 with a red circle.
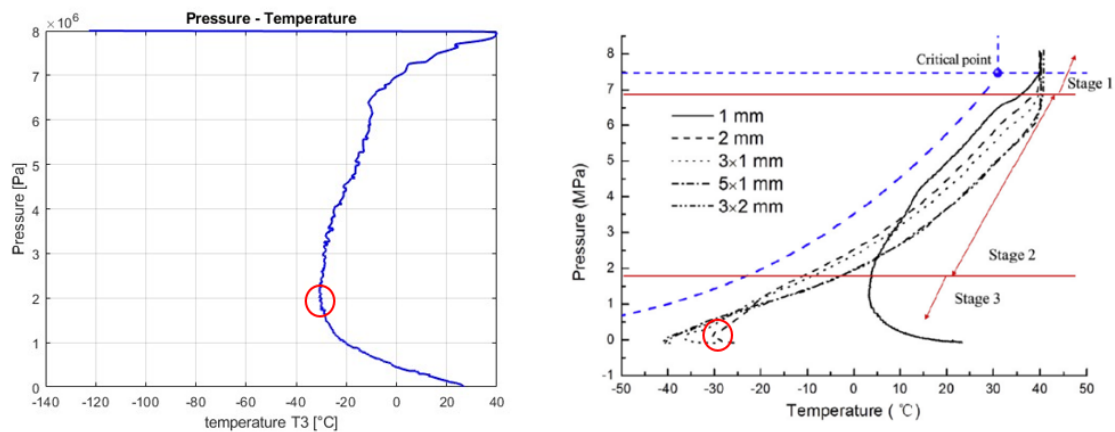
Figure 74: Pressure-Temperature graphs: Numerical modeling results on the left, experimental data on the right.

Another qualitative comparison can be made for the Temperature distribution along the center line of the release, considering the behavior presented earlier. However, it is important to remember that the numerical model results are based on a release that uses a nozzle of 2 mm, while the graphs from the experiment presented below pertain to the

release that uses a nozzle diameter of 1 mm. Therefore, only a qualitative comparison is possible.
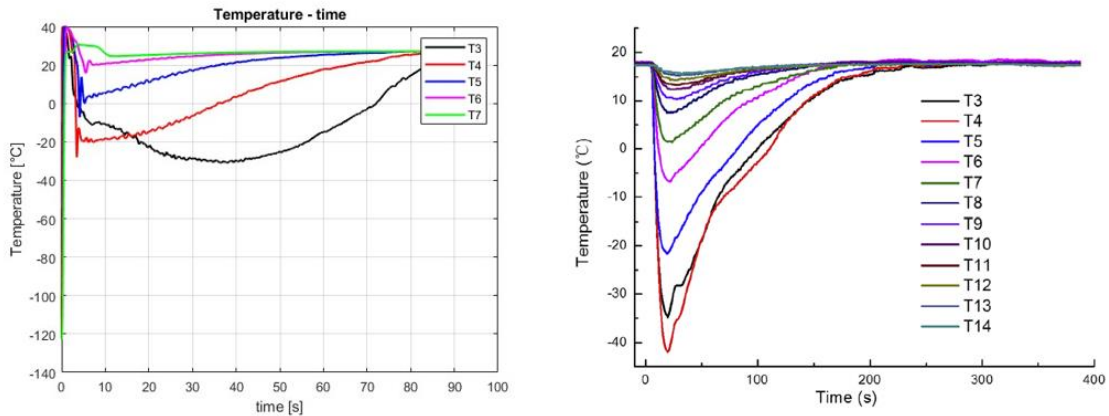
Figure 75: Transient temperature graphs: Numerical modeling results on the left, experimental data on the right.

For the numerical model results only the temperatures T3, T4, T5, T6, and T7 are considered due to the limited computational domain, and their positions are described in

Table 19. As mentioned above, the tags and distances of the measurement points are the same for both numerical modeling and experimental data to facilitate comparison. The behaviors of the curves in Figure 75 are qualitatively similar in both cases, except for the T3 curve in the numerical result, which not only exhibits a completely different trend but also a delayed minimum compared to the corresponding experimental curve.

A comparison of the velocity profile during the release is proposed in Figure 76, where the data from the experiment are also included for easy comparison. The original data was previously reported in the experimental review chapter in Figure 53. The numerical model velocity profile not only shows a higher maximum compared to the experiment but also a delay in its recording over time. Specifically, the maximum velocity registered in the numerical model is approximately 41.8 m/s, recorded 37.4 seconds after the beginning of the release phenomena. In contrast, the maximum velocity registered during the experiment is 28 m/s, observed 2.5 seconds after the beginning of the experiment. As indicated in the experimental setup table, these velocity profiles are measured at 105 cm from the release orifice. Two practical reasons can explain these deviations in the results. Firstly, regarding the maximum values, the accurate estimation of the CO_2 density plays an important role. In the numerical model, the density is estimated using the ideal gas low, which leads to underestimated values. As a result, the gas results lighter, in this case, tends to accelerate after passing through a convergent-divergent nozzle. Conversely, in the experiment, CO_2, being heavier, exhibits lower velocity profiles. Regarding the delay in the appearance of the maximum velocity, it could be attributed to the time step (dt) imposed in the simulation, which fails to adequately capture the early moments away from the inlet boundary condition. However, imposing a smaller time step in the simulation would significantly increase the computational effort, making simulation times unacceptable. It is worth noting that a convergence analysis for the time step can

accurately estimate the correct time step to be imposed on the simulation. Further analysis regarding the time steps is conducted in the numerical model using the Real gas EOS later in this chapter.
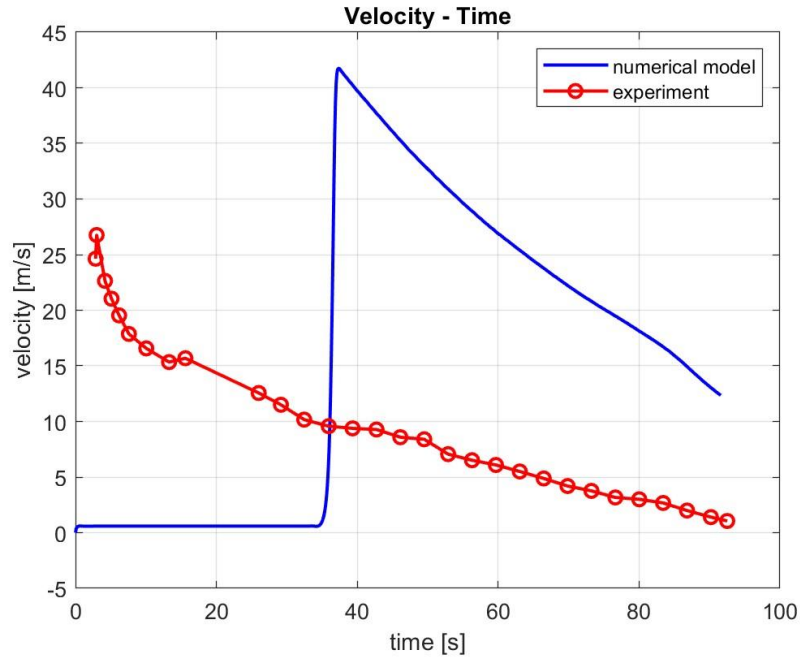
Figure 76: Transient velocity comparative graph.

A similar comparative graph is presented for the CO_2 concentration recorded at a distance of 50 cm from the release nozzle, as shown in Figure 77. Once again, differences in the maximum values are observed. However, it is noteworthy that the curve exhibits a different delay compared to the previous case. This delay occurs before reaching the maximum value, and once again, the cause of this delay can be attributed to the time step (dt) involved in the simulation.
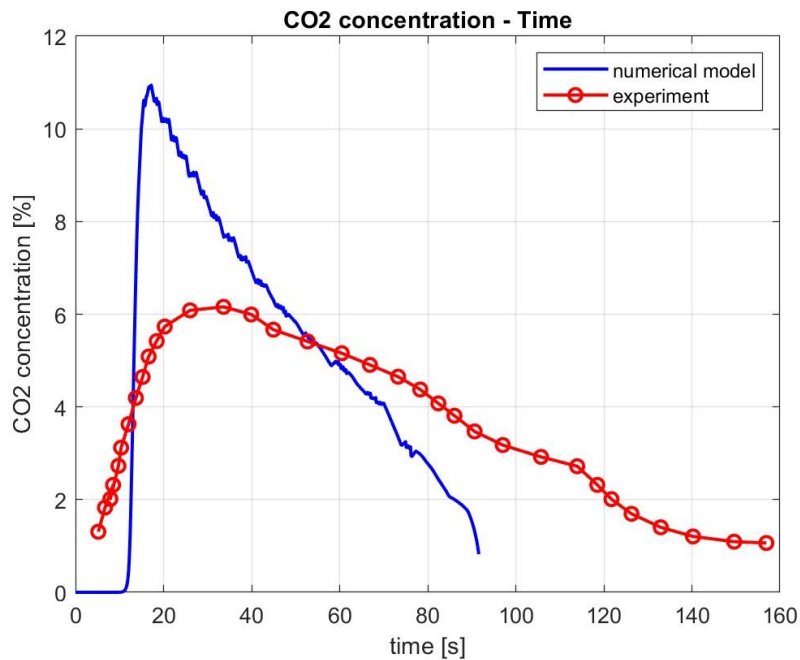
Figure 77: Transient CO₂ concentration comparative graph.

Another important difference is observed in the maximum values between the numerical model and the experimental data. In the numerical model, the maximum concentration reaches approximately 10.9 % at 17.2 seconds, while during the experiment, a maximum of approximately 6.2 % at 33.2 seconds was registered. Moreover, the decrease of CO_2 concentration towards zero is more rapid in the numerical model compared to the experiment, where it reduces gradually, highlighting the lighter nature of CO_2 due to the ideal gas EOS used in the numerical model.

Due to a significant difference of an order of magnitude between the experimental case and the results of numerical modeling, it is not feasible to generate a similar comparative graph for the mass flow rate exiting from the nozzle. Therefore, a direct comparison between the numerical model results and the recorded mass flow rate during the experiment is presented in Figure 78.
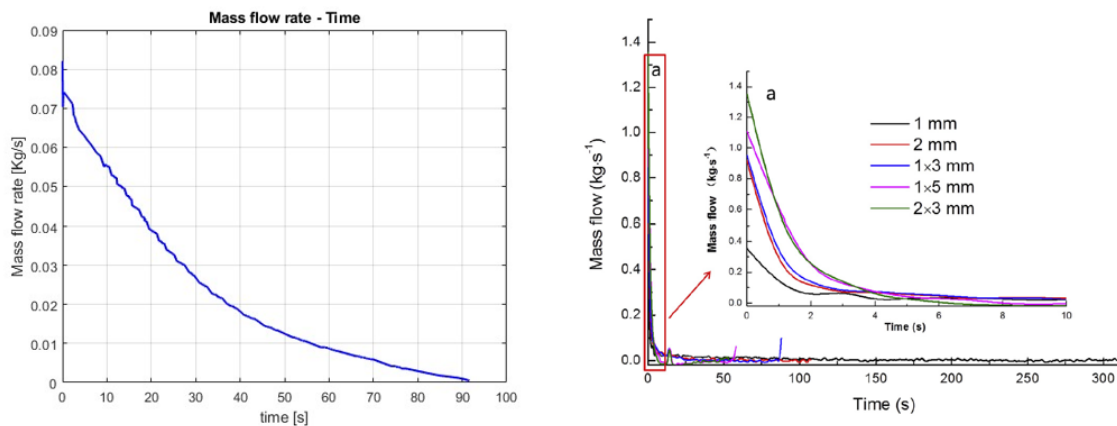
Figure 78: Transient mass flow rate graphs: Numerical modeling results on the left, experimental data on the right.

Upon initial examination, a qualitative comparison suggests that the curves have a similar trend, especially when examining the zoomed-in portion presented in the scientific paper. However, upon closer inspection, there are notable differences between the numerical results and the recorded flow rate during the experiment. In the experiment, the recorded flow rate rapidly decreases to very low values in a shorter time compared to the beginning of the release. On the other hand, the numerical simulation exhibits a much slower decrease in the flow rate behavior, even though the initial value is smaller compared to the experimental case by an order of magnitude. There are several reasons for the discrepancy, with the most significant being the underestimation of the CO_2 density. For instance, at the beginning of the release at 80 bar, the relative CO_2 density calculated using the ideal gas EOS is approximately 128.55 Kg/m^3, while the CO_2 density calculated using the Peng-Robinson EOS is approximately 204.17 Kg/m^3. The density plays a crucial role in determining the mass flow rate, as indicated by the formula:

$$Q = A * \rho * V \tag{25}$$

The Q represents the mass flow rate, A is the area where the flow is thought, and V is the velocity of the flow. However, it is important to note that the velocity of the flow can also impact the simulation results.

Considering the significant difference in the behavior of the results and the greater underestimation of the CO_2 density in high-pressure scenarios, it becomes imperative to implement models that utilize a real gas EOS. Consequently, this thesis aims to investigate different possibilities and scenarios to implement a real gas model within the simulation conducted using ANSYS Fluent software.

5.2 Testing and Implementation Strategies

As previously mentioned, the implementation of a Real gas EOS is necessary to accurately simulate the release of supercritical CO_2. From this point, a series of cases are investigated to incorporate the Real gas EOS into the software.

The first case involves directly setting the Real gas Peng-Robinson EOS in the dedicated section of the software. The same geometry, computational domain, and the other settings described for the "Ideal gas" case are used. However, when attempting to start the CFD simulation with these settings, the software encounters an error. Specifically, the "*Node #: Received signal SIGSEGV*" error is displayed, and the software abruptly closes, making it challenging to identify the cause of this error. To address this issue, several alternative tests are proposed as potential workarounds.

> *First Test*

One potential alternative is to implement User Defined Functions (UDFs) for estimating the density value of the substances involved during the simulation. UDFs, written in C language, allow extending the functionality of ANSYS Fluent software and defining additional user-defined features such as material properties, source terms, and additional boundary conditions that cannot be implemented using the built-in features of the software. The idea is to create a script capable of solving the Peng-Robinson EOS to estimate the density value. In the section discussing the EOS, two types of Peng-Robinson

(P-R) EOS were introduced. For the UDFs, the modified model of the P-R EOS (Haghtalab et al., 2011) was implemented as it explicitly defines the density term in its formulation. To solve this cubic equation (P-R EOS), an iterative method was necessary, and the Newton-Raphson method was implemented due to its efficiency in handling cubic equations. Before the UDF script, the equations and methods involved were tested in a separate C script to ensure their reliability. Only after, the P-R EOS and Newton-Raphson method were adapted into the UDF script. In addition, the "udf.h" library, which contains various functions and macros specific to Fluent software, was utilized to facilitate internal functions within the UDF. This allows the UDF script to communicate during simulations, providing real-time access to a lot of information and property parameters necessary for calculating the density using the P-R EOS. The UDFs that are described below are reported in the Appendix section at the end of the thesis.

Also, in this case, there are various possible ways to use the UDFs in the software, and a series of tests have been conducted, highlighting the encounter issues during the simulations:

- Initially, a UDF was implemented to estimate the CO_2 density and added to the CO_2 material in Fluent. The CO_2 density UDF is reported in the Appendix. However, in the case of CO_2 release into the atmosphere, there is also the presence of the air, resulting in a mixture of these two compounds. When applying a UDF only to the CO_2 material, two possibilities arise for the air density: either declaring a constant value or using another UDF specifically written for the air. In both cases, the density of the mixture is calculated using a weighted average considering the quantities of CO_2 and air. For this reason, also an air density UDF is proposed in the Appendix section. This UDF follows a similar structure to the CO_2 density UDF, utilizing the P-R EOS and Newton-Raphson methods to ensure a good approximation for the value of the density while considering air properties. However, a problem is encountered in Fluent software due to the software's restriction of interpreting only one UDFs at a time. As a solution, an alternative approach is to use a compiled library that contains both UDFs. Unfortunately, a parallel problem occurs during the compilation process, therefore a solution is needed to bypass the problem.
- To address the above-mentioned problems, a modified approach is employed. The CO_2 density UDF and the air density UDF are combined to use only the interpreted command, avoiding errors associated with the compiled command. This new script calculates the density for each element separately and, based on the molar fraction of each component, determines the weighted average density of the mixture. This revised UDF is also included in the Appendix section. However, several issues arise when using this UDF, particularly related to non-converging simulations. Upon careful examination of the software manual, it is discovered that when imposing a UDF for the density of the mixture, it is recommended to calculate all other properties using the same method. This requirement complicates the writing of the UDF, making it lengthy and challenging.

Second Test

Another alternative to the previously implemented Peng-Robinson EOS method and the UDFs method is the utilization of the Real Gas Mixture Properties Model provided by the National Institute of Standards and Technology (NIST), which can be integrated into Fluent through "console commands". There are numerous online guides available that explain how to implement this method in the software, and for this purpose, the ENEA guide (ENEA, 2009) was consulted. The NIST real gas model uses the thermodynamic and transport properties of various pure fluids from the REFPROP (Version 7.0) database to evaluate mixtures of these fluids. REFPROP, an abbreviation for reference fluid properties, employs three models for the thermodynamics properties that are: equations of state explicitly formulated in terms of Helmholtz energy, the modified Benedict-Webb-Rubin equation of state, and an extended corresponding states (ECS) model (Lemmon et al., 2018). In the specific case analyzed in this thesis, it is not possible to declare a mixture composed of CO_2 and air. Therefore, a mixture consisting of CO_2, oxygen, and nitrogen is involved when applying this method. However, using this approach leads to computationally intensive simulations, resulting in significant time consumption. In other words, each iteration during the simulation requires a substantial amount of time, which goes beyond the scope of this thesis.

Third Test

After conducting multiple tests and referring to the settings utilized in (Joshi Preeti, 2016), it was possible to understand why the error related to the implementation of the Peng-Robinson EOS in the density settings occurs. Specifically, a second-order upwind scheme for the flow spatial discretization is necessary. Additionally, in this case, instead of a pressure-based transient simulation, a density-based transient simulation was carried out with a Courant number of 0.5. However, even with these adjustments, the simulation still does not converge. The main reason for the lack of convergence is primarily attributed to the excessively high time step imposed compared to the appropriate setting. Specifically, considering the characteristic parameters such as the jet velocity, Courant number, and the smallest cell size of the mesh, the time steps should ideally be in the order of magnitude of 10^{-8} seconds. Conducting an approximate calculation, if a time step of approximately 10^{-8} seconds is used and considering a total transient duration of approximately 90 seconds, the simulation would require around $9*10^9$ time steps. Assuming an average computational time of 10 seconds per time step, the total calculation time for the simulation would amount to approximately $9*10^{10}$ seconds or 25 million hours. This extensive calculation time is impractical for conducting the simulation.

5.2.1 Real gas case in Steady-State

The tests conducted before implementing a Real Gas EOS into a transient simulation revealed that it is impossible to simulate due to the long time required by the model to simulate the release of CO_2. For this reason, a new model is proposed to simulate the release of CO_2 in a steady state. Unlike the transient case, the steady-state simulation returns result in a fasters way. As in the previous case, the description of this model and the results provided by the numerical model simulation, for practical reasons, are divided into two parts: "Configuration Setup" and "Results".

Configuration Setup

This case uses a geometrical setup that follows one of the experiments conducted by the DNV and discussed by (Joshi Preeti, 2016). This case is characterized by a hole diameter of 11.94 mm, which is larger than the hole analyzed in the preliminary case. A 2D axisymmetric model was chosen instead of a 3D model due to the symmetries presented in the CO_2 release phenomenon. This decision represents a further simplification compared to the previous model, reducing the computational effort due to the lower number of cells of the 2D mesh. Figure 79 depicts the "lateral view" of the geometry setup of the rectangular ambient area where the discharge occurs. The ambient area measures 5 meters long and 1 meter high, which is significantly larger than the release diameter, ensuring stability in the simulation. Due to the large ambient area, it is impossible to accurately visualize the pipe and the release zone near the hole, for this reason, a zoomed-in view of this region is provided in Figure 80. As previously mentioned, the hole has a diameter of 11.94 mm, so the pipe was also designed with this diameter, and its length is 120 mm, which is nearly ten times the value of the diameter of the pipe.
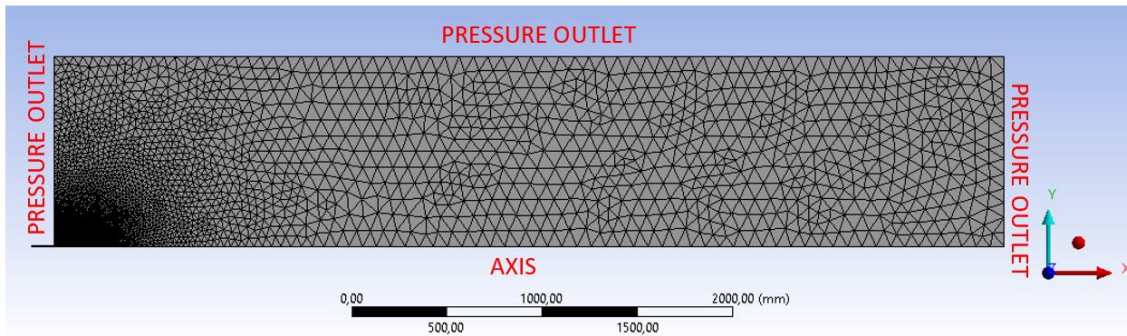
Figure 79: Geometrical setup with some Boundary conditions.
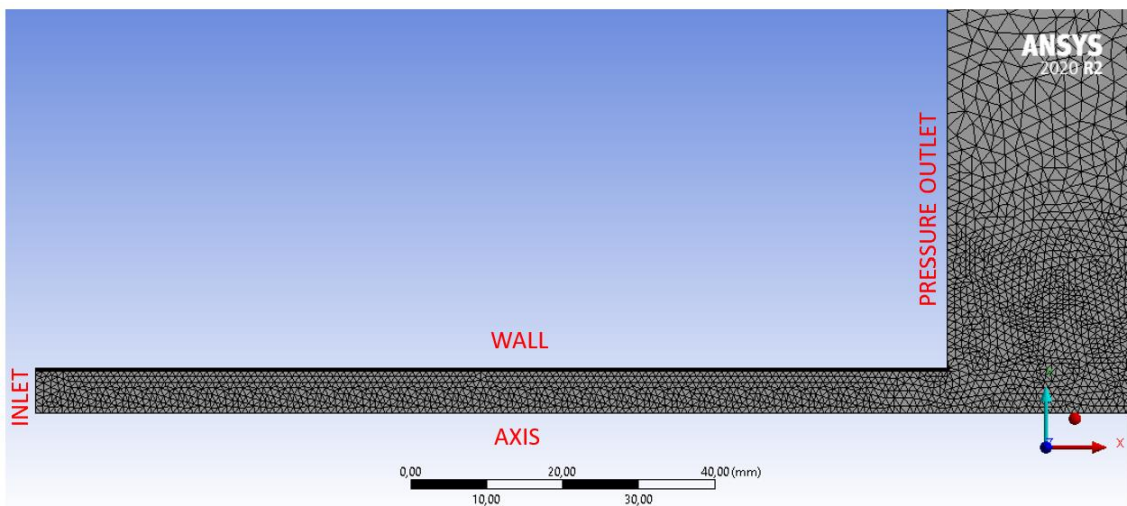

Figure 80: Zoomed-in view of the pipe and release region.

After describing the computational geometry, it is necessary to explain the methods used to create the mash. The 2D domain mesh consists of approximately 55 thousand elements, which is significantly fewer compared to the previously described 3D case. The following settings are used to create the mesh:

- A general *growth rate* of 1.05 is applied in the mesh settings to minimize the difference in element sizes between the smaller elements near the release zone and the larger elements in the farthest area from the release point.
- A general maximum element size of 50 mm is applied to the entire computational domain to control the overall size of the elements and maintain computational efficiency.
- An *edge sizing* is applied to the three sides of the pipe, namely INLET, WALL, and AXIS, imposing an element size of 0.6 mm. These sides are depicted in Figure 80.
- A *body of influence* is included to ensure smaller cell dimensions in the near-release region (only for the first 200 mm), with an element size of 0.6 mm. This setting is visible in Figure 81.
- An *inflation layer* is applied to the wall, with a first layer height of 0,000221 mm and a maximum layer number of 33. The growth rate for the inflation layer is set to 1.2. The mesh near the wall boundary condition, modeled by the inflation layer setting, can be observed in Figure 80. The *inflation laye*r is necessary at the wall to ensure stability during the simulation, as the turbulent fluid dynamics equations rely on the parameter "Y+" to describe the flow state near the solid surface.
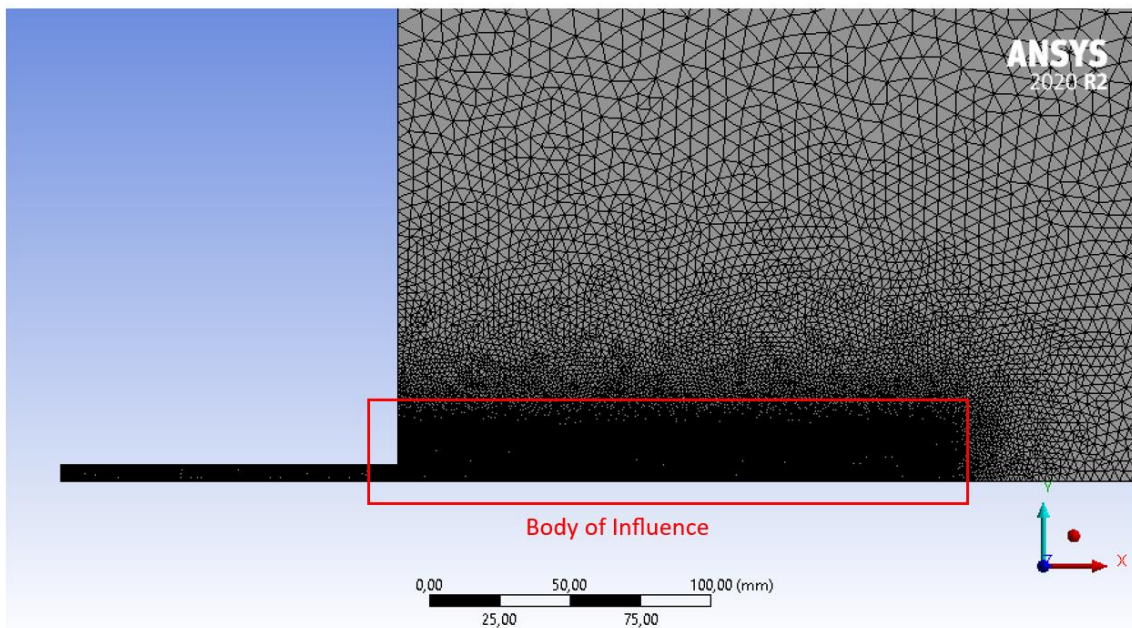
Figure 81: Zoomed-in view of the near-release region where the body of influence is present.

After building the mesh for the computational domain, it is necessary to provide a summary of the boundary conditions applied to the edge of the domain. The boundary conditions are displayed in the figure mentioned above. let's discuss them in more detail:

- *The Pressure Inlet Boundary Condition* is not assigned a precise value but follows an increasing method for the pressure value to understand at which pressure the simulation can converge. This approach is taken due to the difficulty of directly imposing a high-pressure value, which led to not converging. Initially, a simulation is carried out at 10 bar to ensure a good initialization of the parameters

in entire the domain. Subsequently, a series of simulations are conducted, incrementing the pressure value imposed at the inlet face in each simulation. The maximum pressure value reached during the simulations is described in the result section below. Additionally, a temperature of 330 K is assigned to this boundary condition, with the specification that the molar fraction consists entirely of CO_2.

- *The Pressure Outlet Boundary Conditions* on the ambient faces are kept at their default settings (see Figure 79).
- *The Axis Boundary Conditions* on the cutting domain are maintained at their default settings. These conditions enable the axisymmetric setting, which helps reduce the computational effort.
- *The Wall Boundary Condition* on the nozzle wall is also kept at its default settings, which include a Stationary wall with No Slip condition and a roughness constant of 0.5.

Finally, a steady-state density-based simulation is conducted, and the influence of gravity, in this case, is not considered. Another difference compared to the previously analyzed 3D case is the choice of the turbulence model, which, in this case, is the Realizable k-epsilon model. This model considers both viscous heating and compressibility effects. For the selection of the material, a mixture of CO_2 and air from the ANSYS Fluent database is chosen. However, since the default polynomial approximation for the specific heat at constant pressure "cp" of CO_2 has a limited validity range (from 300K to 5000K), a constant value of 1000 J/(Kg*K) is imposed to ensure validity even at lower temperatures that occur during the release. It should be noted that a more accurate approach would involve modifying the polynomial to extend its validity range. The Peng-Robinson Real Gas EOS is selected for estimating the density during the simulation. Moreover, an implicit formulation available for the density-based solver is employed. The flow equation is discretized using the Second Order Upwind method, while the other equations are discretized using the First Order Upwind method. Although the First Order Upwind method is less accurate, it offers more stability for the convergence of the solution. To ensure stability, the simulation utilizes High Order Term Relaxation and is carried out with a Courant number of 0.5. In particular, the first simulation with a pressure inlet imposed at 10 bar is conducted using the *solution staring* settings that facilitate the convergence of the simulation in the case of hypersonic flow. The subsequent simulations at higher pressure do not employ these specific settings and instead use a constant value of Courant number (0.5).

Results

One important aspect to highlight is the necessity of properly configuring the inlet pressure boundary condition in the ANSYS Fluent software. According to the software's theory guide, it is not sufficient to only set the "*gauge total pressure*" in the inlet pressure boundary settings popup but it is also crucial to specify the "*supersonic/initial gauge pressure*". It has been observed that neglecting this setting, the pressure calculated by the software does not follow the value indicated in the "*gauge total pressure*" as typically expected in subsonic simulations using this software. However, even with the settings declared in the *Computational Setup* section, the simulation only converges for maximum absolute pressure on the inlet boundary condition of approximately 49,28 bar, which falls below the pressure range (79-145 bar) relevant to the objective of this thesis. The pressure outlet through the nozzle follows the critical pressure value, which is half the inlet

pressure, indicating a choked condition at the nozzle, as shown by the contour plot in Figure 82. However, simulations with higher pressure values fail to converge.
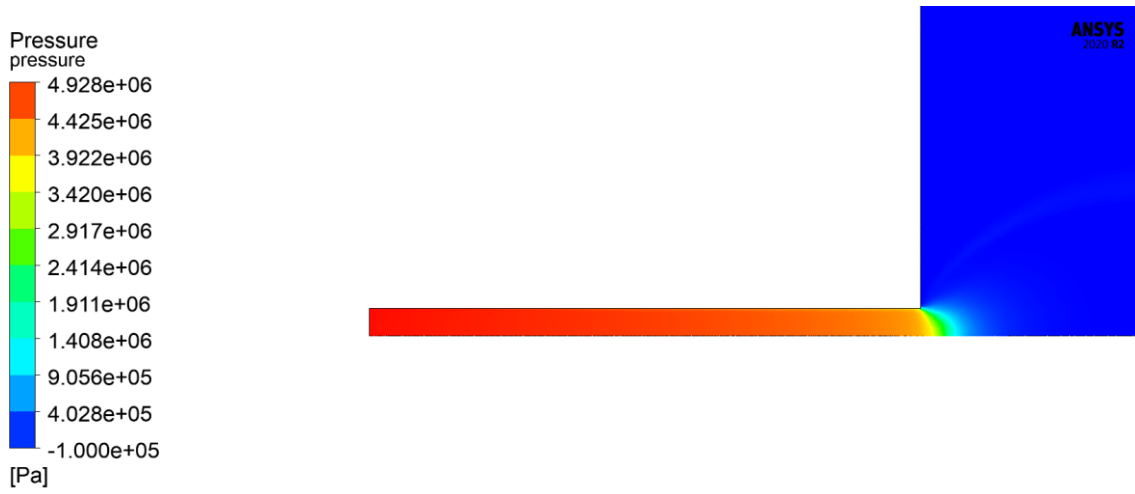
Figure 82: Absolute pressure contour plot of the case with an inlet pressure of 49,28 bar.

Regarding the temperature distribution, a temperature of 330 °C is set at the inlet boundary condition, as stated in the *Computational Setup* section. However, Figure 83 shows that the calculated average temperature value at the inlet boundary is approximately 298 °C, indicating a significant mismatch.
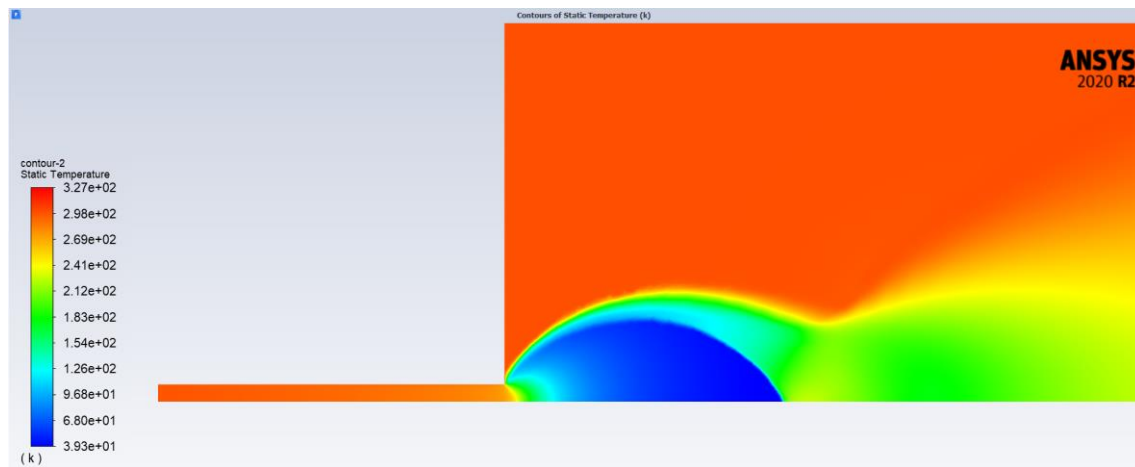
Figure 83: Temperature contour plot of the case with an inlet pressure of 49.28 bar.

Furthermore, the minimum temperature calculated near the Mach disk is excessively low (T_{min}=39.3 K) compared to the magnitude recorded by experiments in the literature review.

Figure 84 depicted a contour plot of the density distribution in the domain calculated using the Peng-Robinson real gas EOS. At the inlet boundary layer, the calculated density value is 137,14 Kg/m^3, which agrees with the value calculated analytically using a temperature of 298 °C and an absolute pressure of 49.28 bar as the results obtained from the CFD simulation.
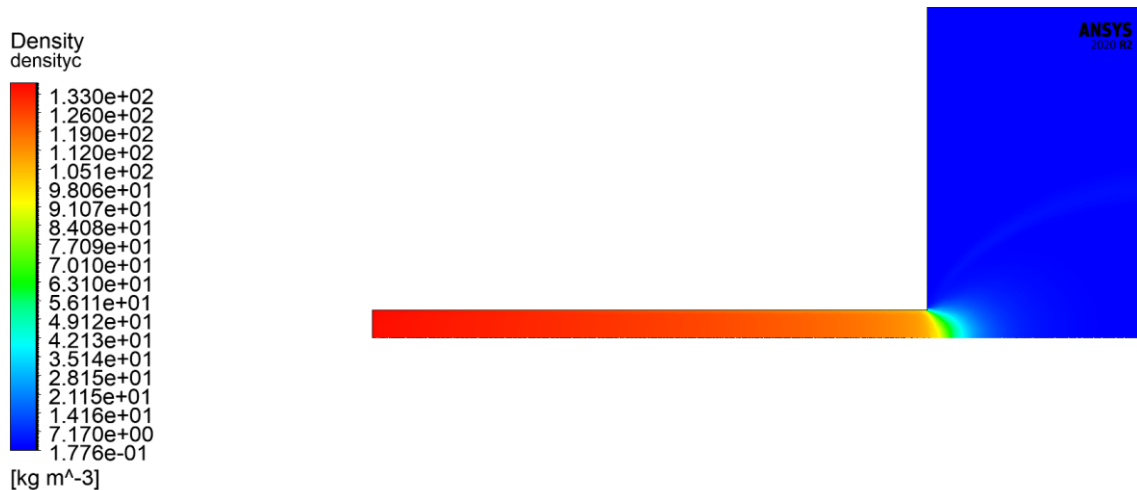
Figure 84: Density contour plot of the case with an inlet pressure of 49.28 bar.

A qualitative analysis of the Mack disk structure is provided in Figure 85, which represents a contour plot of the velocity magnitude distribution in the computational domain. The maximum velocity magnitude recorded is approximately 582 m/s, observed in the Mack disk discontinuity region.
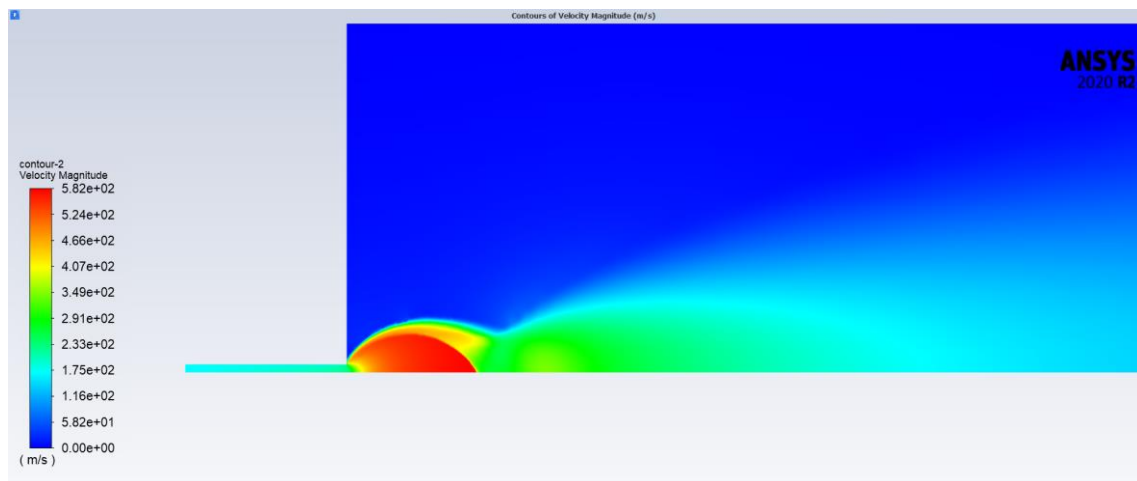
Figure 85: Velocity contour plot of the case with an inlet pressure of 49.28 bar.

However, the jet structure depicted in Figure 85 differs from the classical jet described in the literature review. To ensure that this is not a problem of this simulation, a qualitative comparison with other simulations at lower pressure is conducted. Specifically, Figure 86, Figure 87, and Figure 88 represent three different cases involving absolute pressure on the inlet layer approximately 8.75, 21.8, and 35.55 bar, respectively.

The discontinuity region of the Mack disk is in general less visible in all the cases, and also it differs from the structures analyzed in the theory of under-expanded jets, which typically exhibit a highly visible discontinuity (as shown in Figure 13, Figure 25, and Figure 40). The discontinuity between the region with a Mack number greater than one in the case with a Mack number less than one is more clearly visible in the case with lower pressures, while this phenomenon gradually disappears as the pressure increases.

The structure of the jet near the Mack disk in the latter simulations appears more oval-shaped compared to the expected shape in under-expanded jet theory.
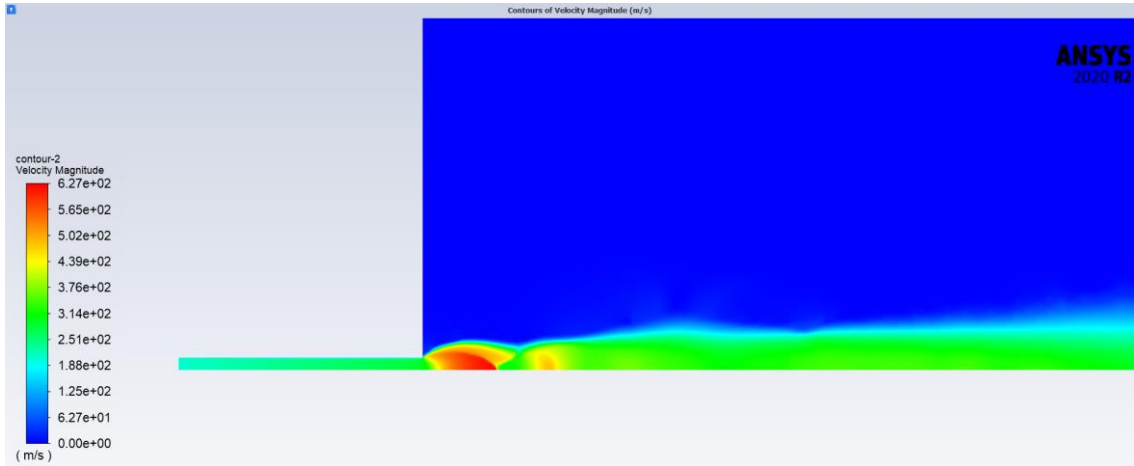
Figure 86: Velocity contour plot of the case with an inlet pressure of 8.75 bar.
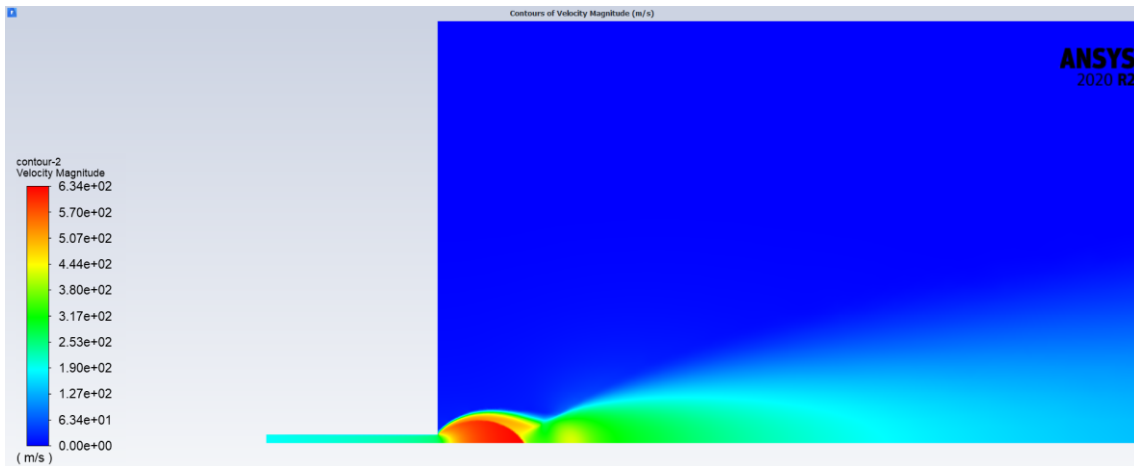
Figure 87: Velocity contour plot of the case with an inlet pressure of 21.8 bar.
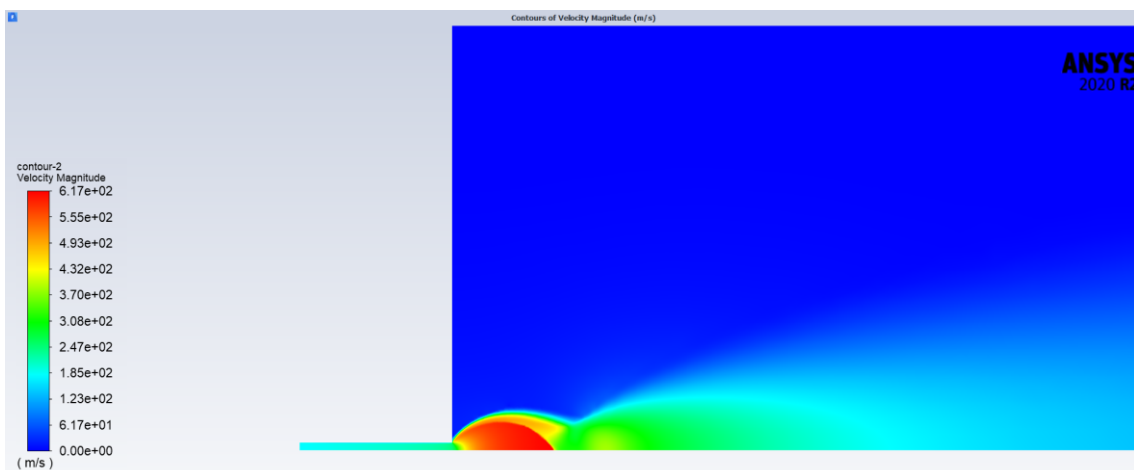
Figure 88: Velocity contour plot of the case with an inlet pressure of 35.55 bar.

Much more similar to the theoretical expectations is the region far away from the release zone, where the gas is dispersed. This is illustrated in Figure 89, which depicts the molar fraction of CO_2 released in the considered domain.
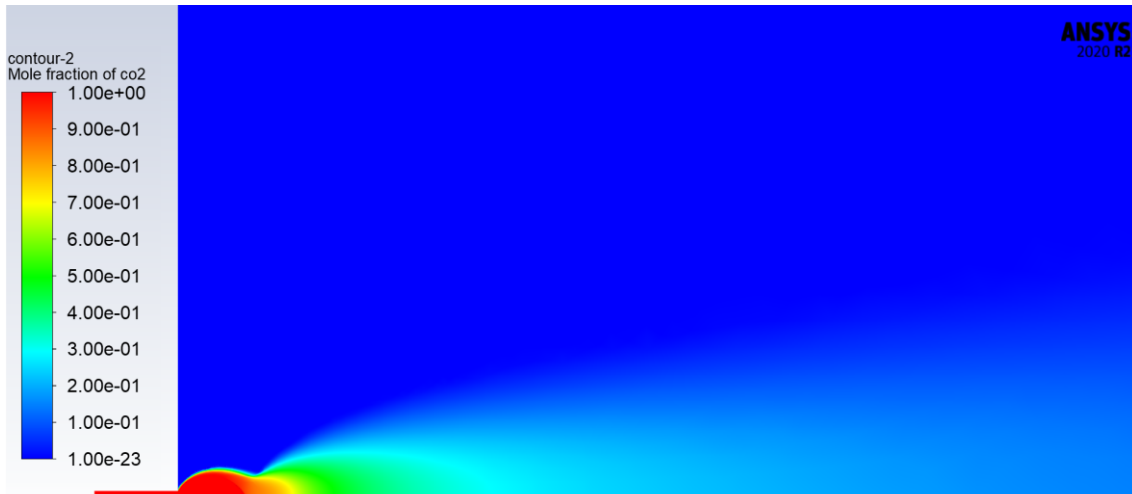
Figure 89: Molar fraction of CO_2 contour plot of the case with an inlet pressure of 49.28 bar

However, in the absence of specific experimental data, it is not possible to ensure the accuracy of the simulation in estimating the concentration of CO_2. Estimating concentrations in the release region is crucial in the context of this thesis, as it is one of the most important parameters for aspects related to industrial safety and for QRA purposes.

A grid independence analysis is proposed in Appendix B to ensure the accuracy and reliability of numerical simulations. The purpose of this analysis is to determine the minimum grid resolution that strikes a balance between obtaining reliable results and minimizing computational effort. It is important to note that in the absence of experimental data to validate the results, Appendix B aims to describe the methodology to be followed in conducting a grid independence study. The focus is on establishing a systematic approach to refine the grid and assess the convergence behavior of the solution, rather than validating the results against experimental data.

6   Conclusion

The main objective of this thesis was to provide support for a project that aimed to repurpose a decommissioned oil platform (GREEN1) as infrastructure for CO_2 storage in depleted hydrocarbon reservoirs, utilizing CCS technologies. Given the operating pressure range of 79-145 bar, the carbon dioxide undergoes a phase change from a gas to a supercritical phase during the storage operation. As a result, previous risk analyses conducted for hydrocarbon extraction are no longer applicable due to the new platform layout and the shift to carbon dioxide as a hazardous substance. Therefore, an analysis of the hazardous concentration impacting human health is provided to quantitatively understand the associated risks. However, commercially used empirical models for simulating incidental leakage scenarios for Quantitative Risk Analysis (QRA) purposes tend to overestimate the risk in the case of congested environments. This topic is extensively discussed by (Moscatello et al., 2021) and is also evident in the results presented by (Gallo A., 2021).

In this context, the primary objective of this thesis is to simulate the release of supercritical CO_2 using Computational Fluid Dynamics (CFD) methods for QRA purposes.

An analysis of the existing numerical modeling works in the literature on supercritical CO_2 releases reveals that the available information and methodology for conducting CFD simulations of this phenomenon are incomplete. Therefore, before being able to simulate supercritical CO2 releases, it is necessary to establish a strategy to address this gap in the literature. The thesis also includes a review of experiments conducted by other authors to compare the experimental data with the simulation results obtained in this study.

Since there is no precise methodology for simulating supercritical CO_2 releases using CFD methods, this thesis proposed to investigate how to simulate this phenomenon in the ANSYS Fluent software to extend the range of applicability of the SBAM model. This model is specifically developed to simulate incidental leakage scenarios in confined spaces (spaces with obstacles) using a CFD-based approach. SBAM employs a particular strategy that aims to minimize the computational effort typically associated with classical CFD analysis while ensuring precise results comparable to those obtained through CFD methods.

A preliminary simulation is presented in this thesis work that aims to replicate a specific experiment conducted by (Teng L. et al., 2021). This preliminary simulation uses the ideal gas equation of state (EOS) to simulate the behavior of the supercritical CO_2 during the release. The first results demonstrate that the ideal gas EOS does not accurately estimate density values, leading to an overestimation of CO_2 concentration in the surrounding area of the release. Additionally, parameters such as velocity magnitude and mass flow rate differ from the experimental data. Based on this comparative analysis, it is highlighted that the implementation of a Real Gas EOS is necessary to better estimate the behavior of supercritical CO_2 during a release.

A series of tests to implement a Real Gas EOS was proposed, such as using the User Defined Functions (UDFs) to implement the Peng-Robinson EOS, Real Gas NIST properties, and the Peng-Robinson EOS implemented in the software. The first case

shows not only a high computational effort due to the UDFs that communicate with the software but also a challenge when imposing a UDF for the calculation of the density of the mixture, as it is recommended to calculate all other properties using the same method. In the second case, an elevated computational effort is encountered due to the software having to communicate with the REFPROP database. In the last case, using settings similar to those used in the numerical models analyzed in the literature, it was possible to introduce the Peng-Robinson EOS just implemented in the ANSYS Fluent software. However, in this case, an issue occurs, particularly related to the time step imposed on the simulation. An analysis of the time step required by the numerical model to complete the simulation reveals that this time step is excessive and deviates from the scope of this thesis.

To overcome the time step issue, at the end of the thesis work, steady-state simulations are proposed, which are compared to the transient simulations, resulting in faster results. However, even in this case, multiple problems occur, such as mismatching parameters between the settings and the obtained results or also the non-converging simulation after a certain imposed inlet pressure boundary condition.

In conclusion, the various tests proposed in this thesis work highlight the challenging nature of implementing a simulation of supercritical CO_2 releases using the ANSYS Fluent software. Prominent research centers in the world, such as Det Norske Veritas (DNV) in its guidance on CCS CO_2 Safety and Environment (Hamish H. et al., 2021), the International Energy Agency (IEA) in its special report on Carbon Capture Utilization and Storage (IEA, 2020), and the Intergovernmental Panel on Climate Change (IPCC) in its special report on Carbon Dioxide Capture and Storage (Metz B. et al., 2005), have acknowledged that numerical modeling of incidental CO_2 leakage scenarios for QRA purposes is still in the research stage.

In the ANSYS Fluent software used in this thesis, multiphase settings are also available. Exploring this possibility could be an important strategy because it is possible to consider the solid, liquid, and gas phases of carbon dioxide and their interaction with air during the release in simulations. Another potential solution for simulating this phenomenon using CFD methods is to investigate other codes or software that could be more suitable for the numerical modeling of supercritical CO_2 releases while ensuring accurate results and reasonable calculation times.

For future analysis in this field, it would be interesting to conduct experiments on the supercritical CO_2 releases in a wind tunnel, such as the SEASTAR WT (SEASTAR, n.d.), to collect data suitable for comparison with numerical model results. This is because there is a scarcity of usable data in the existing literature. To achieve this goal, it would be necessary to develop an ad hoc scaling method, implement suitable instrumentation, and make modifications to the wind tunnel itself.

Reference

A. Aliberti. (2021). *Riconversione di una piattaforma petrolifera in dismissione per l'installazione di un impianto di dissalazione alimentato da energia fotovoltaica. Progettazione preliminare.* Politecnico di Torino.

A.C. Uggenti, Gerboni, R., Carpignano, A., Ballocco, G., Tortora, A., & Aliberti, A. (2022). Definition of a Basic Design for Conversion of an Offshore Fixed Platform on a Depleted Reservoir Into a Sustainable Plant. *ASCE-ASME Journal of Risk and Uncertainty in Engineering Systems, Part B: Mechanical Engineering*, *8*(4). https://doi.org/10.1115/1.4053061

Ashkenas H., & Sherman F. S. (1966). *Structure and Utilization of Supersonic free jets in Low Density wind tunnels*.

Carpignano A. (2009). *Risk Analysis*.

Crist, S., Sherman, P. M., & Glass, D. R. (1966). Study of the highly underexpanded sonic jet. *AIAA Journal*, *4*(1), 68–71. https://doi.org/10.2514/3.3386

Dahiru, A. R., Vuokila, A., & Huuhtanen, M. (2022). Recent development in Power-to-X: Part I - A review on techno-economic analysis. In *Journal of Energy Storage* (Vol. 56). Elsevier Ltd. https://doi.org/10.1016/j.est.2022.105861

ENEA. (2009, January 29). *ANSYS FLUENT 12.0 User's Guide*. Https://Www.Afs.Enea.It/Project/Neptunius/Docs/Fluent/Html/Ug/Main_pre.Htm.

Energy Institute. (2010). *Good plant design and operation for onshore carbon capture installations and onshore pipelines : a recommended practice guidance document*. Energy Institute.

F. Pertuso. (2022). *Riconversione di una piattaforma petrolifera in dismissione e del relativo reservoir per l'installazione di un impianto di stoccaggio di anidride carbonica. Progettazione preliminare.* Politecnico di Torino.

Franquet, E., Perrier, V., Gibout, S., & Bruel, P. (2015). Free underexpanded jets in a quiescent medium: A review. In *Progress in Aerospace Sciences* (Vol. 77, pp. 25–53). Elsevier Ltd. https://doi.org/10.1016/j.paerosci.2015.06.006

Gallo A. (2021). *Analysis of the state of the art of vulnerability and impairment thresholds associated to physical effects of a CO2 release. Application to the Allam cycle case study.*

Global CCS Institute. (2015). https://www.globalccsinstitute.com/resources/ccs-image-library/

Guo, X., Yan, X., Yu, J., Zhang, Y., Chen, S., Mahgerefteh, H., Martynov, S., Collard, A., & Proust, C. (2016). Under-expanded jets and dispersion in supercritical CO2 releases from a large-scale pipeline. *Applied Energy*, *183*, 1279–1291. https://doi.org/10.1016/j.apenergy.2016.09.088

Haghtalab, A., Mahmoodi, P., & Mazloumi, S. H. (2011). A modified Peng-Robinson equation of state for phase equilibrium calculation of liquefied, synthetic natural gas,

and gas condensate mixtures. *Canadian Journal of Chemical Engineering*, *89*(6), 1376–1387. https://doi.org/10.1002/cjce.20519

Hamish H., Parry K., & Sykes J. (2021a). *CO2RISKMAN Guidance on CCS CO 2 Safety and Environment Major Accident Hazard Risk Management Level 1-Executive Summary*.

Hamish H., Parry K., & Sykes J. (2021b). *CO2RISKMAN Guidance on CCS CO 2 Safety and Environment Major Accident Hazard Risk Management Level 2-Overview*.

Hamish H., Parry K., & Sykes J. (2021c). *CO2RISKMAN Guidance on CCS CO 2 Safety and Environment Major Accident Hazard Risk Management Level 4-Specific CCS Chain Guidance*.

Holt H., Parry K., & Sykes J. (2021). *CO2RISKMAN Guidance on CCS CO 2 Safety and Environment Major Accident Hazard Risk Management Level 3-Generic Guidance*.

IEA. (2020). *The role of CCUS in low-carbon power systems*.

IEA. (2022). *CO2 Emissions in 2022*. www.iea.org

International Energy Agency. (2020). *Technology Perspectives Energy Special Report on Carbon Capture Utilisation and Storage CCUS in clean energy transitions*. www.iea.org/t&c/

Joshi Preeti. (2016). *CONSEQUENCE ANALYSIS OF THE ACCIDENTAL RELEASE OF SUPERCRITICAL CO2 FROM HIGH PRESSURE PIPELINES*.

Kunz O., & Wagner W. (2012). The GERG-2008 wide-range equation of state for natural gases and other mixtures: An expansion of GERG-2004. *Journal of Chemical and Engineering Data*, *57*(11), 3032–3091. https://doi.org/10.1021/je300655b

Le Treut, H., Somerville, R., Cubasch, U., Allen, M., Treut, L., Somerville, R., Cubasch, U., Ding, Y., Mauritzen, C., Mokssit, A., Peterson, T., Prather, M., Marquis, M., Averyt, K., & Tignor, M. (2007). *Historical Overview of Climate Change Science*.

Lemmon, E. W., Bell, I. H., Huber, M. L., & Mclinden, M. O. (2018). *REFPROP Documentation*.

Liu B. (2016a). *Modelling of CO2 release from high pressure pipelines* [University of Wollongong]. https://ro.uow.edu.au/theses

Liu B. (2016b). *Modelling of CO2 release from high pressure pipelines*. https://ro.uow.edu.au/theses

Masson D., P. Zhai, A. Pirani, S.L. Connors, C. Péan, S. Berger, N. Caud, Y. Chen, L. Goldfarb, M.I. Gomis, M. Huang, K. Leitzell, E. Lonnoy, J.B.R. Matthews, T.K. Maycock, T. Waterfield, O. Yelekçi, R. Yu, & B. Zhou. (2021). *IPCC, 2021: Climate Change 2021: The Physical Science Basis. Contribution of Working Group I to the Sixth Assessment Report of the Intergovernmental Panel on Climate Change*. https://doi.org/10.1017/9781009157896

Metz B., O. Davidson, H. C. de Coninck, M. Loos, & L. A. Meyer. (2005). *CARBON DIOXIDE CAPTURE AND STORAGE*.

Mondini G. (2019). Valutazioni di sostenibilità: dal rapporto Brundtland ai Sustainable Development Goal. *Valori e Valutazioni*.

Moscatello A. (2023). *Development and experimental validation of a novel CFD approach for the simulation of high-pressure accidental gas releases*.

Moscatello, A., Uggenti, A. C., Gerboni, R., & Carpignano, A. (2021). A novel approach to high-pressure gas releases simulations. *Journal of Loss Prevention in the Process Industries*, *72*. https://doi.org/10.1016/j.jlp.2021.104531

Munson B.R., Okiishi T.H., Huebsch W. W., & Rothmayer A. P. (n.d.). *Fundamental of Fluid Mechanics*.

Peng D., & Robinson D. (1976). A New Two-Constant Equation of State. In *Int. J. Heat Mass Transfer* (Vol. 19). https://pubs.acs.org/sharingguidelines

Ritchie H., Roser M., & Rosado P. (2017). *CO2 and Greenhouse Gas Emissions*. Our World in Data CO2.

Sallée, J. B., Matear, R. J., Rintoul, S. R., & Lenton, A. (2012). Localized subduction of anthropogenic carbon dioxide in the Southern Hemisphere oceans. *Nature Geoscience*, *5*(8), 579–584. https://doi.org/10.1038/ngeo1523

SEASTAR. (n.d.). *Seastar wind tunnel*. Retrieved July 6, 2023, from http://www.seastar-wt.polito.it/

Span, R., & Wagner, W. (1996). A new equation of state for carbon dioxide covering the fluid region from the triple-point temperature to 1100 K at pressures up to 800 MPa. *Journal of Physical and Chemical Reference Data*, *25*(6), 1509–1596. https://doi.org/10.1063/1.555991

Teng L., Bai, J., Li, Y., & Wang, C. (2021). An Experiment on Flashing-Spray Jet Characteristics of Supercritical CO2 from Various Orifice Geometries. *Frontiers in Energy Research*, *9*. https://doi.org/10.3389/fenrg.2021.697031

Teng L., Li, Y., Hu, Q., Zhang, D., Ye, X., Gu, S., & Wang, C. (2018). Experimental study of near-field structure and thermo-hydraulics of supercritical CO2 releases. *Energy*, *157*, 806–814. https://doi.org/10.1016/j.energy.2018.04.195

Teng, L., Liu, X., Li, X., Li, Y., & Lu, C. (2021). An approach of quantitative risk assessment for release of supercritical CO2 pipelines. *Journal of Natural Gas Science and Engineering*, *94*. https://doi.org/10.1016/j.jngse.2021.104131

UN. (2015). *Transforming our world: the 2030 Agenda for Sustainable Development*.

UNFCCC. (2015). *ADOPTION OF THE PARIS AGREEMENT*.

UNFCCC. (2019). *Action on Climate and SDGs*. Https://Unfccc.Int/Topics/Cooperative-Activities-and-Sdgs/Action-on-Climate-and-Sdgs.

United States Environmental Protection Agency. (2023). *Inventory of U.S. Greenhouse Gas Emissions and Sinks*. Https://Www.Epa.Gov/Ghgemissions/Inventory-Us-Greenhouse-Gas-Emissions-and-Sinks.

Vendrig M., Spouge J., Bird A., Daycock J., & Johnsen O. (2003). *Risk Analysis of the Geological Sequestration of Carbon Dioxide*.

Witlox, H. W. M., Harper, M., & Oke, A. (2012). *PHAST VALIDATION OF DISCHARGE AND ATMOSPHERIC DISPERSION FOR PRESSURISED CARBON DIOXIDE RELEASES*.

World Commission on Environment and Development. (1987). *Report of the World Commission on Environment and Development: Our Common Future*.

Zanzi S. (2017). *Numerical Simulation of Condensing CO2 Supersonic Flows at High Pressure*. Politecnico di Milano.

Appendix A

This section includes three User Defined Functions (UDFs) for ANSYS Fluent software, used for calculating the density of CO_2, air, and the CO_2 – air mixture, respectively.

- **UDF for the CO_2 density calculation:**

```
#include "udf.h"

#define TOLERANCE 0.0001

#define R_UNIVERSAL 8.3144598 // [J/mol/K]


    double PM=44; // Peso molecolare [g/mol]

    double Tc=304.12; // Temperatura critica [K]

    double w=0.225; // Fattore acentrico

    double Pc;

    double Tr;

    double R_gas;

    double k;

    double alphaT;

    double b;

    double a;


    double ro0;

    double ro1;

    double error;

    int iterations = 0;


DEFINE_PROPERTY(density_co2, c, t) {

    real ro;


    double P = C_P(c, t); // Pressione [Pa]
```

```
double T = C_T(c, t); // Temperatura [K]


Pc = 7.374*pow(10,6); // Pressione critica [Pa]

Tr = T/Tc; // Temperatura ridotta

R_gas = R_UNIVERSAL/(PM*pow(10,-3));

k = 0.37464+1.54226*w-0.26992*pow(w,2);

alphaT = pow((1+k*(1-sqrt(Tr))),2);

b = 0.07780*(R_gas*Tc/Pc);

a = 0.45724*(((pow(R_gas,2))*(pow(Tc,2)))/Pc)*alphaT;



//initial guess for root

ro0=200;


do{
    // Compute the next approximation of the root
    ro1=ro0-((P*pow(b,3)+R_gas*T*pow(b,2)-a*b)*pow(ro0,3)+(-3*P*pow(b,2)-
R_gas*T*2*b+a)*pow(ro0,2)+(P*b-R_gas*T))/((P*pow(b,3)+R_gas*T*pow(b,2)-
a*b)*3*pow(ro0,2)+(-3*P*pow(b,2)-R_gas*T*2*b+a)*2*ro0+(P*b-R_gas*T));


    // compute the error in the approximation
    error = fabs(ro1-ro0);


    // Update the current approximation
    ro0=ro1;


    // increment the iteration count
    iterations++;
} while (error > TOLERANCE && iterations < 1000);
ro = ro0;
```

```
    return ro;
```

- **UDF for the air density calculation:**

```c
#include "udf.h"

#define TOLERANCE 0.0001

#define R_UNIVERSAL 8.3144598 // [J/mol/K]


    double PM=28.96; // Peso molecolare [g/mol]

    double Tc=132.3; // Temperatura critica [K]

    double w=0.033; // Fattore acentrico

    double Pc;

    double Tr;

    double R_gas;

    double k;

    double alphaT;

    double b;

    double a;


    double ro0;

    double ro1;

    double error;

    int iterations = 0;


DEFINE_PROPERTY(density_air, c, t) {

     real ro;


    double P = C_P(c, t); // Pressione [Pa]

    double T = C_T(c, t); // Temperatura [K]
```

```
Pc = 3758000; // Pressione critica [Pa]

Tr = T/Tc; // Temperatura ridotta

R_gas = R_UNIVERSAL/(PM*pow(10,-3));

k = 0.37464+1.54226*w-0.26992*pow(w,2);

alphaT = pow((1+k*(1-sqrt(Tr))),2);

b = 0.07780*(R_gas*Tc/Pc);

a = 0.45724*(((pow(R_gas,2))*(pow(Tc,2)))/Pc)*alphaT;



//initial guess for root

ro0=200;


do{
    // Compute the next approximation of the root
    ro1=ro0-((P*pow(b,3)+R_gas*T*pow(b,2)-a*b)*pow(ro0,3)+(-3*P*pow(b,2)-
R_gas*T*2*b+a)*pow(ro0,2)+(P*b-R_gas*T))/((P*pow(b,3)+R_gas*T*pow(b,2)-
a*b)*3*pow(ro0,2)+(-3*P*pow(b,2)-R_gas*T*2*b+a)*2*ro0+(P*b-R_gas*T));


    //Compute the error in the approximation
    error = fabs(ro1-ro0);


    // Update the current approximation
    ro0=ro1;


    //Increment the iteration count
    iterations++;
} while (error > TOLERANCE && iterations < 1000);


ro = ro0;

return ro;
```

```
}
```

- **UDF for the density of CO₂ and air mixture:**

```
#include "udf.h"

#define TOLERANCE 0.0001

#define R_UNIVERSAL 8.3144598 // [J/mol/K]

// definisco le proprietà dell'aria

    double PM_air=28.96; // Peso molecolare [g/mol]
    double Tc_air=132.3; // Temperatura critica [K]
    double w_air=0.033; // Fattore acentrico
    double Pc_air;
    double Tr_air;
    double R_gas_air;
    double k_air;
    double alphaT_air;
    double b_air;
    double a_air;
    double Yi_air;
    double P_air;

    double ro0_air;
    double ro1_air;
    double error_air;
    int iterations_air = 0;
```

```c
// definisco le proprietà della CO2

    double PM_co2=44; // Peso molecolare [g/mol]

    double Tc_co2=304.12; // Temperature critica [K]

    double w_co2=0.225; // Fattore acentrico

    double Pc_co2;

    double Tr_co2;

    double R_gas_co2;

    double k_co2;

    double alphaT_co2;

    double b_co2;

    double a_co2;

    double Yi_co2;

    double P_co2;


    double ro0_co2;

    double ro1_co2;

    double error_co2;

    int iterations_co2 = 0;

DEFINE_PROPERTY(density_mixture, c, t) {

    real ro_mixture;

    real ro_air;

    real ro_co2;


    int i;
```

```
double P_tot = C_P(c, t); // Pressione [Pa]

double T = C_T(c, t); // Temperatura [K]


Yi_co2=C_YI(c,t,i);


// proprietà air

    Yi_air=1-Yi_co2;

    P_air=P_tot*Yi_air;

    Pc_air = 3758000; // Pressione critica [Pa]

    Tr_air = T/Tc_air; // Temperatura ridotta

    R_gas_air = R_UNIVERSAL/(PM_air*pow(10,-3));

    k_air = 0.37464+1.54226*w_air-0.26992*pow(w_air,2);

    alphaT_air = pow((1+k_air*(1-sqrt(Tr_air))),2);

    b_air = 0.07780*(R_gas_air*Tc_air/Pc_air);

    a_air = 0.45724*(((pow(R_gas_air,2))*(pow(Tc_air,2)))/Pc_air)*alphaT_air;


// proprietà co2

    P_co2=P_tot*Yi_co2;

    Pc_co2 = 7.374*pow(10,6); // Pressione critica [Pa]

    Tr_co2 = T/Tc_co2; // Temperatura ridotta

    R_gas_co2 = R_UNIVERSAL/(PM_co2*pow(10,-3));

    k_co2 = 0.37464+1.54226*w_co2-0.26992*pow(w_co2,2);

    alphaT_co2 = pow((1+k_co2*(1-sqrt(Tr_co2))),2);

    b_co2 = 0.07780*(R_gas_co2*Tc_co2/Pc_co2);

    a_co2 = 0.45724*(((pow(R_gas_co2,2))*(pow(Tc_co2,2)))/Pc_co2)*alphaT_co2;


//initial guess for the root

    ro0_air=200;

    ro0_co2 = 200;
```

```
    do{

        // Compute the next approximation of the root

        ro1_air=ro0_air-((P_air*pow(b_air,3)+R_gas_air*T*pow(b_air,2)-
a_air*b_air)*pow(ro0_air,3)+(-3*P_air*pow(b_air,2)-
R_gas_air*T*2*b_air+a_air)*pow(ro0_air,2)+(P_air*b_air-
R_gas_air*T))/((P_air*pow(b_air,3)+R_gas_air*T*pow(b_air,2)-
a_air*b_air)*3*pow(ro0_air,2)+(-3*P_air*pow(b_air,2)-
R_gas_air*T*2*b_air+a_air)*2*ro0_air+(P_air*b_air-R_gas_air*T));


        //Compute the error in the approximation

        error_air = fabs(ro1_air-ro0_air);


        // Update the current approximation

        ro0_air=ro1_air;


        //Increment the iteration count

        iterations_air++;

    } while (error_air > TOLERANCE && iterations_air < 1000);


    do{

        // Compute the next approximation of the root

        ro1_co2=ro0_co2-((P_co2*pow(b_co2,3)+R_gas_co2*T*pow(b_co2,2)-
a_co2*b_co2)*pow(ro0_co2,3)+(-3*P_co2*pow(b_co2,2)-
R_gas_co2*T*2*b_co2+a_co2)*pow(ro0_co2,2)+(P_co2*b_co2-
R_gas_co2*T))/((P_co2*pow(b_co2,3)+R_gas_co2*T*pow(b_co2,2)-
a_co2*b_co2)*3*pow(ro0_co2,2)+(-3*P_co2*pow(b_co2,2)-
R_gas_co2*T*2*b_co2+a_co2)*2*ro0_co2+(P_co2*b_co2-R_gas_co2*T));


        //Compute the error in the approximation

        error_co2 = fabs(ro1_co2-ro0_co2);


        // Update the current approximation

        ro0_co2=ro1_co2;
```

```
        //Increment the iteration count

        iterations_co2++;

    } while (error_co2 > TOLERANCE && iterations_co2 < 1000);


    ro_mixture=(ro0_air*Yi_air+ro0_co2*Yi_co2)/(Yi_air+Yi_co2);


    return ro_mixture;

}
```

Appendix B

This section aims to analyze the grid independence on the steady-state case presented in Chapter 5. The objective is to validate the accuracy of the obtained results and to explain the methodology employed for conducting the grid independence study.

The grid independence analysis compares four different cases with the same computational domain (see Figure 79, Figure 80, and Figure 81), but with varying levels of mesh refinement. The minimum element size of the mesh is considered the characteristic length. Specifically, four different characteristic lengths are used to build the mesh: 0.46, 0.6, 0.9, and 1.2, respectively. The other mesh settings such as the maximum size of the element and the element size of the body influenced are regulated with the same percentage in which the characteristic length change.

Figure 90 displays the graph comparing the minimum temperature values in the computational domain for four different cases mentioned above. Interestingly, the trend observed in this graph shows an increase in the minimum temperature as the mesh is thickened. In fact, the cases with characteristic lengths of 0.46, 0.6, and 0.9 exhibit very similar values, specifically 36.12 K, 35.7 K, and 36.22 K, respectively. In contrast, the case with a characteristic length of 1.2 calculates a significantly lower minimum temperature value in the computational domain, approximately 32.26 K. Regarding the minimum temperature analysis, it is crucial to underline that the lowest temperature in the computational domain is located at the position of the Mach disk.
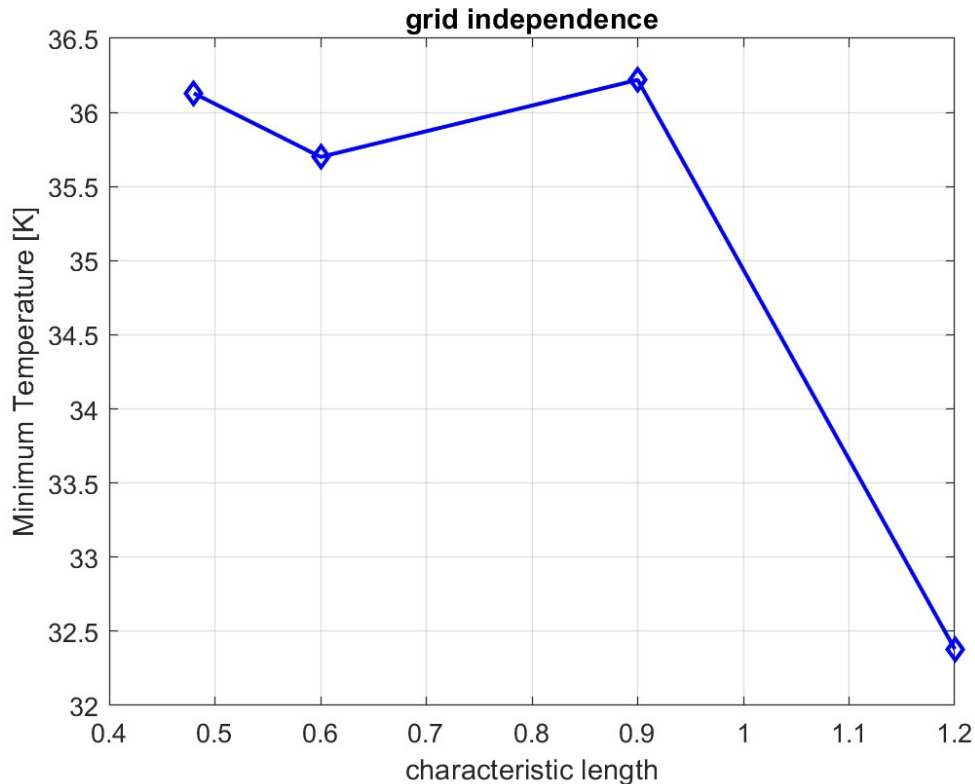

Figure 90: Grid independence comparing the minimum temperature in the computational domain calculated for four different cases with characteristic lengths of 0.46, 0.6, 0.9, and 1.2, respectively.

Acknowledgments

I would like to acknowledge my supervisor Prof. Andrea Carpignano for the trust placed in me and for making the collaboration on this project possible, which has contributed to the development of this work.

I wish to extend my special thanks to Alberto Moscatello and Prof. Raffaella Gerboni for their constant support during the thesis work and the writing of this document.

Additionally, I would like to express my thanks to the company RAMS&E for involving me in the internship activities.